Miniaturizated Respiratory Monitoring: Synchronous Demodulation & Bi-directional Ultrasonic Flow Sensing

by

Gregory Begin

Submitted in partial fulfillment of the requirements
for the degree of Doctor of Philosophy.

at

Dalhousie University
Halifax, Nova Scotia
April 2023

To Mom, Dad, and Malory

TABLE OF CONTENTS

List of Tables

List of Figures

ABSTRACT

The issues surrounding optimization of respiratory monitoring are of size, power, and SNR (Signal to Noise Ratio). Miniaturization and optimization of components within a respiratory monitoring system is valuable for integration into existing non-invasive ventilators, including, but not limited to the FOT (Forced Oscillation Technique) source, sensors, signal processing and generation. This document contains a low power analog Lock-in Amplifier (LIA) in CMOS 0.18um to measure respiratory impedance at low frequencies ($4Hz < f < 100$), and a speed of sound invariant, ultrasonic based flow meter for reduction of series impedance when sensing flow. This LIA relaxes requirements on signal input power by maintaining a precise frequency selection in the modulation and demodulation of FOT, improving the effective bandpass quality factor when averaged over long time periods, and significantly reducing the power requirement of impedance calculations. This LIA, when integrated with current ventilation devices, would allow for long term exploration of respiratory health through a diverse band of FOT frequencies and open more avenues for research with large sets of data to improve respiratory diagnostics. The ultrasonic based flow meter, leverages TDC (Time to Digital Conversion) to measure the time of flight of ultrasonic waves within the breathing path, instead of using a conventional differential pressure measurement across a known impedance. This ultrasonic sensor uses a symmetric style of measurement that cancels the effect of changes in speed of sound, isolating flow from temperature and humidity variations during breathing. This ultrasonic sensor is a more compact, bi-directional (positive and negative flow) and inexpensive form of capturing flow that is capable of highly linear operation, high resolution and sampling rate, while not adding series impedance to the measurement. Together, these components comprise a large portion of a functional respiratory monitoring platform.

List of Abbreviations and Symbols Used

SA	Sleep Apnea
CMOS	Complementary Metal Oxide Semiconductor
SNR	Signal to Noise Ratio
FOT	Forced Oscillation Technique
DC	Direct Current (Limited variation in signal)
TDC	Time to Digital Converter
IC	Integrated Circuit
PCB	Printed Circuit Board
CPAP	Continuous Positive Airway Pressure
BMI	Body Mass Index
HFLA	High Frequency Low Amplitude
MEMS	Micro-Electro-Mechanical System
FFT	Fast Fourier Transform
STFT	Short-Time Fourier Transform
LMS	Least Mean Squares
ADC	Analog to Digital Converter
DAC	Digital to Analog Converter
TOF	Time-Of-Flight
AM	Amplitude Modulation
TX	Transmitter
RX	Receiver
LSB	Least Significant Bit
MOSFET	Metal-Oxide-Semiconductor Field Effect Transistor
PLL	Phase Locked Loop
PSoC	Programmable System on Chip
PWM	Pulse Width Modulation
PGA	Programmable Gain Amplifier
HME	Heat and Moisture Exchanger
LIA	Lock-In-Amplifier
LNA	Low-Noise Amplifier
BW	Bandwidth
BPF	Bandpass Filter
MCU	Microcontroller
1P6M	One-Poly Six-Metal Manufacturing Process
LDO	Low Dropout Voltage Regulator
DAQ	Data Acquisition System
GUI	Graphical User Interface
SAR	Successive Approximation Register

ACKNOWLEDGEMENTS

First and foremost, I would like to express my sincerest gratitude to my supervisors, Dr. Kamal El-Sankary and Dr. Hamed Hanafi. Your consistent involvement, guidance, teaching, patience, and unwavering support over the years has been paramount to my success and has given me an exceptional graduate experience. The opportunities and encouragement to express my creativity has been cardinal to realizing the potential you saw in me. Thank you for preparing me for a successful career, for showing me what it means to be humble, to have a solid work ethic, and for making my dreams a reality; you two are an inspiration.

I would like to give thanks to colleagues and professors who have been a positive influence on me; Thank you, Dr. Jason Gu, and Dr. William Phillips for taking the time to review my work and advise me as a part of my supervisory committee. Thank you, Dr. Vincent Sieben, I appreciate having had the opportunity to work with you in your lab and to have you now as a graduate coordinator, and thank you Dr. Karama Al-Tamimi for being a constant presence during the pandemic, for assisting me with using cadence virtuoso tools, and helping mentor me with some of the literature in microelectronics,

I would also like to thank the colleagues and friends I've made along the way, and those that have supported me in ways that aren't always as tangible. Thank you, Dr. Steve Driscoll, Luke Hacquebard, Guillermo Aritsi, Lee Babin, Meagan Sinclair, and Najmeh Sadatnejad for supporting my graduate studies journey through your positivity, advice, and friendly presence over the years. Thank you, Dr. Rodolph Uher, for helping me through some of my hardest times and working with me to make my mental health the best it can be. Thank you, Josh, Evan, Kevin, Hunter and friends, for prioritizing our friendships despite my unavailability at times.

I'd like to give thanks to my family. Thank you, Dad, for encouraging my sense of curiosity, for being a role model of humility, stoicism, and knowledge, and for being a solid family foundation. Thank you, Mom, for always believing in me, for teaching me generosity, for giving so much of yourself, and always having an ear open when I need it most, and of course, thank you to everyone in my family who supported me along the way.

Lastly, and certainly not least, thank you to my partner Malory Macdonald; for the unconditional love and support you so selflessly give every day, and for showing me that there is more to life than studies, without you, none of this would have been possible.

Chapter 1 : INTRODUCTION

Respiratory disorders affect a large proportion of the population. It is estimated that at the very least, one in twenty people will suffer from sleep apnea in their lifetime. [1] Roughly the same number will suffer from COPD or Asthma [2],[3]. From causing high blood pressure, to obesity, heart disease and diabetes, these respiratory disorders can be life threatening if left untreated. Thus, monitoring the frequency and progression of respiratory disorders as well as improving therapy techniques can help doctors better diagnose and prevent these problems to save lives. This places a high importance on capturing reliable data from sensors attached to the airways of patients. Existing sensors boast a high degree of linearity, range, and resolution, though many have their drawbacks, from having sensitivity to flow in only one direction, being large in size and cost, or having series impedance, improvements in this space are possible. Chapter 2 walks through the current literature and state of a typical respiratory monitoring system, sensors, forced oscillation technique, respiratory impedance, the lock in technique and other relevant literature to this dissertation.

Chapter 3 explores the design and proof of concept for an ultrasonic based flow meter, resilient to fluctuations in speed of sound, used in a respiratory capacity, and is compared against an existing and widely accepted platform for measuring airflow to the lungs. Ultrasonic based flow metering devices have been used in industry for some time, however, only recently have they been used in a respiratory capacity. Existing ultrasonic respiratory flow metering devices show only an indication of flow rather than an accurate measurement compared to standards used in respiratory therapies. This chapter shows the design and analyses for constructing a flow meter that competes in this space. Flow sensing is only a portion of the respiratory measurement platform; pressure is also recorded during breathing and can be used in conjunction with flow to determine impedance of the airways through oscillometry. Pressure signals are relatively high in SNR compared to flow due to the nature of the high impedance of the airways and thus more importance can be placed on development of a high resolution and SNR flow meter as opposed to pressure. However, additional signal processing techniques, particularly in the analog domain, can be leveraged to improve the signal recovery of flow. Chapter 4 explores the design of an analog lock in amplifier, constructed

in CMOS 0.18um technology for improving power draw and integrability into existing ventilation devices while maintaining signal recovery of respiratory impedance. Respiratory oscillometry, also known as forced oscillation technique (FOT), describes how the respiratory system can be stimulated by pressure waves to induce a flow response within the volume encompassing the airways. If FOT is done at a single frequency, the effective impedance at this frequency can be revealed by taking the phasor ratio of measured pressure and flow. The pressure and flow signals fed into this chip are first split into four channels (in-phase & quadrature for both pressure & flow). These signals first see passive mixers for demodulation, whose demodulation phase and frequency are matched through synchronous generation of FOT and demodulation clock phases. The demodulated signals are upconverted through chopper stabilization, amplified, down converted, and filtered to produce low-noise level DC values correlated to the phase and amplitude distortion caused by the respiratory system. These in-phase and quadrature values are then converted from cartesian to polar and operated on by phasor division to acquire respiratory impedance. This single frequency impedance measurement can give health care practitioners vital information about the health of the airways and can lead to diagnosis and treatment of disorders mentioned earlier.

Chapter 5 includes supplementary material to augment the analysis and design processes of the ultrasonic based flow metering system and the lock-in amplifier. This chapter shows how zero crossing detection is invariant to ultrasonic pulse wave energy, while envelope detection is not, and the magnitude of error that is expected when dealing with pulse envelope. The analysis of when these zero-crossing measurements should be taken is explored, and how the standard deviation of phase measurements degrades in time using time to digital conversion, while using a crystal oscillator in a phase locked loop with the TDC clock improves this standard deviation of phase. The various geometries for sensor tube designs are shown, and collected data on the range and resolution of flow for each geometry is demonstrated. Maximizing sampling frequency i.e. pulse repetition rate, is explored by pushing the ultrasonic pulses as close together as possible. Anti-phase pulses are added in an attempt to quash the undesirable ringdown effects of the pulses, with some effect on amplitude, the duration of measurable ringdown doesn't change. The elimination of channel noise by taking bidirectional measurements are shown. The zero-flow state shows large deviations in speed of sound when single sided measurements are taken, while the difference in phases shows virtually no channel noise. Finally, data from a single channel of the folded cascode amplifier using various phases and frequencies as input shows the intermediate

step of demodulation and flicker noise suppression before aggressive filtering by the floating ground capacitors. Additional results of a low pass filter frequency response, and overall topology for the integration into a respiratory monitoring setup is presented. The appendix contains images of the PCB circuit and layout design, as well as additional images of the fabricated chip, layouts, circuits, and firmware.

I. Thesis Objectives

The primary objective of this thesis is to reduce the size, cost, and power requirements of respiratory monitoring systems to improve the portability and integrability into existing non-invasive ventilators. This generates a pathway for low power, large scale, continuous monitoring of respiratory mechanics. The first avenue to accomplish this goal is to utilize synchronous generation and demodulation of FOT in a low-power analog CMOS process to capture impedance data of the airways and surrounding tissue, making what is effectively a highly sensitive benchtop device (Lock-In Amplifier), capable of integration into non-invasive ventilators, while maintaining SNR capabilities, and decreasing power requirements in processing. The other goal is a flow measurement system that simultaneously drives down the cost of production for sensing flow, eliminates resistance in the pathway of breathing, and maintains a competitive sampling rate, resolution and linearity for measuring respiratory signals. This goal would lower the cost of production for respiratory monitoring systems and improve the patient pressure delivery by eliminating series resistance.

II. Original Contributions

1. I applied the synchronous demodulation signal processing technique of lock in amplifiers to respiratory oscillometry, to improve signal recovery of FOT, lower the power requirements for FOT signal processing and generation, and created an avenue for large scale continuous respiratory health monitoring.
2. I designed, fabricated, tested, and validated a novel LIA structure in CMOS 0.18um, purposed for respiratory mechanics monitoring. This unique structure contains:

- A passive mixer front end for a wide linear input range, virtually zero-power operation and lack of flicker noise contribution.
- Modified non-monotonic gain feedback structure.
- Low power and Chopper stabilized folded cascode amplifier for reasonable gain and low-frequency noise suppression of the gain stage.
- Sub-Hz low pass filtering for high effective bandpass quality factor

3. I adapted from literature, an AC grounded capacitor multiplier structure for significant gains in capacitive multiplication and a massive reduction in power consumption.
4. I showed how the optimum value of area consumption for any filter designed with R and C is spatially optimized when the area of the capacitors and resistors are matched.
5. Using the adapted AC grounded capacitor multiplier, I designed a novel 2^{nd} order, sub-1Hz low pass filter, with a wide linear input range compared to pseudo-resistor based filters, that consumes substantially lower area than its fully passive counterpart.
6. I designed, built, and validated a novel ultrasonic-based respiratory flow sensor prototype that is insensitive to temperature fluctuations associated with breathing, and competes with other respiratory flow meters in linearity, resolution, and sampling rate while not adding any series resistance to the fluid flow path.
7. I demonstrated through simulation and mathematical modelling how zero crossing detection is superior to envelope detection in terms of reduction in phase noise when determining time of flight of ultrasonic waves.
8. I demonstrated the standard deviation, i.e uncertainty, of time-of-flight measurements increases with time and is proportional to the frequency stability of the time to digital converter clock.

Chapter 2 : Literature Review

I. Sleep Apnea

Sleep Apnea is characterized by the intermittent lack of breathing during sleep and can fall into two main categories: obstructive, and central. Obstructive Sleep Apnea is where the patient's soft tissue surrounding their airway collapses, preventing the patient from breathing. As their blood CO_2 levels rise and O_2 falls, they enter lighter forms of sleep, sometimes waking entirely before their muscle tone returns and the soft tissue moves sufficiently to facilitate breathing again [4]. Central Sleep Apnea is where the autonomic nervous system responsible for maintaining breathing during sleep stops functioning. This causes the person to halt their breathing without having an obstructive event, suffering from the same drawbacks of low blood oxygen and high blood CO_2. A third category called Hypopnea, is a condition of low flow and can be either central or obstructive. As a precursor to an obstructive apnea, obstructive hypopneas happen as the airways relax, the soft tissue can oscillate as it struggles to stay open. Obstructive hypopneas can often be observed as audible snoring. These apneic events can occur hundreds of times in a night in those without treatment and dramatically affect their ability to feel rested after a night's sleep, and chronic effects are fatal. The treatment for obstructive apneas is different from that of central apneas. The most basic treatment for the obstructive type involves increasing and maintaining a positive airway pressure by using a CPAP machine, reducing the chances of soft tissue collapse.

Central apneas are correlated with progressive heart disease, high BMI (body mass index), stroke, prescription medications and the frequency of obstructive apneas. While CPAP therapy can help reduce the frequency of central apneas, more elaborate treatments and diagnostics are needed to track their frequency and separate them from their obstructive counterpart. Treatment of central apneas with increased pressure can increase the occurrence of central apneas, leading to worse outcomes. This makes distinguishing between events critical and proper treatment of obstructive apneas reduces the occurrence of central apneas [5].

II. Respiratory Impedance & FOT

A popular method for distinguishing if a patient's airway is collapsed, is by their airway impedance signature. Airway Impedance, or respiratory impedance, is a complex quantity, comprised of real mechanical resistance (R_Z), and the frequency dependent reactive component, Reactance (X_Z). Reactance is comprised as the sum of inertance of the medium, depicted as (I) and analogous to inductance, with the compliance depicted as (C), analogous to electrical capacitance [6], Eqn's [1 & 2]

$$Z = R_Z + j X_Z \quad (1)$$

$$X_Z = X_I + X_C \qquad X_I = j\omega I \qquad X_C = 1/j\omega C \quad (2)$$

Respiratory disorders like sleep apnea can significantly change impedance parameters when the airways are obstructed, at low frequency, resistance increases as reactance falls. Whereas in central apneas, no significant change is observed. It has also been shown that resistance of the airways increases over time in patients with COPD and asthma [7], and more recently has been shown to be an effective tool in monitoring changes in lung health among COVID-19 patients [8]. Therefore, tracking a person's respiratory resistance could lead to the early detection of a progressive disease. Measuring respiratory impedance can be done non-invasively by Forced Oscillation Technique (FOT) [9]–[12]. This method involves inducing oscillations in a person's lungs and airway tissue by using a speaker, by modulating the fan of a CPAP (Continuous Positive Airway Pressure) or piezo elements [13]. These oscillations in pressure induce a flow response within the lungs, airways, and tubing, which contains a particular phase and magnitude shift from the pressure wave that generated it. Referencing phasor mathematics, we can show that the ratio of Pressure and Flow phasors resulting from the FOT can deliver a measurement of mechanical impedance. Where P represents pressure, F represents flow, R is the real component and X the imaginary, Z gives us the impedance phasor which can be broken back into its R and X components by $A \cdot cos(\theta)$ and $A \cdot sin(\theta)$ respectively.

$$P = R_P + j X_P \qquad F = R_F + j X_F \qquad A = \sqrt{R_2 + X_2} \qquad \theta = tan^{-1}(X/R) \quad (3)$$

$$P = A_P \angle \theta_P \qquad F = A_F \angle \theta_F \qquad Z = A_P / A_F \angle(\theta_P - \theta_F \quad (4)$$

$$R[Z] = A \cdot sin[\theta] \qquad X[Z] = A \cdot cos[\theta] \qquad 5$$

This measurement of impedance depends heavily on the ability to accurately measure pressure and flow signals, compute their FFT and phasor division. This also requires selection of a high enough amplitude FOT to distinguish from breathing noise. Figure 1 shows the spectral nature of breathing data. The current methods for measuring respiratory impedance can be improved by computing sine correlation in analog as opposed to digital and by maintaining an FOT frequency outside the heavy noise band caused by breathing. Studies done by our lab have indicated that high frequency low amplitude (HFLA) FOT is a viable tool in distinguishing between central and obstructive apneas, though at some frequencies, the noise can really obscure the measurement [14].

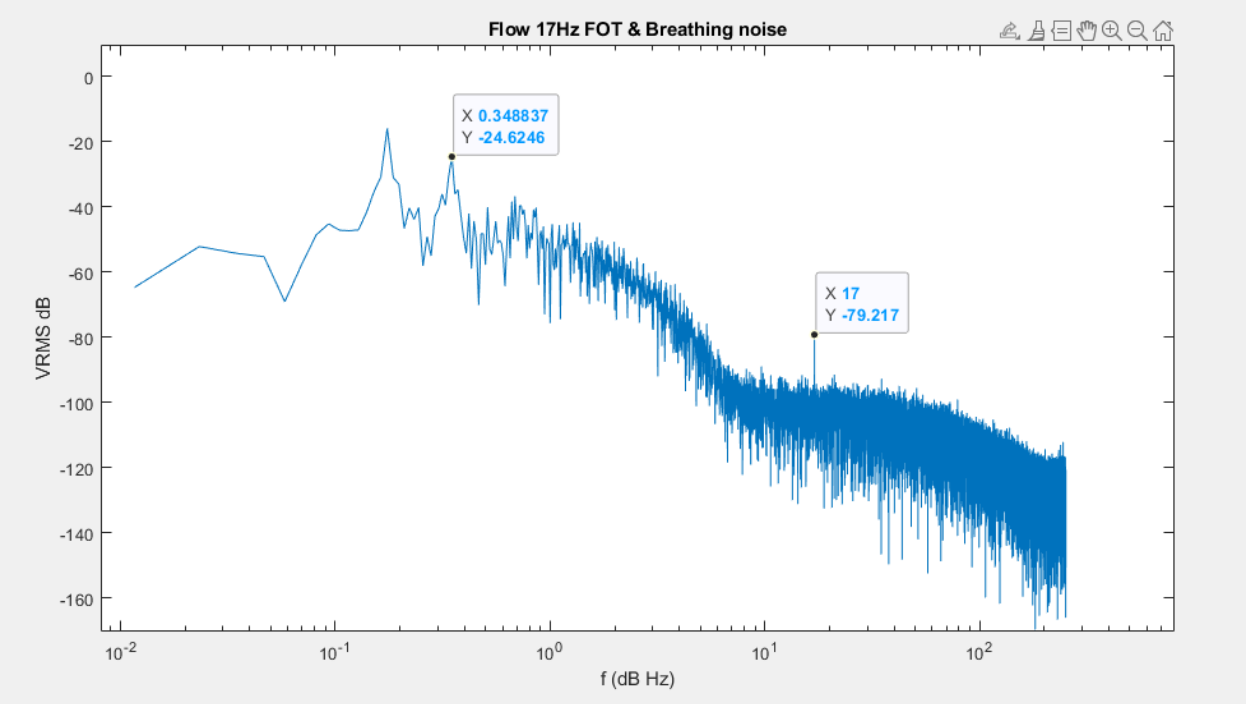

***Figure 1**: 17Hz FOT with Superimposed Breathing Noise*

III. Predictive & Preventative Therapy

To further highlight the importance of continuous impedance monitoring, work has been done at NovaResp to use artificially intelligent networks to forecast when an apneic event is coming [15]. However, these algorithms rely heavily on accurate tagging of events for algorithm training. Events are currently tagged using high amplitude FOT only after an event has been longer than 10 seconds, as the algorithms used for triggering FOT and the FOT itself requires time to initiate and compute on CPAP devices. Apneic events are defined by this 10 second threshold, but this excludes 9 second events, considering them as non-apneas. A continuous measurement and analysis of events would show the behaviour and level of obstruction through an entire apneic event, potentially leading to a distribution of events as opposed to a binary classification. This continuous monitoring would allow for better tagging and thus training of these neural networks for improved prediction and forecasting of events.

IV. Impedance Measurement System

Currently, the systems used to generate, capture, and process the pressure and flow signals to extract respiratory impedance contain four major components: [Figure 2]

- Waveform Generation (Speaker/Fan/Frequency)
- Sensors (Pressure & Flow)
- Data acquisition and processing
- Mechanical coupling to the airways

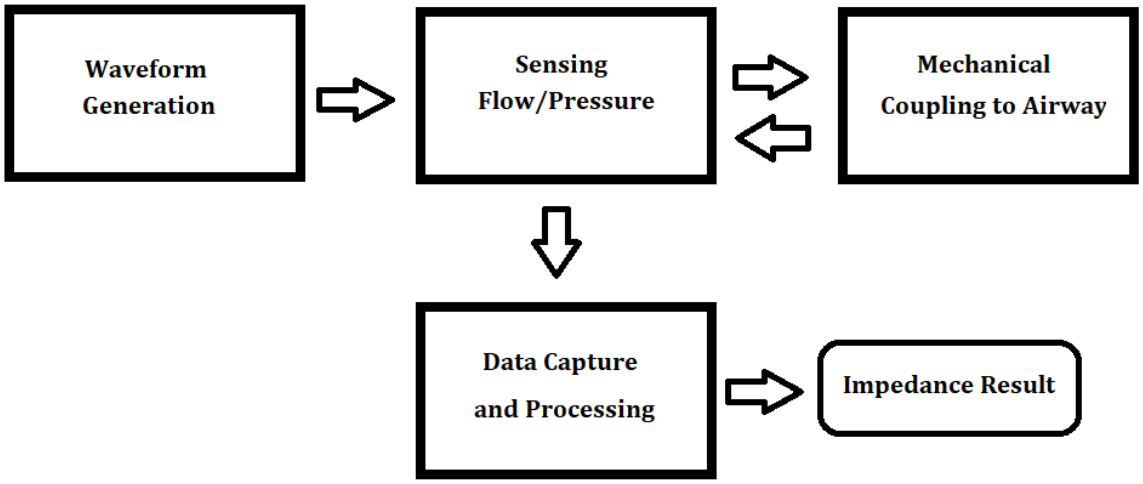

***Figure 2**: Major Components of FOT Impedance Measurement*

A. Sensors

One of the most commonly used sensors, due to its relatively low cost and simple design is the Fleisch pneumotachograph (shown in Figure 3 (*left*)). It measures flow by incorporating a resistive element between two ports of a differential pressure sensor. The drop in pressure across the resistive element due to a non-zero flow can be measured by digitizing the analog voltage produced from the differential Wheatstone bridge (Figure 3 (*right*)) sensor and calibrated based on the resistivity of the separating element. The pressure waves are also measured by a similar style sensor, but with a lower sensitivity and range, and being referenced to atmosphere.

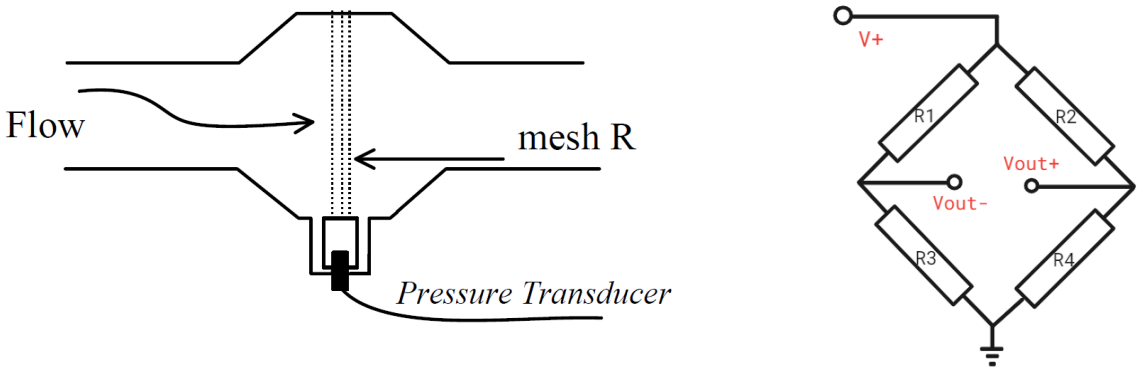

***Figure 3**: Mesh Pneumotach (Left) Wheatstone Bridge Sensor (Right)*

These types of flow sensors are often large and can be very expensive. In addition, they also pose the issue of being resistive in the path of breathing. Other sensor options are highly resistive, uni-directional (only measure flow in one direction), have moving parts, or have specific requirements for operation. The following list of sensors have been determined with their unique attributes and functional requirements [16].

Air Vane Meter:

- Spring loaded potentiometer in direct contact with fluid.

- Voltage drop is proportional to flow rate. Highly resistive, bulky.

Hot wire:

- Heated wire with temperature sensor.

- Temperature drops proportional to mass flow.

- Cold-wire system implements a second wire to give reference to ambient temperature

- Low resistance, Unidirectional

Vortex sensor (Von Karman vortex):

- Laminar flow

- A disruptor causes a vortex whose frequency is proportional to fluid velocity

- Requires laminar flow

- Highly complex, resistive, bulky.

Ultrasonic Flow sensor:

- Calculates the flow rate based on the difference in time of flight of the sound waves.

- Compact, low resistance,

- Bi-directional (if implemented properly), low complexity.

Membrane sensor: [17]

- MEMS Electronic membrane in air stream.

- Temperature sensor on up and downstream sides, a heater in placed inside the sensor and the temperature difference is proportional to mass flow

- Highly non-linear, low resistance, high complexity

Pneumotachograph: [18]

- Pressure difference across resistive element is proportional to flow rate.

- Highly linear

- Resistive, bulky

B. Mechanical Coupling & Waveform Generation

Concerning waveform generation, FOT has been achieved in creative ways, although two main methods seen in commercial applications, are by speaker and fan modulation. Some CPAP machine manufacturers have adopted the latter, where during continuous positive airway pressure therapy, the fan used to generate the positive pressure is also modulated by a relatively high amplitude 4Hz sine wave. The pressure and flow are digitized, and the magnitude of impedance is used to determine if the airway is obstructed. This process can take some time however, current

methods present on a commercially available CPAP from ResMed cannot distinguish between central and obstructive events until 10 seconds after an event has occurred, and the amplitudes of the FOT are quite high, raising the risk of arousing the patient if done continuously rather than intermittently. Speakers have been used in handheld commercial devices to measure airway impedance, although they are large to accommodate low frequency, high amplitude sine wave generation. Increasing frequency of the FOT would increase efficiency of electrical to mechanical power transfer in the generation of infra-sound waves within the speaker. Increased frequency also reduces the in-band noise profile due to separation of FOT from breathing spectra. These combined effects would relax requirements on the size and power of the signal source. However, raising the frequency of FOT poses an issue with sound wave propagation in the CPAP system, where higher frequencies may be affected by resonance.

The mechanical coupling for the system involves tubing, approximately 2 meters in length with a CPAP machine on one end and a mask and patient on the other. The CPAP system emulates a long tube, closed at the end of a variable geometry. The CPAP machine exerts pressure using a fan and has a fairly high resistance, emulating the closed end of a tube as a boundary condition, i.e. displacement is assumed to be effectively zero across the boundary. The two ideal scenarios during spontaneous breathing are when the connected geometry length is reduced to zero, and the other when length is infinitely elongated. The first harmonic of the system when length is reduced to zero, exists at one half wavelength. This requires that frequencies close to $S/2\lambda \approx 86Hz$, where the speed of sound, $S \approx 343m/s$ and wavelength $\lambda \approx 2m$, should be taken into careful consideration when trying to make measurements of impedance, as small changes in connected load impedance (airway) will cause large variations in flow amplitude and phase. This affect could lead to a more sensitive decoupling of central and obstructive apneas, though absolute measurements of impedance for detecting respiratory disease may be less accurate based on differing geometry and resonance.

C. Data Capture & Processing

Once the signal has been generated, injected, sensed, and digitized, the bit stream is passed through an STFT (Short Time Fourier Transform) frequency correlation function using a sliding window, and the magnitude and phase of the spectrum is maintained. The spectrum is then digitally band-pass filtered to remove unwanted noise, and a local maximum is obtained. The magnitude and phase of this maxima is then used in the phasor division shown earlier. 4). Others have opted for a less computationally intense method, such as the Hilbert transform to only correlate with the frequency of interest [14].

However, digitization and computation of signals inherently has its own set of problems with quantization and round-off errors, leaving some of the signal integrity behind, especially when dealing with very low amplitude signals. On the generation side, the frequency being generated has to fit precisely in one of the bins of the STFT, otherwise the correlation function will not be as sensitive. One can get close by following the relationship below, but this still leaves room for error, as the demodulation and generating waveform are not from the same source. This relationship, which accommodates multiple FOT frequencies being measured at once, is shown here:

Given that $f(s) = 1(T) \cdot W(s)$ where T is real and positive and $W(s)$ is a positive integer.

$$F(r) = f(s)(W(s)) = 1(T) \qquad F(b)(n) = n(T) \qquad n = 0,1,\dots, W(s) - 1 \qquad 6$$

$$\textit{Generally,} \quad F(i)(n) \in F(b)(n) \quad \textit{when} \quad hcf\ F(i)(n) = k(T) \quad k \in \mathbb{N} \qquad 7$$

Thus one must choose $\{F(i)\}$ or $f(s)$ or $W(s)$ so that the relationship $hcf\ F(i)(n) = k\ f(s)(W(s))$ holds.

Where T is the time period being measured in seconds, $F(r)$ is the resolution of the STFT window, $f(s)$ is the sampling frequency, $W(s)$ is the window size in samples, $\{F(i)\}$ is the set of frequencies to be measured, $\{F(b)\}$ is the set of bins contained within the STFT window, n is the bin number, k is an integer scaling factor, and $hcf(\,)$ gives the highest common factor of the set.

Although the data capture and processing circuitry consume slightly less power than its waveform generating counterpart, the SNR limitation is further compounded by the inability to separate the

FOT signal from in-band noise at low power. Improving the system's ability to differentiate between signal and noise, would relax requirements on waveform generation.

V. The Lock-In Technique

The power of the Lock-In technique comes from its homodyne mixing. By stimulating a system $h(t)$ with a sinusoidal tone $x(t)$, and mixing the systems response $y(t)$ with a 0-degree copy of the tone $sin(\omega t)$ and a 90-degree version of that tone $sin(\omega t + \pi/2)$, one can effectively measure with a high degree of accuracy how that system responds to that stimulus at ω.

$$Given: \quad x_1(t) = sin\,\omega t, \quad x_2(t) = sin\,\omega t + \pi/2 \quad and \quad x_1(t) * h(t) = y(t) \qquad 8$$

$$y(t) \cdot x_1(t) = I_{DC} - \frac{1}{2}cos\,2\omega t \quad and \quad y(t) \cdot x_2(t) = Q_{DC} - \frac{1}{2}cos(2\omega t + \pi/ \qquad 9$$

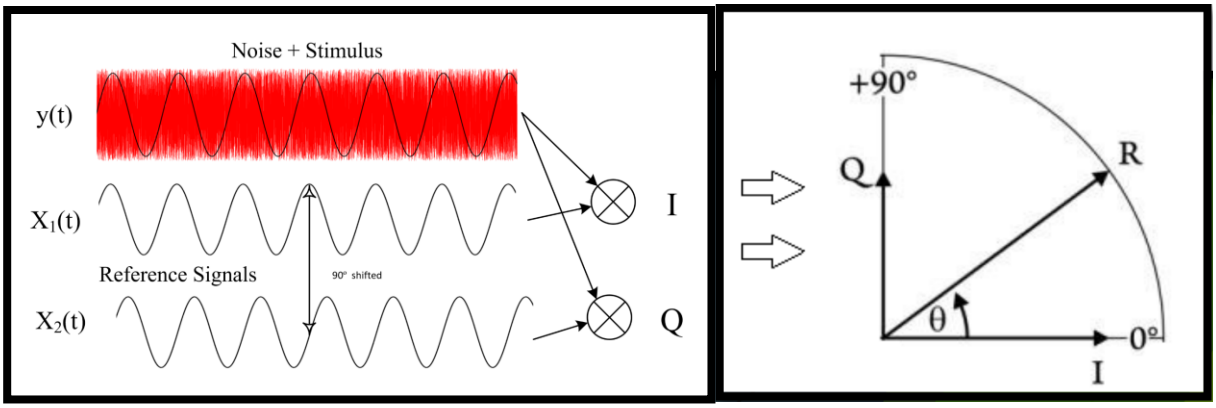

***Figure 4**: In-Phase & Quadrature Mixing*

This self-mixing technique shown in Figure 4, generates a DC component (I_{DC} and Q_{DC}) and a double frequency component, whose amplitudes are both correlated to how in phase $y(t)$ was with $x_1(t)$ and $x_2(t)$ at the frequency ω . By low pass filtering each mixed output very close to DC, the double frequency components and neighboring noise can be eliminated, leaving a DC correlation factor behind. These two DC values represent the magnitude of the real and

imaginary parts of the signal being measured, when compared to the reference. The closer the low pass corner frequency is to DC the more the system can reject noise, though at the expense of settling time. With a sufficiently low cutoff frequency, signals buried in noise thousands to millions of times greater than itself can be measured.

This lock in amplifier would improve the current FOT measurement system by reducing power consumption and complexity. A typical Lock-In topology is shown in Figure 5. This topology shows how the input signal is amplified before being band-pass filtered to remove excess noise. The signals are then mixed by an in-phase and quadrature signal and filtered to extract their DC correlation factors.

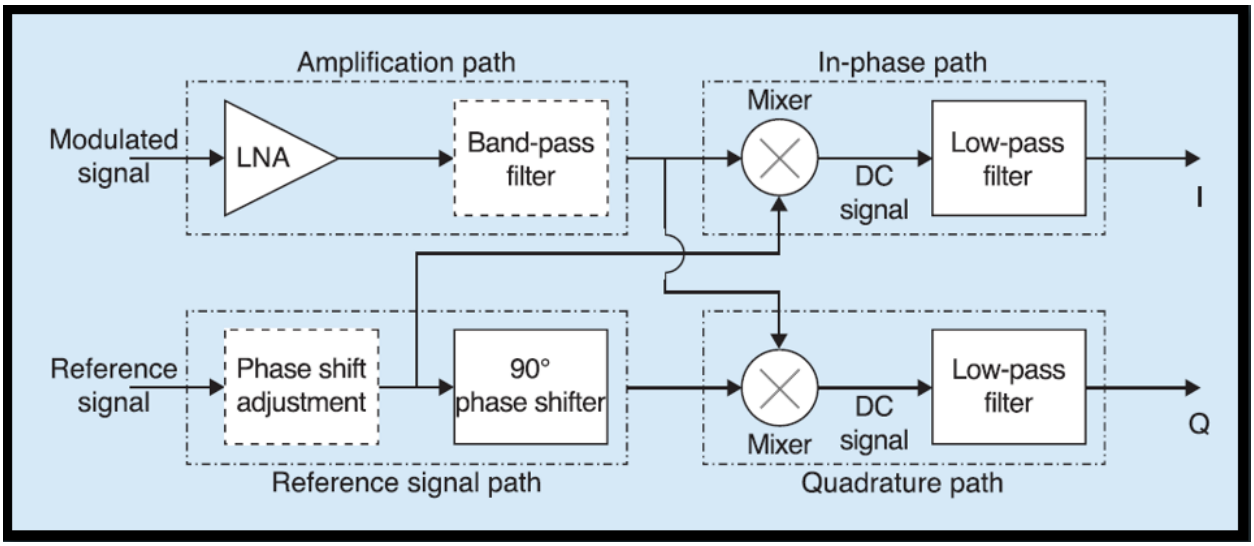

***Figure 5**: Typical Lock-In Topology [19]* © *[2017] IEEE*

These DC correlation factors can be used to precisely extract the phase and amplitude of the pressure and flow signals. By knowing the I and Q values, the Cartesian representations for Pressure and Flow from Eqn. 3) i.e. R and X can be treated as I_{DC} and Q_{DC} respectively. Simultaneously, the sum of squares and inverse tangent transformation can be used to extract the polar values $A\angle\theta$ and ultimately the system impedance (Eqn's 4 & 5)

VI Conclusion

In conclusion, there exists a gap in the literature for miniaturization and reduction of power and cost for respiratory monitoring systems like non-invasive ventilators. In particular the synchronous demodulation of FOT waves for improving the signal lock over long time periods during sleep, and reducing the cost, size and power of computing respiratory impedance. There is also exists a gap for a resistance-less respiratory flow meter that can achieve positive and negative flow rates, in a highly linear fashion, that also withstands the channel variations during breathing. In this thesis I explore a flow meter that can provide similar benefits as the most widely used flow metering devices, but without resistance in the path of breathing, and a lock-in amplifier that effectively maintains a synchronous lock on FOT signals that consumes far less power than its MCU and STFT counterpart in a highly compact CMOS process.

Chapter 3 : Respiratory Bidirectional Ultrasonic TOF Flow Sensor Resilience to Ambient Temperature Fluctuations

Authors:

Gregory Begin,

Karama M. AL-Tamimi,

Hamed Hanafi Alamdari,

David Roach,

Michael Schmidt,

Kamal El-Sankary

Published, IEEE Sensors Journal, © 2021 IEEE. [20]

This manuscript has been modified from its original format to conform to the structure of this dissertation

Abstract

Measuring fluid flow velocity using ultrasonic based sensors has been established for some time, however implementation of this technology in respiratory systems is relatively recent. This paper presents the design of a respiratory flow sensor made possible the by air-coupling ultrasound principle. A prototype has been developed as a proof-of-concept. To enhance the signal to noise ratio (SNR), the modulated ultrasound arrival time is translated to a digital word using Time-to-Digital Conversion (TDC). Hence, the respiration is digitally captured in real-time to offer a synchronous respiratory monitoring. The near-zero deviation is further alleviated by Least Mean Square (LMS) technique accomplished off-line. Down to 0.03 L/s of resolution and over 95% of

linearity is achieved. The bidirectional transmit/receive echo signals have been leveraged to provide a system level cancelation of the environmental conditions affecting measurement accuracy. The developed sensor was used on adult volunteers and tested experimentally using an ASL5000 servo lung simulator. The results validate the system functionality in the presence of real-world conditions.

I. Introduction

Cost-effective and accurate measurement of breathing signals are the foundation of monitoring and control systems on mechanical ventilators [21]. The importance of ventilatory sensors has been echoed since the COVID-19 outbreak [22], [23], as ventilatory treatment based on lung protective ventilation strategies are completely dependent on accurate and real time sensors. Whether the ventilation is conducted invasively through intubation in the intensive care unit (ICU), noninvasively using face masks in post-anesthesia care units (PACU), or on positive airway pressure (PAP) machines, measurement of airflow and air volume helps to provide lung protective ventilation [23] by avoiding ventilator induced lung injury (VILI) caused by overdistention of the aerated lung (volutrauma), or repeated collapse and reopening (atelectotrauma) [21], [24]. When considering a ventilation system, minimizing the mechanical load against breathing is essential.

Most airflow sensors use a Fleisch style pneumotachograph, where the differential pressure across a known resistance is utilized to calculate airflow [21]. This introduces an unwanted resistance in the path of breathing. Figure 6(a) shows a simplified block diagram of sensing flow and applying postprocessing for diagnostics and treatment. The bottleneck in these types of systems is tracking breathing flow with good resolution. Typically, the pneumotach incorporates a differential pressure sensor as shown in Figure 6(b). Flow is calculated using this simple relation:

$$Q = \Delta P \square R \square \qquad 10$$

where Q is the flow rate in L/s, P is the pressure in cmH2O, and R is the pneumotach resistance in cmH2O/L/s, which is a sheet of narrow-mesh screen placed perpendicular to the direction of

flow [25]. In addition to the resistance fluctuation, the accuracy of a pneumotach also depends on the precision of the transducer that measures its differential pressure.

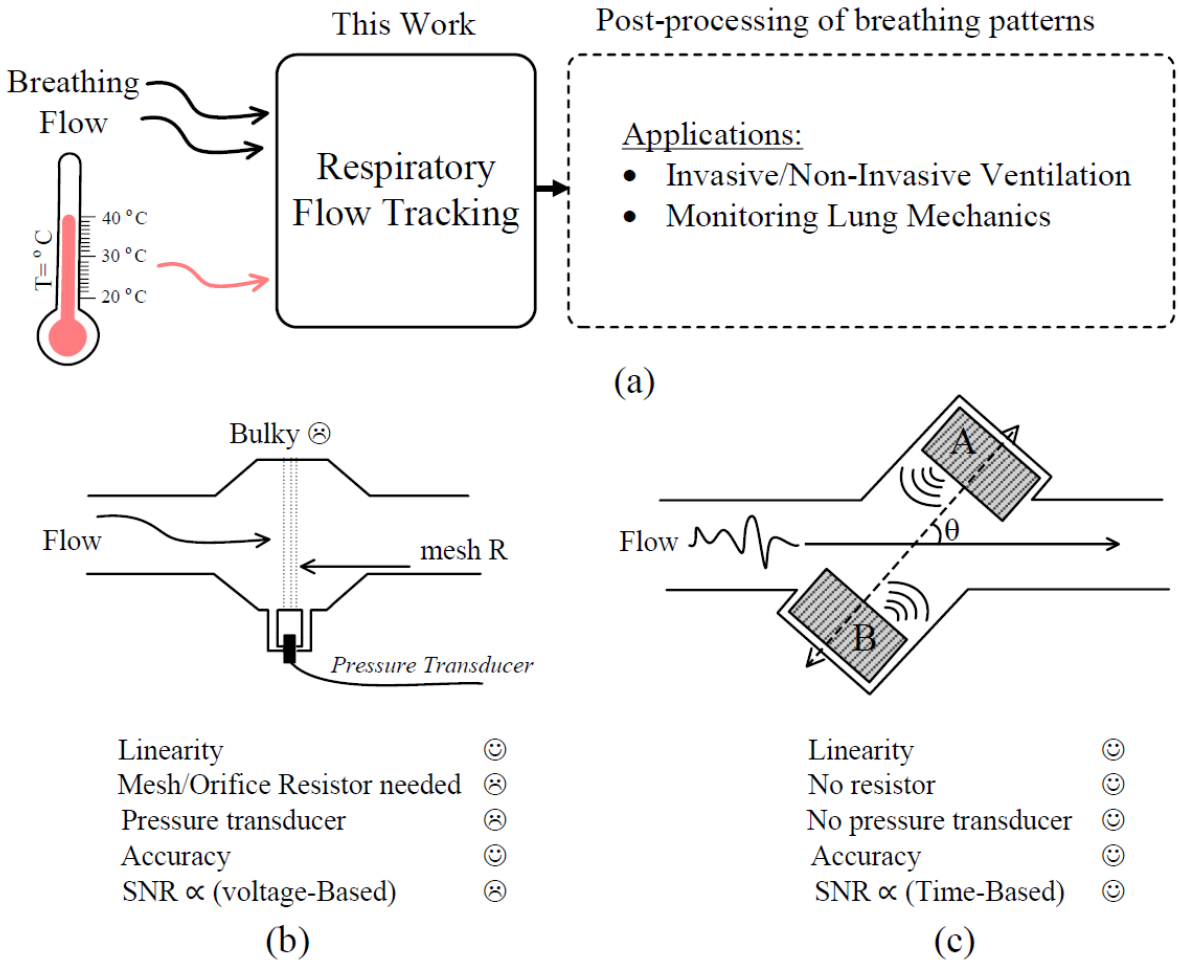

***Figure 6**:(a) Intuitive representation of the ongoing respiratory sensing. for respiratory tracking (postprocessing engine for different applications). (b) Pneumotachograph instrument is used to indirectly derive the rate of respiratory flow by measuring the pressure differential (ΔP) across a barrier of known mesh resistance using pressure sensor(c) ultrasonic air-coupling TOF (time-of-flight) configuration.*

Motivated by the requirements, the principle of an ultrasonic flowmeter has been leveraged to develop a non-contact, medium independent, high resolution, real-time respiratory tracking sensor augmented by the direct digitization of the phase difference between ultrasonic waves. In this case, the transit time between the two acoustic transducers is modulated by the flow rate inside the tube (Figure 6(c)). This article is organized as follows. Section II provides a background and problem statement. Section III describes the design of the overall system architecture and elaborates on the

PSoC (Programmable System on Chip) prototype implementation. Section IV shows different experiments and *in-situ* measurements. Concluding remarks are presented in Section V.

II. Background Overview and Problem Statement

A. Overview

Disorders affecting the respiratory system can result in an intermittent and abrupt reduction in blood oxygen levels and can have long-term serious health consequences. Patients are often diagnosed using high-cost equipment in a specialized clinical laboratory. Such solutions are in general bulky and not affordable leaving the majority of respiratory conditions undiagnosed and untreated. Diagnostic and monitoring approaches, for example forced oscillation technique (FOT), allow for the study of the mechanical properties of the respiratory system via the systems measured response to small time-varying forces [25]. FOT methodology utilizes pressure signals (force) to evoke a flow (displacement) response. The relationship between pressure and resulting flow are then analyzed, yielding respiratory impedance which consists of respiratory resistance and reactance. While the advantage of FOT is the noninvasive methodology, the probing oscillations often have to be generated at larger amplitudes to have a better signal-to-noise-ratio (SNR), which can cause discomfort in some patients. Having an acceptable SNR is an essential trade-off in the application of FOT, especially if performed during sleep on positive airway pressure (PAP) machines [26], [27]. This trade-off echoes the need for high accuracy airflow sensors. Recently, respiratory sensing approaches based on micro-electro-mechanical systems (MEMS) [28]–[32], Piezoresistive materials [33], phase tracking doppler detection technique [34], and in time delay ultrasound [35], [36], have been reported. The latter approaches are promising as the technology of semiconductor foundries are scaling down. Time delay ultrasound, known as time of flight (TOF) can be estimated using different parameters such as amplitude, phase, or frequency (i.e., doppler effect) [37]–[40]. Depending on the application, some parameters are preferred over others. By inspection in the literature, the ultrasonic flowmeter has shown efficiency in a wide range of applications such as vibration measurement, oil flow estimation, distance measurement, positioning sensors for robotics etc. [41]–[51]. Also, it shows excellent accuracy as a temperature sensor [52]. In [53], [54], two approaches of analog and mixed-signal systems have been reported with respiratory monitoring as one of their applications.

B. Problem Formulation: (Goal: Miniaturized Sensor)

The global covid-19 pandemic echoes the necessity of portable and accurate respiratory sensing and support for monitoring and treatment of diseases such as acute respiratory distress syndrome (ARDS). To comply with these requirements, the design of such portable sensors would need to be in sync with the technology roadmap. This prototype focuses on the design of an interface which translates the raw information (flow) from the sensor's vital signs into a digital stream via an optimal signal quantization in the time-domain using TDC (Time to Digital Conversion). This offers a portable and cost-effective respiration screening solution. By method of direct digitization, we eliminate the phase gradient block, and the discrete ADC. Our long-term aim is essentially to develop a fully integrated, low-cost respiratory monitoring sensor that is portable and can be used as a screening tool to improve diagnosis and monitoring of a variety of respiratory conditions.

III. Design Evolution

This section explains the conceptual evolution of the ultrasonic flow sensor architecture steps.

A. Concept: Time of Flight (TOF)

The ultrasonic sensors generate and receive amplitude modulated (AM) acoustic sine waves by bandpass filtering an input electrical square wave around its fundamental mechanical resonance frequency. Then, generating an AM electrical sine wave across the opposite transducer via the air pressure disturbances created by the first transducer. In general, the ultrasonic flow meters work based on two different principles:

1) Doppler effect ultrasonic flow meter: where the frequency shift is measured
2) *Time of flight ultrasonic flow meter:* where the time delay of the acoustic echo is used as the variable to translate the flow rate.

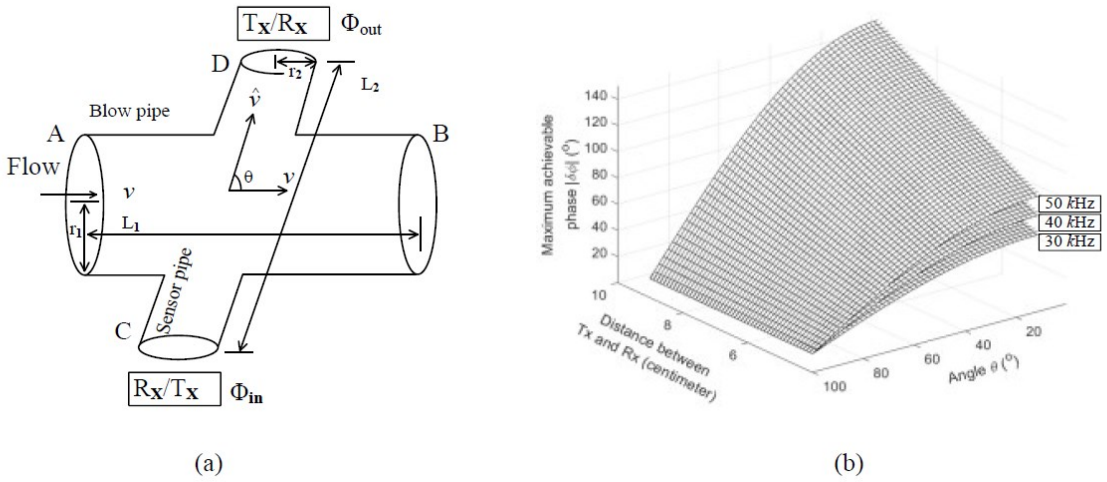

***Figure 7**: (a) Equivalent cylindrical tube geometries (b) 3D plot of maximum phase achieved as a function of frequency, Tx-Rx distance, and angle.*

The realization of the proposed sensing platform can be broken down as follows:

Consider the sensor tube shown in Figure 7(a) where TX and RX denotes to the transmitter and receiver of the air-coupled ultrasound transceiver, respectively. According to the fundamental physics, the time needed, *t*, by a wave with a speed *s* to travel a distance *d* as follows:

$$t(in\ sec) = d(in\ m) \square s(in\ m/s) \square \qquad 11$$

By applying cylindrical tube geometries shown in Figure 7(a), if *t* refers to the time delay between $\emptyset \square in \square$ and $\emptyset \square out \square$ and *T* is the time interval of the ultrasound excitation signal (*T= 1/f*), then the phase difference, $\Delta\emptyset = \emptyset \square out \square - \emptyset \square in \square$, can be mathematically given as:

$$\Delta\Phi = 2\pi * 1 \square T \square * t = 2\pi \square T \square \quad L \square 2 \square \square v \square sound \square + v \square p \square \square \square \square \square t \square \qquad 12$$

where $L \square 2 \square$ is the distance between the transmitter and receiver, $v \square sound \square$ is the velocity of sound and roughly equal to 343 m/s, $v \square p \square$ is the velocity component of respiration. The speed of $v \square p \square$ is proportional to inspiration and expiration ($\approx 0.1 \rightarrow 10$m/s for tidal breathing). Hence, the derivative of the phase difference, $\partial\Phi$, can be related to change in the respiration velocity (the argument), $\partial v \square p \square$, as follows:

$$\partial\Phi \approx v_{sound} \gg v_p = -\frac{2\pi L_2}{T v_{sound}} K_p \partial v * \cos\theta \quad (13)$$

where θ is the angle between the two cylindrical tubes (i.e., the relative angle between the transmitted ultrasonic beam and the respiratory flow where $v_p = v\cos\theta$ is the applied respiration velocity at point A in Figure 7(a). We can model K_p as the gain of the ultrasonic medium in radian/m/s. Unlike [27], there is no phase gradient block. The phase difference $\Delta\emptyset$ is directly translated through clocked counter with N states to formalize a multibit TDC configuration with a resolution of 2^N (details in Section III.D). The $\Delta\emptyset$ is related to the time of flight (TOF) by expression (12). In other words, *t* is nothing but the TOF. TOF will be used as the terminology in the rest of this article. Prior validation for an ultrasound-based system for respiratory applications has been done before [35], [36], [55]–[59]. However, these implementations either suffer from temperature dependency, resolution limitation, or the lack of compact implementation.

B. Optimal Design Parameters

There are mainly three parameters needed to be designed for an optimal operation: 1) frequency of the excitation signal (F); 2) distance between Tx and Rx and 3) the angle θ. Based on (13), it is obvious that the phase shift sensitivity is directly proportional to the distance of separation L_2, and the ultrasound excitation wave frequency, while it is inversely proportional to the angle θ for a given v_p as depicted in Figure 7(b). The air-coupled transducers operating at 40 k Hz have been chosen because they are cost effective and widely available transducers, as well as being low enough frequency to not cause wraparound measurements of phase. The tube's design parameters are presented in Table 1. With these specifications, the equation (13) also shows that the phase shift ($\Delta\emptyset$) of the ultrasound wave is directly proportional to the component of inspiration/expiration velocity along the sound travel path, ∂v_p.

TABLE 1

Symbol	Quantity	Value/Unit
L_1	55	55 mm
L_2	Tx $\rightarrow$ Rx distance	30 mm
θ	Angle between direction of flow and ultrasonic wave propagation	45º
r_1	Cross sectional radius	10 mm
r_2	Transducer tube radius	6.75 mm

***Table 1**: Geometric Parameters for Ultrasonic Sensor*

C. Elimination of Temperature Effect: Bidirectional

The measured phase changes are being modulated by both the fluid velocity within the device, and the speed of sound propagation within the fluid (air). Any changes to the speed of sound will cause an error in measurement, as the waves will take differing amounts of time to arrive at the receiver. Several parameters, like humidity and pressure will affect the speed of sound. Of those, temperature modulates the speed of sound the most dramatically [55]–[57], [59]. It is well established that the source of this effect comes from this relationship:

$$v_{sound} = 331 + 0.6 * Temp \qquad 14$$

where *Temp* is the air temperature in ºC. The speed of sound is roughly 346 m/s in room temperature air. This is faster than at freezing temperature speeds of less than 331 m/s. Based on the cylindrical tube geometry in Table 1, the deviation of TOF (or digital word) due to fluctuation of temperature is shown in the contour Figure 8. It is obvious that the 20 ºC change in temperature (15~45 ºC) causes around 5 LSB (least significant bit) deviation from the nominal value during the inhalation and exhalation. The deviation increases proportionally to the range of the temperature fluctuation, resulting in deflection in the recorded data under different ambient

conditions.

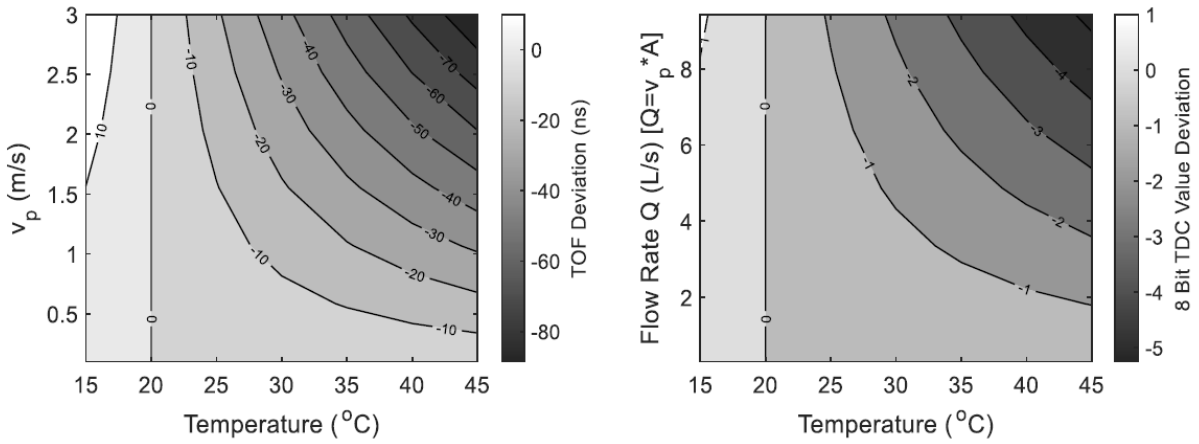

***Figure 8**: Temperature effect on TOF measurement accuracy for unidirectional.*

To eliminate/alleviate this issue, we adapt the tube design (Figure 7(a)) as the simplified diagram shown in Figure 9(a). The tube has been prototyped in the lab facility at NovaResp Technologies Inc (Halifax, Canada). using a 3D printer as illustrated in Figure 9(b).

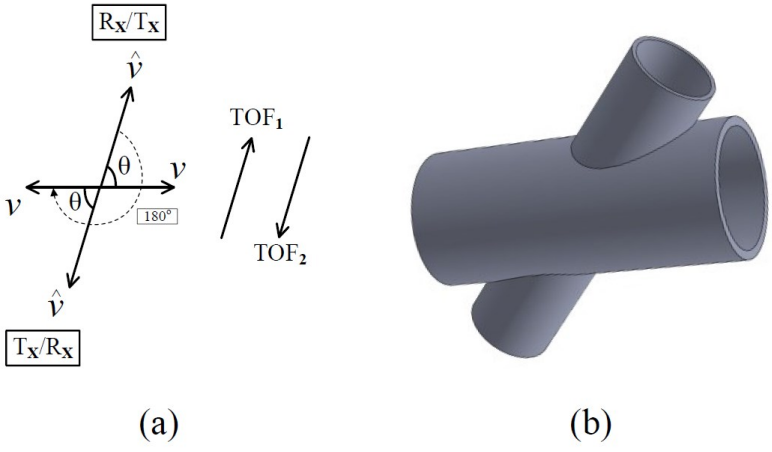

***Figure 9**: (a) Simplified illustration of bidirectional vectors Transmit/Receive TOF calculation (b) 3D design tube made in-house at NovaResp Technologies Inc (Halifax, Canada). for prototype testbench*

The two piezo-crystals are mounted to function both as transmitter and receiver. In this configuration, the ultrasonic flow measurement is done by measuring the phase difference in both directions sequentially and taking their difference. To avoid interference and ringdown effects

from transmission, the time between sequential transmissions is roughly 1ms. Thus, the travelling time of the acoustic beams TOF_1 and TOF_2 are as expressed in (15) and (16), respectively:

$$TOF_1 = \frac{L_2}{v_{sound} + v_p \cos\theta} \quad (15)$$

$$TOF_2 = \frac{L_2}{v_{sound} - v_p \cos\theta} \quad (16)$$

$$v_p = \frac{L_2}{2\cos\theta}\left(\frac{TOF_2 - TOF_1}{TOF_1 \, TOF_2}\right) \quad (17)$$

$$v_{sound} = \frac{L_2}{2}\left(\frac{TOF_1 + TOF_2}{TOF_1 \, TOF_2}\right) \quad (18)$$

By taking the two $TOF_{1,2}$ measurements, one with and one against the drift velocity, the ratio of their product and sum can be used to isolate the drift velocity (17), and the speed of sound (18). The flow rate, Q, inside the cylindrical tube can be estimated according to its geometry. In this case, the Q can be derived as:

$$Q = \int_A v_p \cdot dA = v_p \pi r_1^2 \quad (19)$$

where A is the area of cross-sectional sensor tube and r_1 is the radius of the sensor tube (designed in Figure 6(a)). In summary, the ultrasonic flow meter offers the following traits:

- Obstruction-less flow
- Unaffected by changes in temperature, density or viscosity due to its bidirectional configuration
- Low flow cut-off (i.e., better resolution)
- Accuracy reaches ~ 99%

D. Model Validation

The simplified high-level diagram of the system is represented in Figure 10. Before going into detail, the sensor behavioral model was simulated using MATLAB Simulink. Unless otherwise indicated, system parameters are: N = 64 levels (8-bit TDC), excitation frequency F = 40 kHz. The input/output transfer characteristic is carried out as illustrated in Figure 11. This shows how the

measured phase is modulated by breathing-scale changes in flow rates. Second, the transient testbench has been carried out based on data of a 12kg, 2-year-old child, with permission from [60]. The length of the data set is eight minutes; however, it was truncated to one minute for display purposes. The objective of using already measured data as a perturbation (instead of sinusoidal) is to demonstrate the design effectiveness in extracting the data accurately in the presence of quantization noise. The extracted/reconstructed normalized data from of the TDC is shown in Figure 12 with its spectra. It clearly shows the breathing rate (BR) component at around 0.3 Hz (BR = 18 per minute).

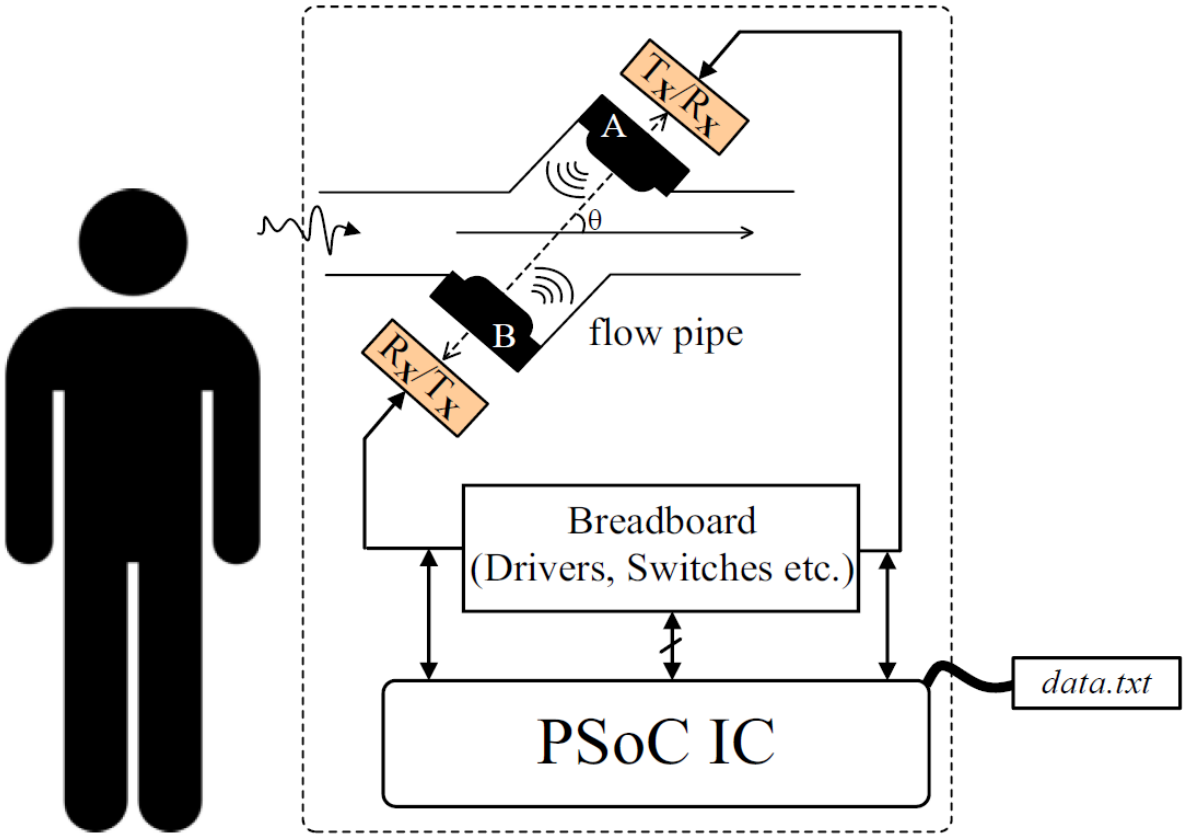

Figure 10:. *High level overview: realization of the proposed respiratory sensing platform incorporating TDC withing the PSoC.*

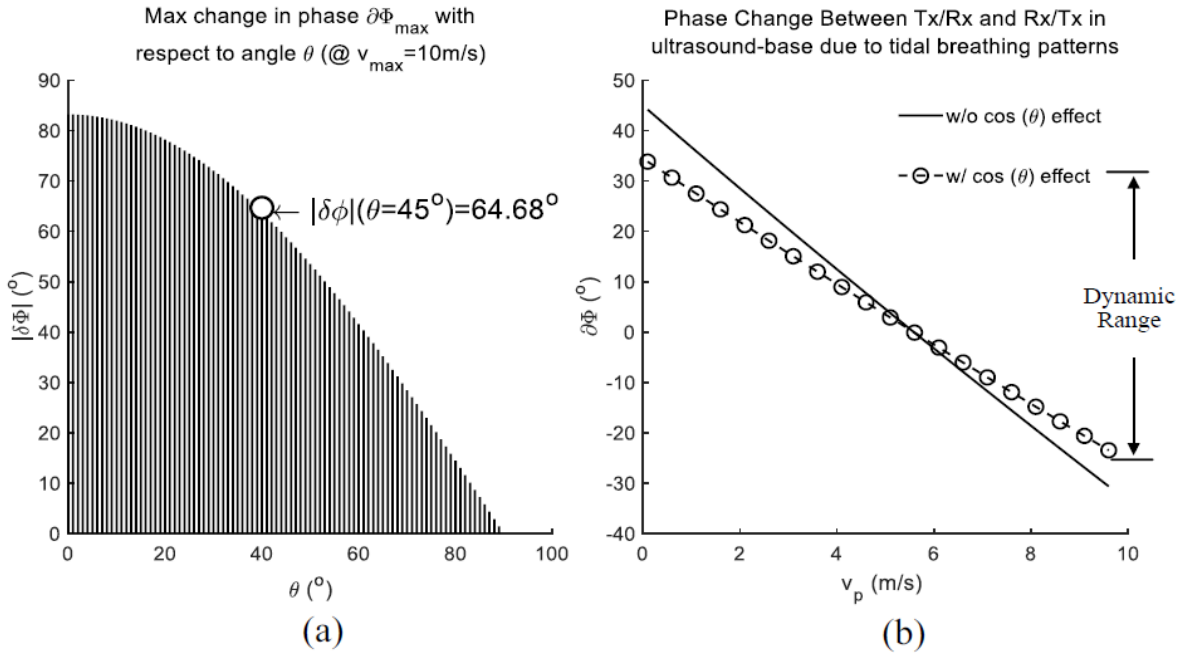

***Figure 11**: Maximum phase that can be achieved with respect to angle θ (left) and phase against respiration velocity (right). The modulated phase is centered around zero.*

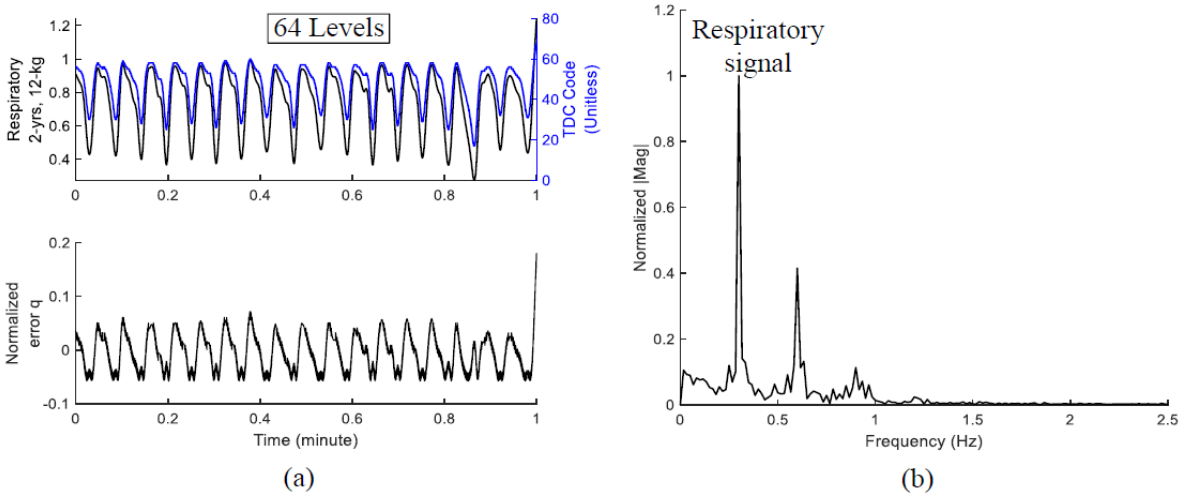

***Figure 12**: Reconstructed respiratory signals: (a) Input (black) signals and extracted respiratory signals (blue) (b) The corresponding frequency spectra of the extracted respiratory signals are dominated by respiration at 0.3 Hz, which is approximately the breath rate (BR).*

IV. Prototype Implementation

The ultrasonic flow sensor has been prototyped in-house as a proof-of-concept. The main components involved in this implementation are: 1) Two 40 kHz transducers, 2) a 3D printed housing, 3) a PSoC chip and peripherals, 4) breadboard and wires, 5) An ASL5000 lung simulator machine for generation of breathing patterns, 6) a pneumotachograph as a reference. And 7) External components, including: MOSFET drivers for the ultrasonic transducers, potentiometers, resistors and a quartz crystal for PLL. The 40 kHz transducer is the UR-1240K-TT-R from PUI Audio, Inc. and its specifications are shown in Table 2.

TABLE 2

Transducer Specifications

Parameter	Value/Unit
Maximum input voltage	30 Vrms
Capacitance	2100 ± 20% pF
Sensitivity (0dB=1V/BAR)	-65 dB
Bandpass Frequency	40 kHz ± 1 kHz
Operation Temperature	-20 → +70 °C

***Table 2**: Ultrasonic Transducer Specifications*

The sensor incorporates the following main blocks: the sensor tube with two 40 kHz transducers, a Programmable System-on-Chip (PSoC) CY8C58LP from Cypress Semiconductor Corp., a breadboard, and a few discrete components. The PSoC contains 32-bit Arm Cortex-M processor. To better perceive the node-to-node operation, Figure 13 presents the electrical circuitry details, including PSoC parts while Figure 14 illustrates an intuitive timing diagram of the intermediate waveforms at each node. The first two 16-bit pulse width modulators (PWM) (Figure 13(a)) in PSoC are driven by an 80 MHz clock and stabilized using PLL from an external crystal of 18MHz. The 40 kHz and FPulse signals are generated from the PWMs according to:

$$F\_Pulse = F\_Gate \wedge (F\_pulse \wedge F\_pulse) \quad (20)$$

where,

$$F\left[40kHz\right] = \left(F\left[pulse\right] \wedge F\left[pulse\right]\right) \quad 21$$

While using one 40kHz square would also work, implementing two PWM signals and taking their product results in finer control over the input phase of the signal, which was optimal for testing linearity between the input and output phase changes. With simple logic, $T\left[RX-1N\right]$, $T\left[RX-1P\right]$, $T\left[RX-2N\right]$, and $T\left[RX-2P\right]$ are generated as depicted in Figure 13(a & b) to drive the off-chip MOSFETs $M\left[1\right]$-to-$M\left[6\right]$ shown in Figure 13(c). The output of the drivers, i.e., $T\left[RX-1\right]$ and $T\left[RX-2\right]$ signals, are then converted to acoustic beams through the two transducers. The ultrasonic waves produced by piezoelectric transducers can be modeled as [61]:

$$u\left(t\right) = A\left(t\right)^{n} e^{-\alpha t} \sin\left(\omega t + \varphi\right) \quad 22$$

where n, α, ω, and φ are transducer dependent parameters: A is the wave amplitude, ω is the angular resonance frequency of the piezoelectric transducer (in this experiment $2\pi * 40 * 10^{3}$), and t is time. The parameters n and α are the empirical constants that are determined by experiments. Since this work is not intended for modeling, their exact value of these parameters would not be necessary.

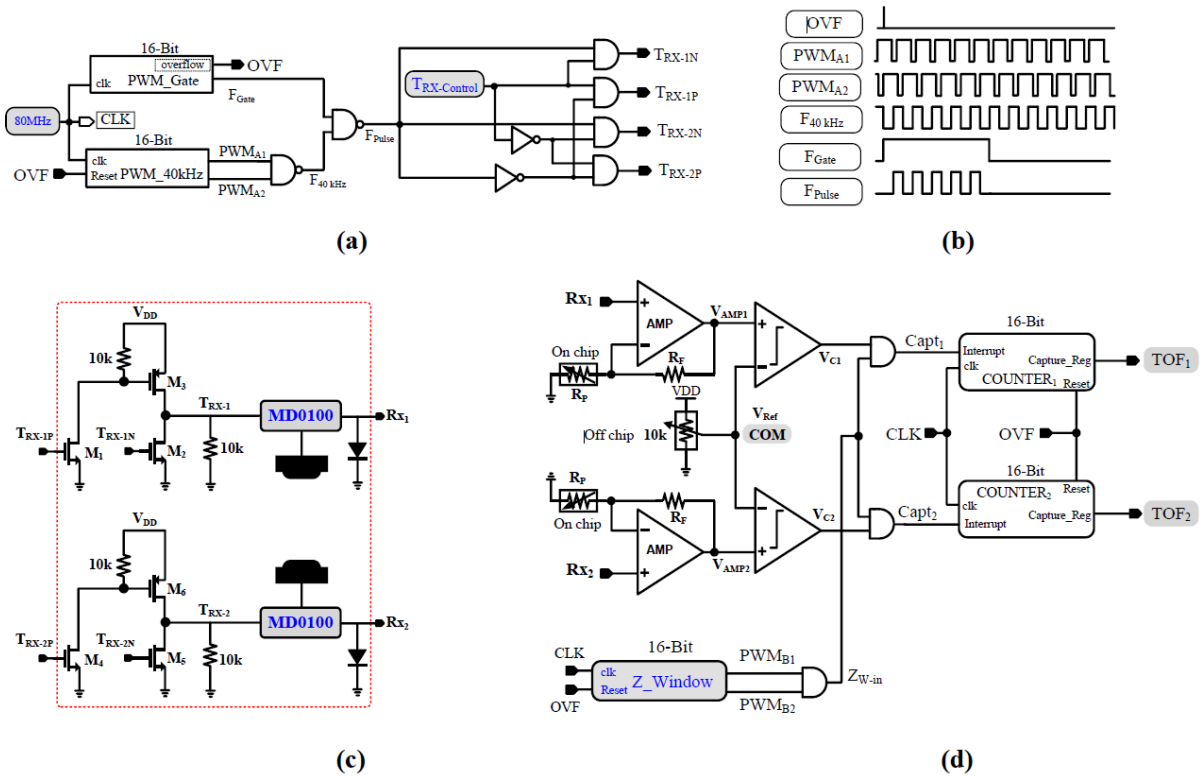

***Figure 13**: Circuitry details of the architecture: all circuits are implemented in PSoC platform except the once highlighted in red rectangle (a) Generate driving pulses (b) Intermediate waveforms used construct the transducer driving signals (c) Off chip MOSFET drivers (d) On chip acoustic-electric interface and TOF capture.*

This imposes no constraint on the practical implementation. The MD0100 switches are used as protection to prevent any high voltage to the Rx input amplifiers during the Tx mode. On the other side of the sensor operation, the echo acoustic beam is translated to electrical waveforms ($Rx□1□$ and $Rx□2□$) through the transducer as shown in Figure 13(d) and Figure 14. The electrical versions of acoustic beams are weak and have low amplitudes. Programmable gain amplifiers (PGA) are used to amplify $Rx□1□$ and $Rx□2□$ signals according to (23),

$$A = 1 + \frac{R□F□□}{R□P□□} \qquad 23$$

The PGA is configured to operate in noninverting mode. The gain is adjusted by changing the values of RF (feedback) and RP (potentiometer) as illustrated in Figure 13(d). The RF ranges

between 20 k to 980 k and the $R⍰P⍰$ ranges between 20 k to 40 k. To achieve a gain of 34 dB, the ratio of resistors is set as $R⍰F⍰ \approx 49\ R⍰P⍰$.

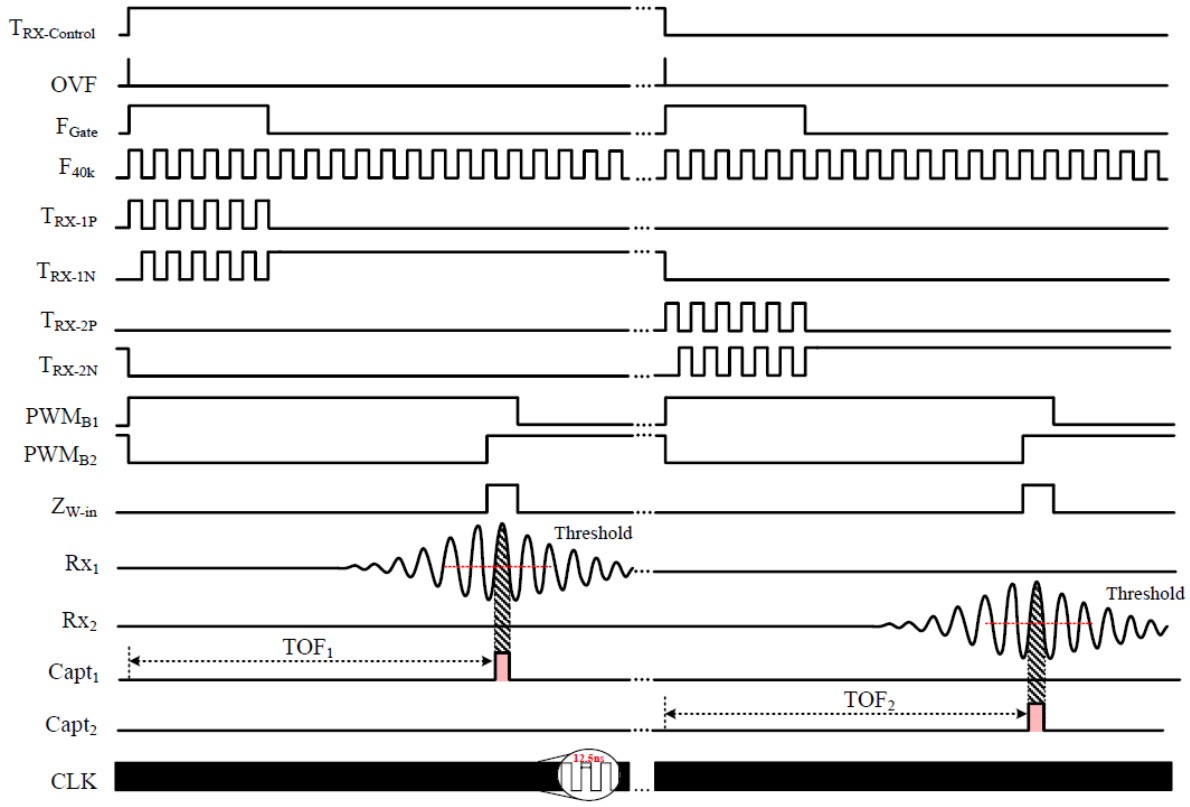

***Figure 14**: Timing diagram intermediate waveforms of architecture presented in Fig. 8.*

The bandwidth for this gain case is 215 kHz which is sufficient for this application. Following the PGA, a hard decision zero crossing detector is implemented. The optimal reference of the comparator ($V⍰Ref⍰$) is set through off-chip 10 k controllable potentiometer. The sampling window $Z⍰W - in⍰$ is adjusted to comply with the following condition in (24):

$$Z⍰W - in⍰ \leq 1⍰2⍰T \qquad 24$$

where T is the LSB of the TDC. By doing so, only one zero crossing is considered to generate the capture pulse. This prevents ambiguity in measurement, provided the maximum flow amplitude does not result in a phase change in excess of half the period of the ultrasonic wave. The iteration of each transmit/receive sample is indicated by a flow chart shown in Figure 15.

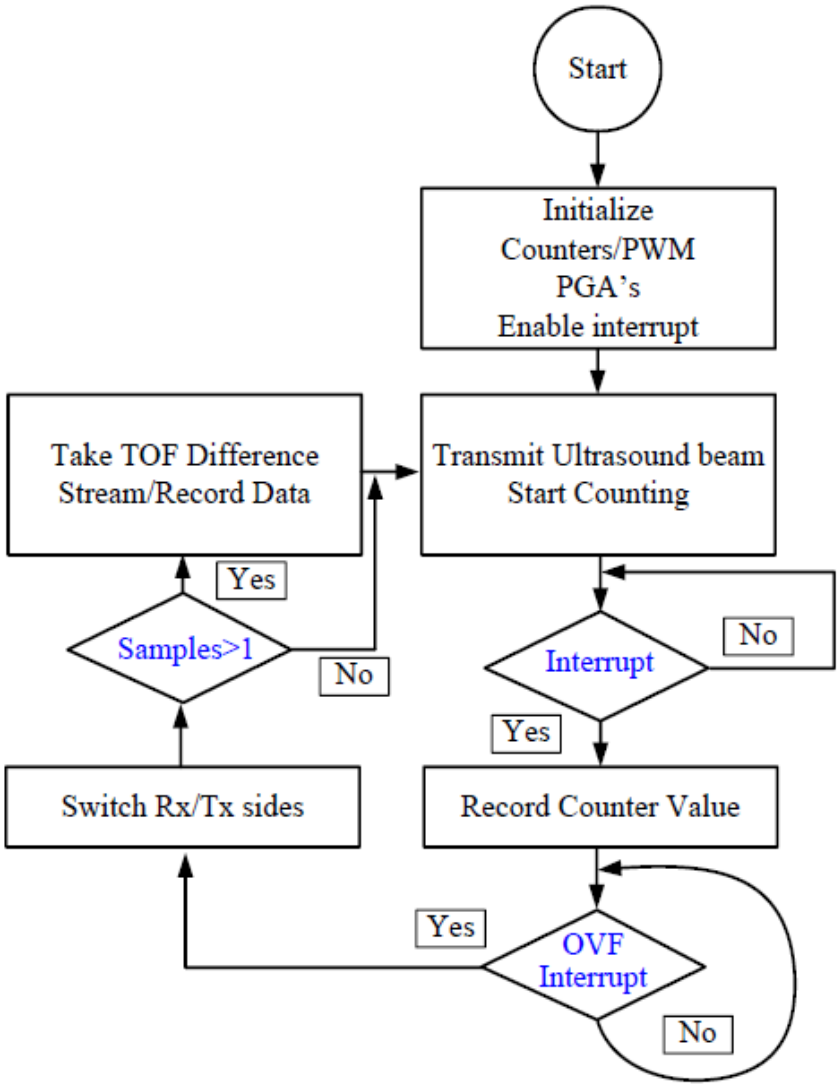

***Figure 15**:. Flow chart of flow tracking in one cycle*

On the other side, Envelope detection and thresholding makes measuring phase incredibly inaccurate, as this method depends heavily on consistent wave amplitude which varies greatly in time, and between transducers. Differences between transducers, bandwidth, damping coefficients and efficiency all affect the received wave amplitude, however the largest contributor to amplitude variation occurs while flowrates vary in time. The movement of the fluid carrying the wave alters the delivered wave energy and thus, received amplitude. To circumvent these issues, the envelope detector is removed, and the threshold is brought to the center of the waveform, where only the zero crossings are considered. Provided the wave amplitude between zero-crossings can exceed

the hysteresis upper boundary on the thresholding comparator (the tube is not obstructed, and wave energy is sufficient), any change in wave amplitude will not affect the transit-time measurement, vastly improving accuracy over the non-zero-crossing threshold method.

V. Experimental Measurements

A series of test benches were conducted to characterize the performance of the ultrasonic flow sensor prototype, both alone using an ASL5000 Servo Lung Simulator and under real-world use conditions with human beings.

A. Experimental Testbenches

The experimental test setup is shown in Figure 16. The HME (Heat and Moisture Exchanger) was utilized to decouple humidity from the bare transducers. The sensor works between ±5 Volts range. The PC is used to store data for postprocessing. The first testbench is to characterize the input/output transfer curve as shown in Figure 17. The pressure is swept from 4 to 20 cmH2O using a commercial AirSense™10 (ResMed Corp, California, USA) CPAP machine. The sensor shows very good linearity compared to the reference pneumotach. Many experiments have been carried out and the device shows good stability under different conditions. Figure 18 shows three cases of real time signals including a case of adult respiratory distress syndrome (ARDS). The extracted signals are generated by the ASL5000 lung emulator machine and referenced to pneumotach. The reliability and repeatability of the prototype is examined under five input scenarios and the sensor's filtered output (moving average filter) illustrated in Figure 19. The objective in Figure 19 is to examine the sensor functionality under several input signaling. The step response of the sensor is shown in Figure 19(a). The time response is in very agreement with the commercially available pneumotach. Figure 19(c&d) demonstrates how the tidal breathing and random AC signals can be tracked successfully by the ultrasonic sensor.

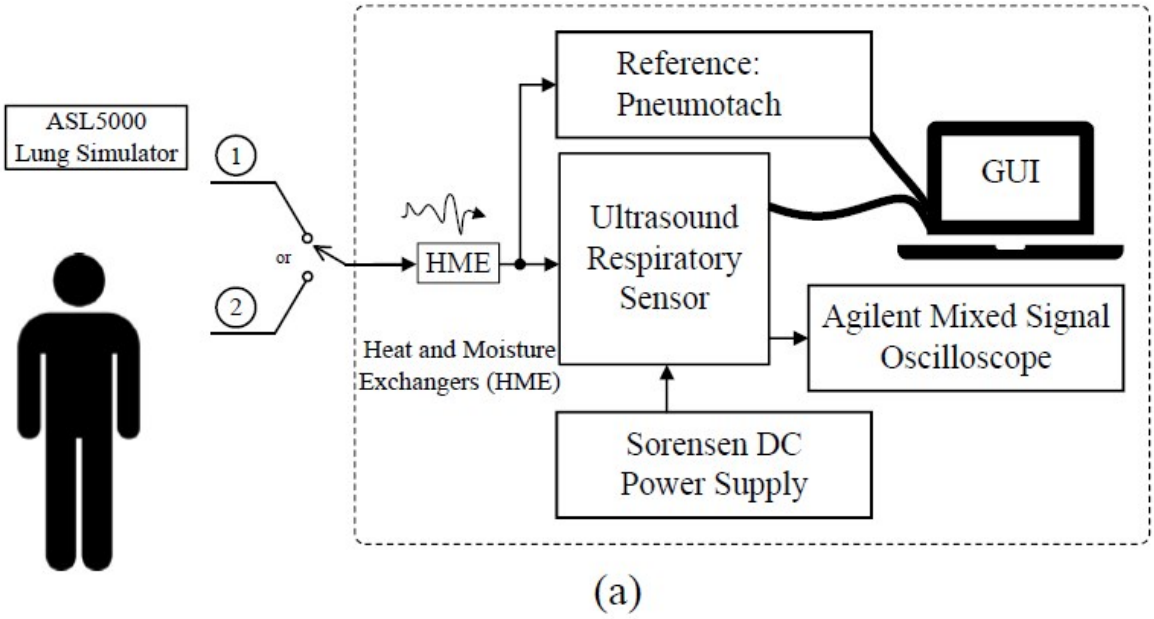

(a)

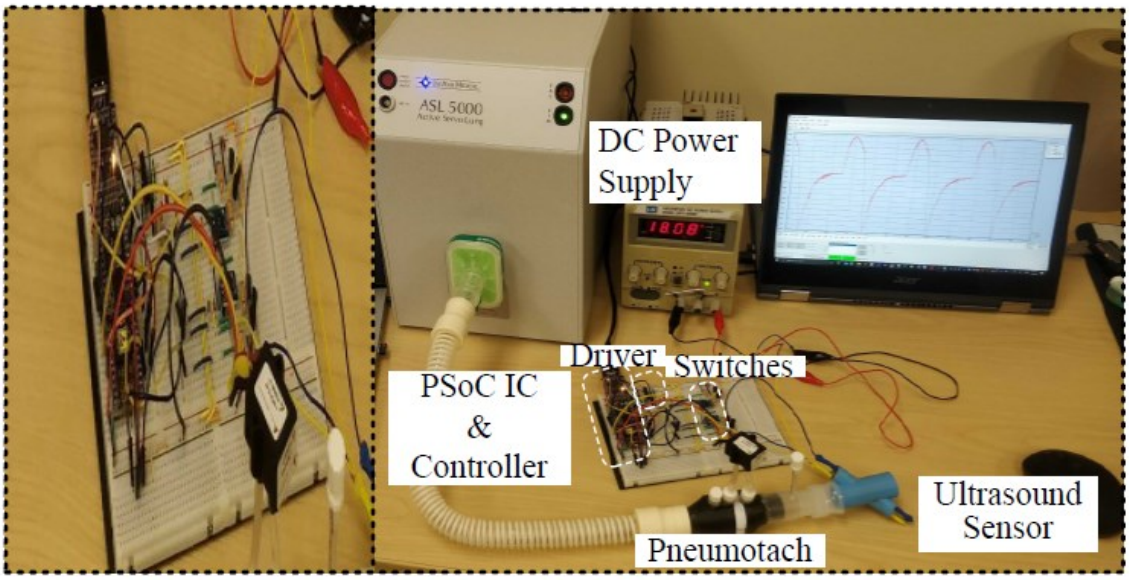

(b)

Figure 16:. *Test setup diagram (b) Hardware main components.*

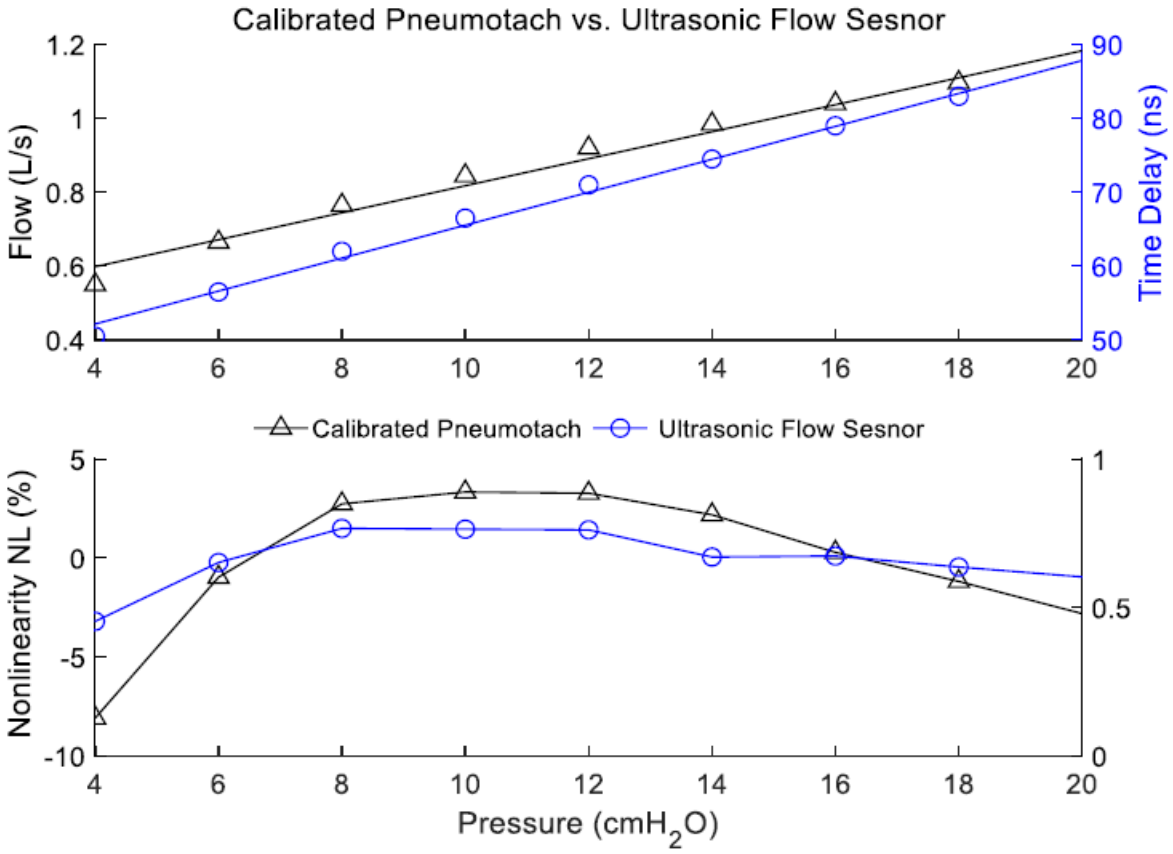

***Figure 17**:. Experimental DC steps linearity test*

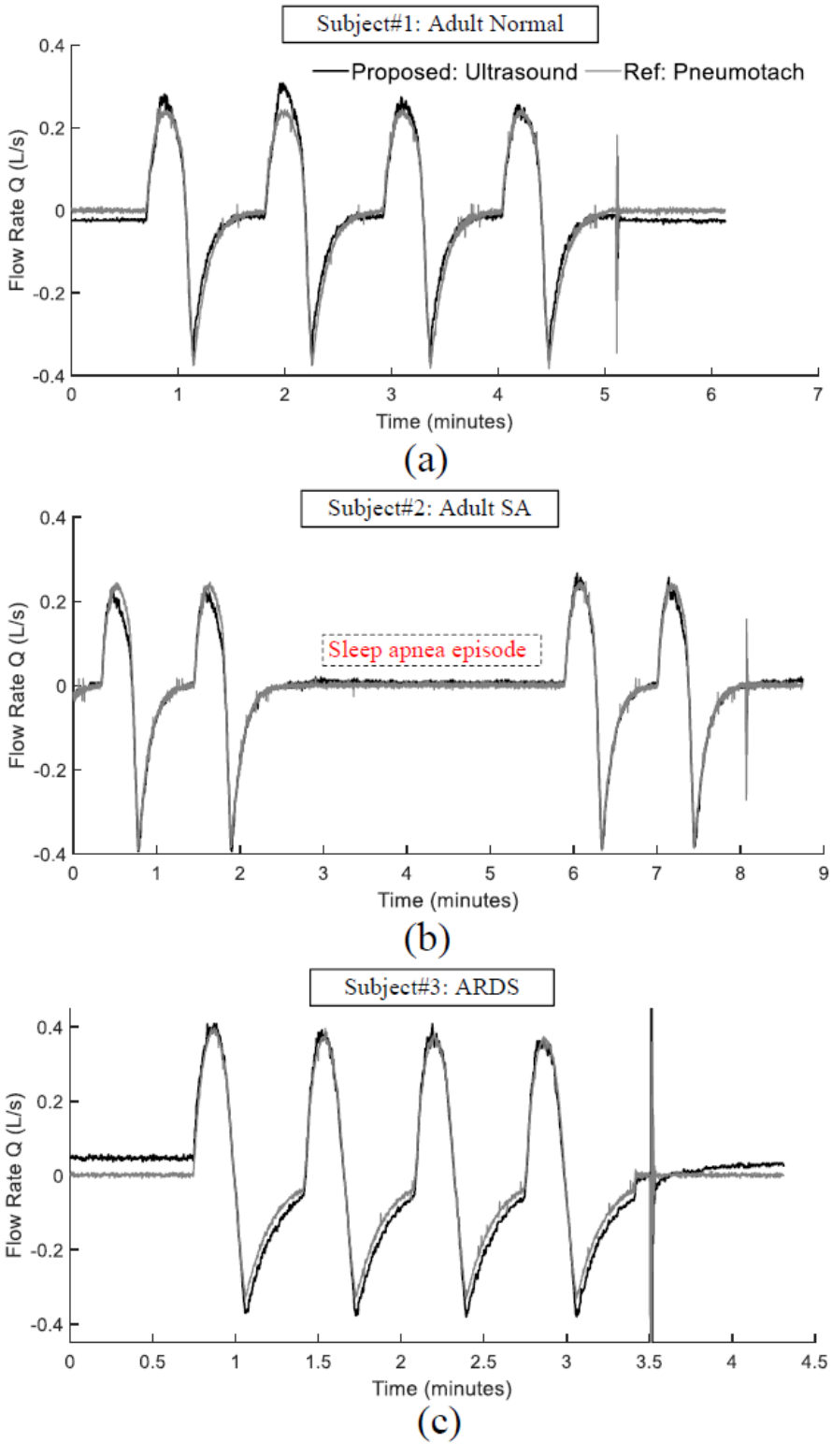

***Figure 18**: Experimental results of respiratory signs extracted with the ultrasound and ASL5000 servo lung simulator (a) Adult: normal (b) Adult: sleep apnea (c) Adult: ARDS.*

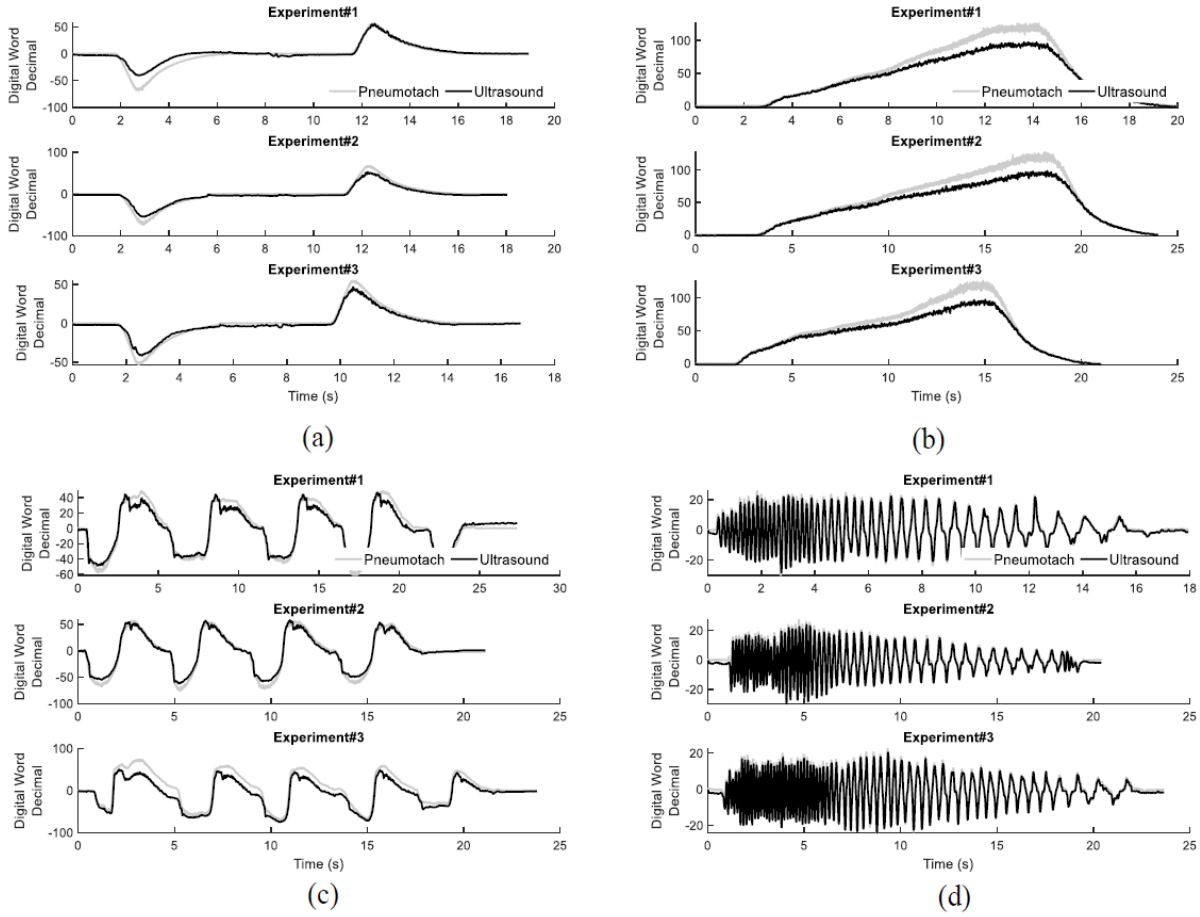

Figure 19*: Measurements of the repeatability of the prototype (a) Flow step (b) Ramp flow (c) Breathing flow: random (d) AC test.*

B. Resolution

The resolution of the proposed sensor can be estimated as follows: By inspection in (15)-(18), ΔTOF can be written as (16):

$$\Delta TOF \cong 2\,v\,p\,L\,2\,v\,sound\,2 \qquad 25$$

When there is no flow in the tube, then $TOF\,1 = TOF\,2 = TOF\,0$. Hence,

$$TOF(0) \cong \frac{L(2)}{v(sound)} \quad (26)$$

The ratio ΔTOF to the travelling time $TOF(0)$ measured at no flow condition is given by:

$$\Delta TOF(TOF(0)) = \frac{2\,v(p)}{v(sound)} = \frac{2Q(A)}{*\,v(sound)} \quad (27)$$

Expression (27) is used to estimate the needed measurement resolution. For instance, the minimum flow rate calculated for a given respiratory flow velocity of 0.1 m/s, and tube radius of 10 mm is about $Q(min) = 0.03 L/s$. Therefore, according to equation (25), this minimum flow rate of 0.03 L/s produces a ΔTOF value of about ΔTOF = 102 ns, provided that the zero-flow travelling time $TOF(0)$ = 87.5 μs (for $L(2)$ = 30 mm using (26)). Therefore, to achieve an accuracy of 95%, the proposed ultrasonic flow sensor must be able to accurately measure a minimum ΔTOF value of at least 5.1 ns which is comfortably met in this sensor. The sensor is demonstrated to be sensitive enough to detect respiratory scale flow rates, and the relationship between flow rate and sensed time of flight is relatively linear. By integrating the sensor with its sensing circuitry into a single package, the cost of the sensor could be greatly reduced. Table 3 summarizes the performance comparison with the state-of-art. Recently, an interesting review paper [62] shows the utility of optical fiber sensors in fluid flow measurement for industrial-based applications. It gives a good insight and comparison for the some of the references cited therein. Such techniques can be leveraged in future for different applications.

C. Nonlinearity Off-Line Compensation

To mitigate the possible nonlinearity in flow rate, compensation with the Least Mean Square (LMS) algorithm is used, this calculates the coefficients of the power series as depicted in Figure 20. Although, in theory, the ultrasonic transit time (i.e., TOF) is linearly proportional to the flow rate or the velocity of the tidal breathing, there is a nonlinearity that comes from the components in PSoC, signal conditioning circuitry, and interfaces between electrical and acoustic medium. Unlike the commercially available pneumotach devices, the proposed sensor nonlinearities can be compensated for only once. In this paper, a one-time calibration has been used using LMS and a calibrated pneumotach as a reference for a fair comparison. compact solution. The aim is to offer a portable and affordable power-efficient take-home device to track/predict sleep apnea with accuracy that meets global health authorities' standards.

***Table 3**: Performance comparison*

TABLE 3
PERFORMANCE COMPARISON

Architecture	Parameter						
	Approach	Digitized Variable	NL[1] (%)	Resolution (L/s)	PIF[2] (L/s)	PEF[3] (L/s)	Δ Temp Effect
This Work	Ultrasonic Acoustic	Time	< 5	0.03	0.3±0.03	1.9	Calibrated
[1]	Peunmotach	Voltage	NR[5]	0.1[6]	NR	NR	Uncalibrated
[3]	MEMS Capacitive	N/A	NR	NR	NR	NR	NR
[4]	MEMS Resistive	N/A	NR	NR	NR	NR	Calibrated
[5]	MEMS Resistive	N/A	NR	NR	NR	NR	Calibrated
[6]	MEMS Capacitive	Time	1	NR	NR	NR	NR
[7]	Piezoresistive	N/A	NR	NR	~ 0.002	0.1	Calibrated
[8]	RADAR	N/A	1.1	NR	NR	NR	Uncalibrated
[9]	Ultrasonic Acoustic	Voltage	> 11.7*	0.19	1.27±0.23	1.62±0.32	Uncalibrated
[10] **	Ultrasonic Acoustic	Voltage	9	NR	NR	NR	Uncalibrated
[29]	Ultrasonic Acoustic	Voltage	~ 3	NR	-1.6	2	Calibrated
[32]	Ultrasonic Acoustic	Voltage	20	0.05	NR	1.4	Calibrated

[1]NL (%): Nonlinearity
[2]PIF (L/s): Peak Inspiratory Flow
[3]PEF (L/s): Peak Expiratory Flow Rate
[4]FFT: Fast Fourier Transform
[5]NR: Not Reported.
[6]Typical for FOT approach but not reported in this article.
* Average
** Doppler: frequency shift and using non-contact chest methodology instead of air-coupling flow.

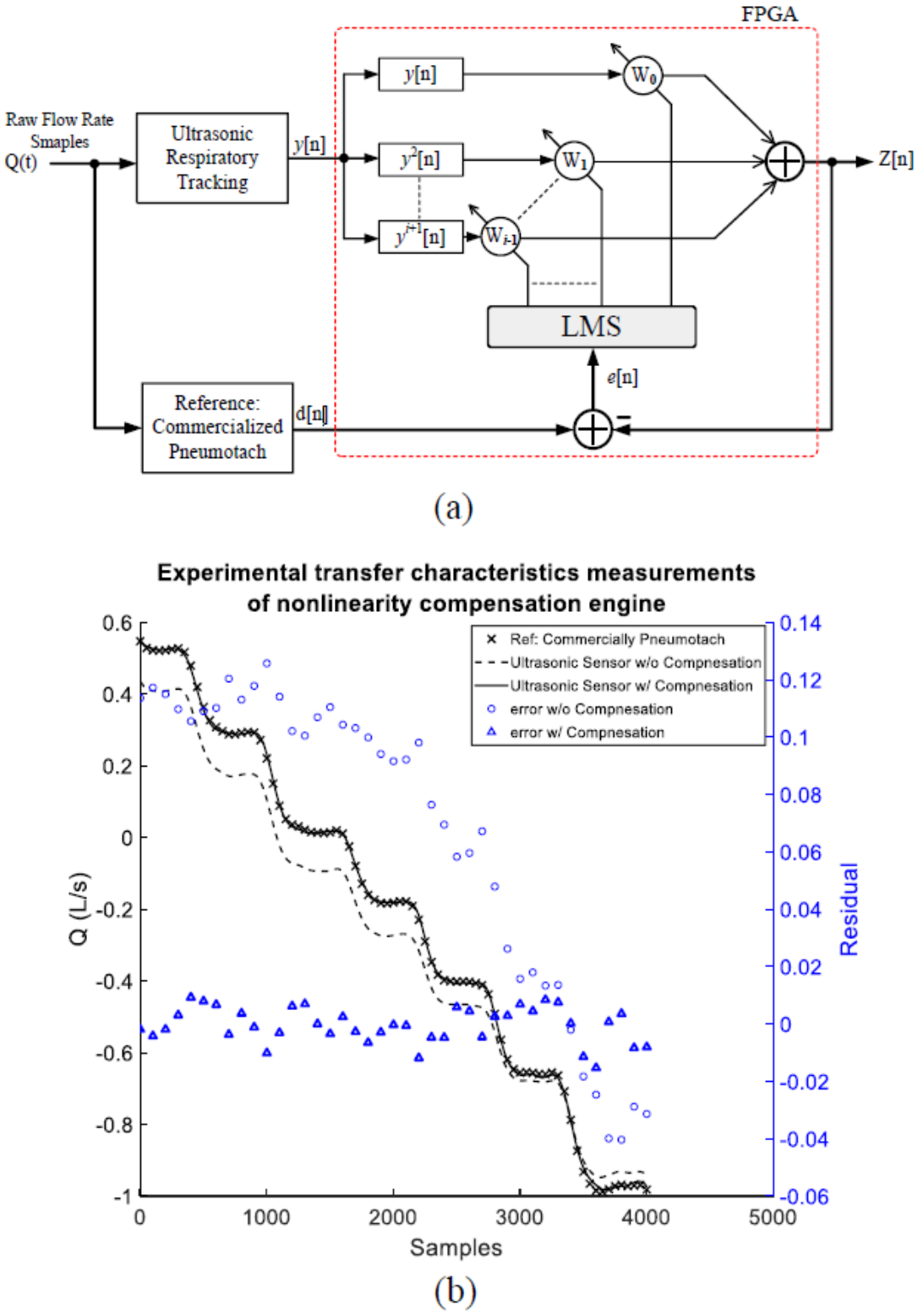

***Figure 20**: Block diagram of off-line nonlinearity compensation (b) Experimental measurements transfer characteristics of nonlinearity compensation engine.*

To calculate the inverse compensation coefficients, a commercialized pneumotach is used as a reference. After eliminating the error between the calibrated ultrasound sensor and the reference pneumotach, through the LMS algorithm, the non-linear distortion of the calibrated ultrasonic sensor can be cancelled. Assuming the output flow rate of ultrasound is:

$$y\,n\boxed{\ } = f\ Q\ t\boxed{\ }\boxed{\ } = \ i = 0\boxed{\ }N\boxed{\ }\ \alpha\boxed{\ }i\boxed{\ }\ Q\boxed{\ }i\boxed{\ }(n)\boxed{\ } \qquad 28$$

where α (i>0) are the non-linear distortion coefficients. After power series compensation, the output is:

$$Z\,n\boxed{\ } = \ i\boxed{\ }\boxed{\ }\ W\boxed{\ }i\boxed{\ }\ y\boxed{\ }i\boxed{\ }(n)\boxed{\ } \qquad 29$$

where $W\boxed{\ }i\boxed{\ }$ are the inverse coefficients. For instant, the coefficients required to eliminate the second and third order distortion are shown in (30).

$$W\boxed{\ }1\boxed{\ } = \ 1\boxed{\ }\ \alpha\boxed{\ }1\boxed{\ }\boxed{\ }, \ W\boxed{\ }2\boxed{\ } = \\ -\ \alpha\boxed{\ }2\boxed{\ }\boxed{\ }\ \alpha\boxed{\ }1\boxed{\ }3\boxed{\ }\boxed{\ }, \ W\boxed{\ }3\boxed{\ } = \ 2\ \alpha\boxed{\ }1\boxed{\ }3\boxed{\ } -\ \alpha\boxed{\ }1\boxed{\ }\ \alpha\boxed{\ }3\boxed{\ }\boxed{\ }\ \alpha\boxed{\ }1\boxed{\ }5\boxed{\ }\boxed{\ } \qquad 30$$

In this setup i=9. As a gradient-descent algorithm, the procedure of calculating coefficients for power series can be described as follows:

$$\boldsymbol{Y}\boxed{\ }\mathbf{1}\boxed{\ } = \quad y\,n\boxed{\ }\boxed{\ }\ y\boxed{\ }1\boxed{\ }\ n\boxed{\ }\boxed{\ }\ y\boxed{\ }2\boxed{\ }\ n\boxed{\ }\boxed{\ }\ \vdots\ \boxed{\ }\ y\boxed{\ }i\boxed{\ }\ n\boxed{\ }\boxed{\ }\boxed{\ }\boxed{\ }\boxed{\ }T\boxed{\ } \qquad 31$$

$$\boldsymbol{W} = \quad w\boxed{\ }1\boxed{\ }(n)\boxed{\ }\ w\boxed{\ }2\boxed{\ }(n)\boxed{\ }\ w\boxed{\ }3\boxed{\ }(n)\boxed{\ }\ w\boxed{\ }4\boxed{\ }(n)\boxed{\ }\ \ldots\ \boxed{\ }\ w\boxed{\ }i\boxed{\ }(n)\boxed{\ }\boxed{\ }\boxed{\ }\boxed{\ }T\boxed{\ } \qquad 32$$

$$Z\,n\boxed{\ } = \ \boldsymbol{Y}\boxed{\ }\mathbf{1}\boxed{\ }\boldsymbol{T}\boxed{\ }\boldsymbol{W} = \ i\boxed{\ }\boxed{\ }\ w\boxed{\ }i\boxed{\ }\ y\boxed{\ }i\boxed{\ }(n)\boxed{\ } \qquad 33$$

$$e\,n\boxed{\ } = d\,n\boxed{\ } - z\,n\boxed{\ } = d\,n\boxed{\ } -\ \boldsymbol{Y}\boxed{\ }\mathbf{1}\boxed{\ }\boldsymbol{T}\boxed{\ }\boldsymbol{W} \qquad 34$$

where $\boldsymbol{Y1}$ is the input matrix, $\boldsymbol{W}$ is the coefficients matrix and *z(n)*, *e(n)* and *d(n)* are the output, error and reference signals respectively (Figure 20). The LMS algorithm runs until $E[\,e^2(n)]$ reaches its smallest value. According to gradient-descent method, the coefficient (weight) updating function is obtained as:

$$W(i)(n+1) = W(i)(n) + \mu * e(n) * y(i) \qquad 35$$

where μ is the updating step size.

D. FOT Testbed

To test the sensor's capability under Forced Oscillation Technique (FOT) scenario, the experiment setup is developed as illustrated in Figure 21(a). The speaker is hence driven by an amplifier under different swing levels. The maximum driving voltage in this setup is 1000 mV where the sensor can easily pick up the acoustic beams generated after the speaker. As the FOT voltage goes down 200 mV, the sensor ability to track the FOT waveform becomes more and more challenging and it needs sophisticated signal processing. The presented curves are postprocessed using moving-average filter.

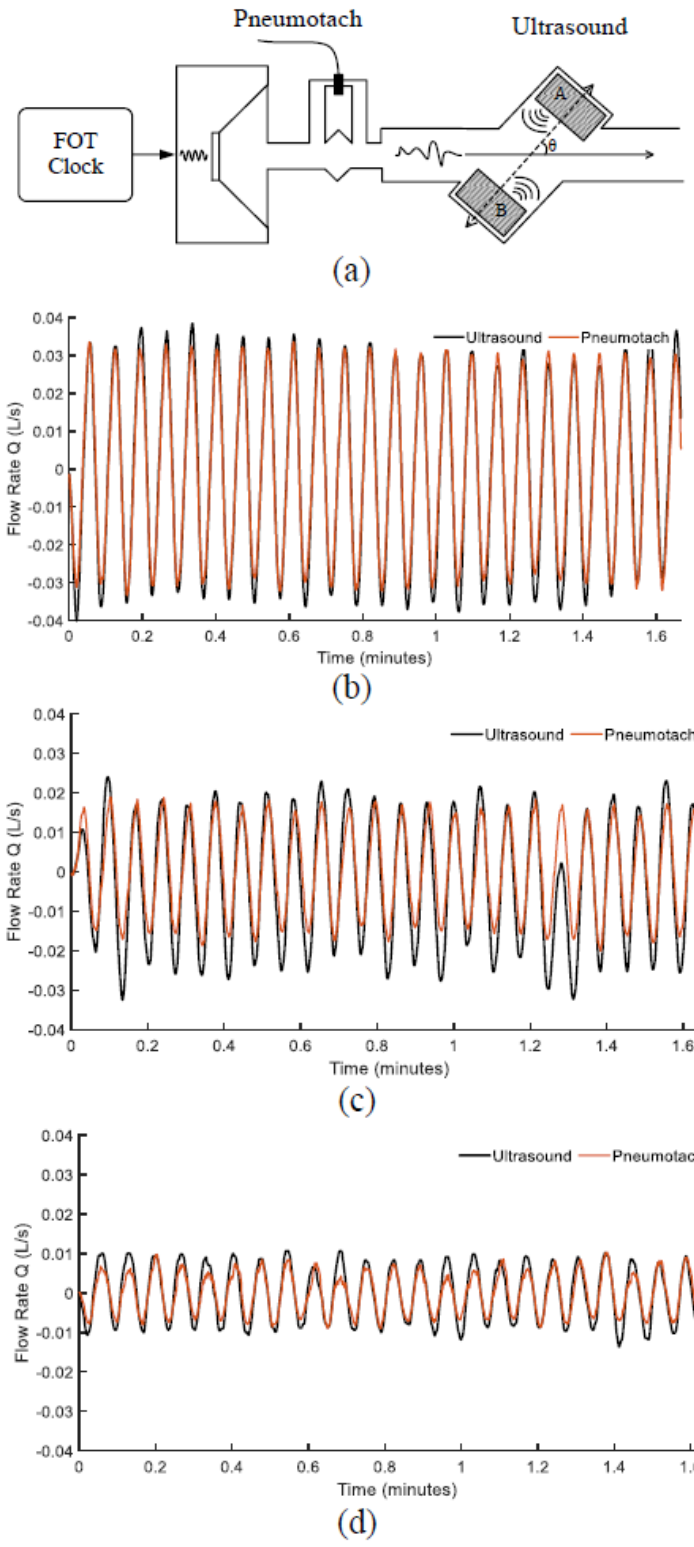

***Figure 21**: FOT measurement (a) Experiment setup when the speaker driving voltage is (b) 1000 mV (c) 500 mV (d) 250 mV.*

VI. Conclusion

In this paper, a respiratory flow sensor with resolution down to 0.03 L/s is presented. The sensor was designed based on the principle of ultrasonic echo transit time, in which time is directly digitized, augmented by a multibit time to digital converter, which distinguishes it from pre-existing approaches. The proposed design is compact architecture and is suitable for standard health applications.

Acknowledgment

Acknowledgment is due to the Natural Science and Engineering Research Council of Canada (NSERC) and NovaResp Technologies Inc., Halifax, NS, Canada, for supporting this research. Acknowledgment is also due to Dalhousie University for providing the facilities.

Chapter 4 : LUNG MECHANICS TRACKING WITH FORCED OSCILLATION TECHNIQUE (FOT) BASED ON CMOS SYNCHRONOUS DEMODULATION PRINCIPLE

Authors:

Gregory Begin,

Karama M. AL-Tamimi,

Hamed Hanafi Alamdari,

Tobias Witter,

Kamal El-Sankary

Published, Transactions on Biomedical Circuits and Systems © 2022 IEEE. [63]

This manuscript has been modified from its original format to conform to the structure of this dissertation

Abstract

In this paper, an area-efficient CMOS integrated solution for lung impedance extraction is presented. The lock-in principle is leveraged for its high effective bandpass selectivity, to acquire information about the airways, through stimulation by FOT (Forced Oscillation Technique). The modulated pressure and flow signals are down-converted by a quadrature voltage commutating passive mixer-first receiver. In addition to its linearity, and unlike the Gilbert cell, it can be biased at zero *dc* current to alleviate flicker noise contributions. The proposed solution is designed and fabricated in 0.18μm TSMC technology. The chip occupies an active silicon area of 4.7 mm2 (including buffers and pads) and dissipates 429.63 μW. The proposed approach offers real time tracking of respiratory mechanics and is expected to be a promising solution for portable health monitoring and cost-effective biomedical devices.

I. Introduction

Diagnosis, treatment, and monitoring of respiratory disorders is critical for the long-term wellbeing of those suffering. Among such disorders include sleep apnea, COPD, asthma, and most recently, disorders related to the onset of COVID-19 [64]. Measuring respiratory impedance is a key tool in diagnosing and monitoring such respiratory disorders [65]–[67]. Respiratory impedance is a mechanical quantity, defined as the ratio of pressure and flow, as opposed to electrical impedance, composed of voltage and current respectively. Methods for measuring respiratory impedance include some time series-based approaches; the identification method, and the recursive least squares algorithm [68]–[70]. While others use a frequency domain approach as illustrated in Figure 22. This frequency-based method used to track respiratory mechanics is known as FOT (Forced Oscillation Technique a.k.a. Oscillometry).

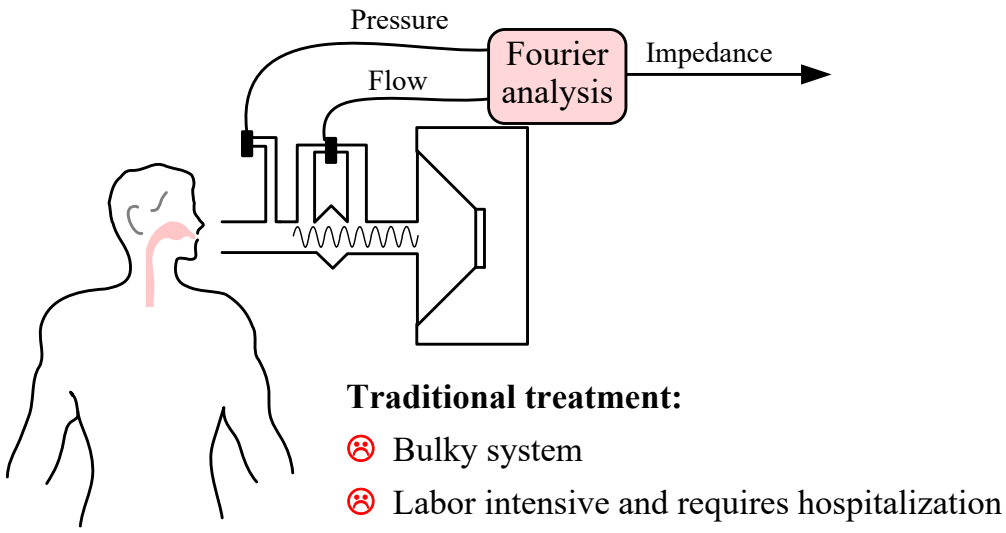

***Figure 22**:. Extraction of the patient's lung mechanics*

Introduced in 1956 by DuBois et al. [12], FOT utilizes a pressure signal (force) to evoke a flow (displacement) response of the respiratory system. Typically, this process is carried out by a speaker or modulated fan, at high amplitudes and low frequencies (<10Hz). This is followed by pressure and flow sensing, to capture the force (pressure), and displacement (flow) signals respectively. The calculated resistance (real part of respiratory impedance), and reactance (imaginary part of respiratory impedance), of the pressure and flow signals obtained via FOT, provide information about respiratory mechanics. Figure 23 shows the conceptual diagram of the respiratory system and the approach of extracting respiratory impedance (Z). Because of FOT's non-invasive nature, it can be continuously applied to spontaneously ventilating patients.

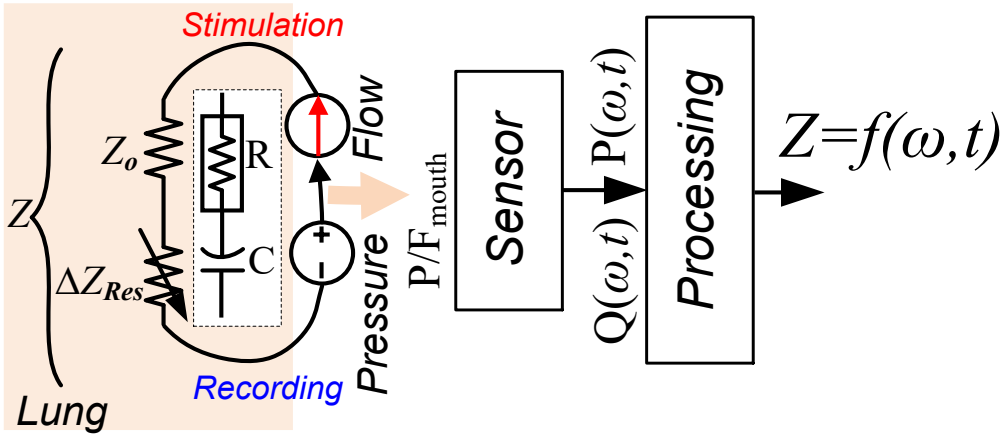

***Figure 23**: Motivation: Conceptual diagram of the respiratory system and the approach of extracting lung impedance, Z. The pressure emulates the voltage while flow is current.*

Industry efforts for long term monitoring of progressive and chronic respiratory disorders, highlight the desire for a miniaturized, continuous, non-invasive, and low power respiratory mechanics sensor. The crucial task, therefore, is to accurately extract FOT signal information, i.e. magnitude and phase [12], while maintaining an appropriate Signal to Noise Ratio (SNR) and consuming less power and computational resources. Recent study [14] supports the idea that high frequency oscillometry for continuous use is possible and can be useful for Positive Airway Pressure (PAP) devices and other mechanical ventilators. Therefore, to miniaturize this system, the FOT frequency is increased to shrink required speaker size, and its amplitude reduced for lower power, (i.e., longer battery life), and less noticeable operation during sleep. This poses a challenge in the face of a breathing noise floor, as SNR gets poorer when amplitudes are reduced. To this end, this article demonstrates a CMOS-based lung impedance extractor. The proposed design implements a lock-in amplifier (LIA) as an analog front-end to determine impedance from a known FOT signal, as it is buried under breathing noise. This paper is organized as follows. In Section II, a background overview is presented. Section III discusses the circuit implementation, details of the system architecture and the principle of operation, followed by the measurement results in Section IV. Finally, this paper is concluded in Section V.

II. Overview

A. Background Review

One of FOT's uses is to distinguish between obstructive and central apneas in patients suffering from sleep apnea [66]. To treat obstructive sleep apnea and minimize recurrence of symptoms, continuous positive airway pressure (CPAP) was developed [71]. Moreover, the usage of a higher frequency lower amplitude oscillometry on a simple noninvasive ventilator such as CPAP was shown in an experimental study [14]. Theoretically, the patient's airway impedance, $Z\ j\omega$, can be modelled as a time-varying complex quantity involving a real resistive component, R, and imaginary reactive component, X, as in (36).

$$Z\ \omega = R\ \omega + jX\ \omega \tag{36}$$

where the reactive component comprises the elastance and inertance of the lung. By probing the airway with a low frequency (infrasound) sinusoid and measuring perturbations in the phase and amplitude of pressure and flow waveforms, one can reveal changes in the complex airway impedance. The ratio of pressure $P\ \omega, t$ and flow $F\ \omega, t$ is equal to the impedance seen by the wave source.

$$Z\ \omega, t = \ P\ \omega, t\ F\ \omega, t \tag{37}$$

This time varying impedance has been shown to have diagnostic qualities when checking a patient's lungs and overall airway health in cases of asthma and chronic obstructive pulmonary disease (COPD). This kind of application also drives the need for different types of respiratory tracking sensors. As a results, silicon-based respiratory sensors [28], [32] and phase detection techniques [34], [35] have been reported. These approaches are promising for improving detection of sleep apnea, as semiconductor foundry technology is scaling down.

B. Impedance Calculation (Lung Mechanics)

The typical method for calculating impedance (Z) is done using the complex ratio of the Fast Fourier Transform (FFT) of sampled *P* and *F* data:

$$Z\ f(k) = FFT\ P(n) / FFT\ F(n) \quad (38)$$

where $f(k)$ is the corresponding frequency bin of the FFT operation. The real and imaginary parts of Z ($R\ f(k)$ and $X\ f(k)$) (39) and (40), respectively,

$$R\ f(k) = Re\ Z\ f(k); \quad 1 \le k \le N \quad (39)$$

$$X\ f(k) = -2\pi k(\delta t) Re\ Z\ f(k); \quad 1 \le k \le N \quad (40)$$

where δt is the sampling interval, and N is the number of points per interval. However, Z is not only a function of frequency but also a function of time. To represent the complex information over time, the Short Time Fourier Transform (STFT) is used. The STFT is effectively a sliding window FFT which, unlike the regular Fourier transform, contains phase as well as amplitude information. This works by using a high-speed, high-resolution ADC to capture time series data, which is then processed to yield $Z\ f(k)$. The sampling interval then changes in time, and impedance is found for the next overlapping time interval, yielding $Z\ f(k), t$.

C. Synchronous Lock-in Concept

Although LIAs are widely used as laboratory equipment, few application-specific integrated implementations can be found in the literature for portable biomedical applications [72], [73]. Lock-In Amplifiers [74]–[78] employ homodyne mixing, followed by low pass filtering to extract phase and magnitude information from a specific spectral component of a broad-banded, noisy

signal, even when the SNR of the information is considerably poor. This technique is used in many sensitive scientific experiments where extraction of data is not possible without it. The lock in technique can be described by the following principle:

$$V_{LIA}(f) = \int_0^T A_1 \sin(2\pi f t + \emptyset_1) \cdot A_2 \sin(2\pi f t + \emptyset_2) dt \qquad 41$$

$$V_{LIA}(f) = \begin{cases} DC: \frac{1}{2} A_1 A_2 \cos(\emptyset_1 - \emptyset_2) & f > 1/2T \end{cases} \qquad 42$$

The input signal is represented as purely sinusoidal for simplicity's sake. The LIA multiplies the input by a reference sinusoid (Eqn. 41), to shift half of the resulting signal power (in the frequency domain) to $(f - f)$ and the other half to $(f + f)$ by the sum difference principle shown in Eqn's 44, 45 & 46. If the chosen mixing frequency exactly matches the input frequency, the signal power is shifted to DC and $2f$. The integration from 0 to T (Eqn. 41) represents the low pass filtering function of the LIA, which averages the $2f$ component (and out of band noise) of the signal to zero. The resulting DC amplitude is determined by the amplitude of the two signals and the phase angle between them (Eqn 42). Because the signals may not be exactly in phase, due to signal path phase addition, and introduced phase addition from the measurement, $\emptyset_1$ is not expected to equal $\emptyset_2$. However, to get the full picture of the measured sinusoid, $\emptyset_2$ is chosen at two values, separated by $\pi/2$. This results in two DC values, first the in-phase (I) measurement and second, the quadrature-phase measurement (Q). These two values can be plotted in a complex Cartesian plane which results in the magnitude and relative phase angle of the measured signal. The power of the LIA lies in its ability to precisely single out the frequency of interest, (as the input and reference sinusoids are generated by the same source), and to have its effective filtering bandwidth quality factor, scale with averaging time. This kind of measuring system can be applied to forced oscillation technique (FOT) in the monitoring of mechanical systems such as airway impedance. When low frequencies <100Hz and infrasound are passed into a patient's airway along with regular breathing, at amplitudes low enough not to be detected by the patient, the pressure and flow signals generated will be buried under noise. By using the lock-in technique, one can ensure extraction of lung and airway impedance despite this noise. To intuitively compare the typical structure of

extracting a single tone from a noisy environment compared to the lock-in amplifier, let us consider this next case. Assume there is an FOT signal at 17 Hz. A good low-noise amplifier (LNA) will have about $0.5mV/\sqrt{Hz}$ of voltage noise spectral density, V_{PSD}. If this LNA has a bandwidth (BW) of 100 Hz and gain of 10^3, then the noise signal (V_n) in the pass band can be given as:

$$V_n = V_{PSD} \times \sqrt{BW} \times Gain \qquad 43$$

Where V_n is the root mean square of the noise. There will be not much luck measuring the output signal, V_s, unless we single out the frequency of interest which is at 17 Hz. If we follow the LNA with a band pass filter (BPF) with a quality factor, Q_F of 50, (in STFT case Q_F =21.5 ~ 22) centered at 17 Hz, Any signal within a bandwidth of 0.34 Hz ($17Hz/Q_F$) will be detected. The noise in the filter pass band according to (44) will limit the SNR to ~ 2.2 at 1mV of input signal. On the other side, the LIA can detect the signal at 17 Hz with a bandwidth as narrow as 0.1 Hz and lower. In this case, the noise in the detection bandwidth will be much less, and an accurate measurement of the signal is possible. The SNR with respect to the input signal level is shown in Figure 24. The LIA overcomes the typical LNA+BPF topology. The contribution of this paper is on this frontier.

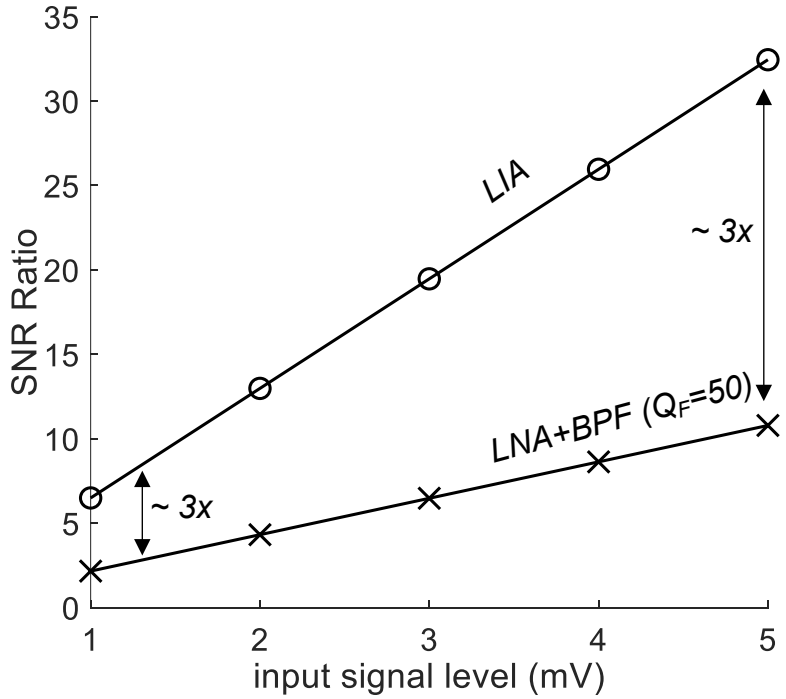

***Figure 24**: The efficiency of extorting weak signals from a noisy environment. SNR is in unitless ratio. Q_F is the quality factor of the bandpass filter.*

III. Architecture of the Proposed Application-Specific Solution

A. System Level

The top-level system architecture 1 is shown in Figure 25. Clock signals used for mixing are generated by the phase generator in Figure 29(a). The input clock signal is generated by a microcontroller (MCU) off chip. This clock signal is 4x the FOT frequency to allow the phase-generator the ability to create the non-overlapping phases (0, 90, 180, 270). The FOT signal is generated by the same MCU, using the same interrupt timer to ensure the signals are phase locked. The sqı re wa ; FOT (CLK/4) is then filtered to produce a sine wave. This FOT sine is then passed ıırough an amplifier and sent to the speaker which generates the mechanical signals. Pressure and Flow signals from the mechanical trasnducers enter the front-end at the mixers. After the mixers, the down converted Pressure and Flow signals are amplified by the chopper stabilized folded cascode amplifier and low pass filtered via the sub-Hertz filters before exiting the chip through buffers. All bandwidth and gain controls are handled by the MCU in software. The down converted and filtered outputs are collected by an ADC via PCB connections to a PSoC device and processed in MATLAB using equations (49 & 50) to obtain impedance. To understand the functionality of the system mathematically, let us recall the sum-difference identity:

$$sin⁡ 2\pi f⁡P⁡t⁡⁡ sin⁡ 2\pi f⁡FOT⁡t⁡⁡ = 1⁡2⁡ Y⁡dc⁡ - Y⁡2f⁡)⁡ \quad 44$$

$$Y⁡dc⁡ = cos⁡ 2\pi f⁡P⁡ - f⁡FOT⁡⁡t⁡⁡ \quad 45$$

$$Y⁡2f⁡ = cos⁡ 2\pi f⁡P⁡ + f⁡FOT⁡⁡t⁡⁡ \quad 46$$

where the $f⁡P⁡$ is the frequency of the incoming pressure signal and $f⁡FOT⁡$ is the frequency of the FOT reference signal, respectively (assuming that the amplitude is normalized to 1 in both signals). For clarity, $Y⁡dc⁡$ refers to the difference of frequencies and $Y⁡2f⁡$ refers to the sum of frequencies according to the trigonometric identity. If both frequencies being equal, with no phase difference,

$\Phi d = 0$, we get the *dc* component of the pressure signal in addition to the double frequency component. The amplitudes of which are half the product of the two sinusoid amplitudes according to (45). If there is a non-zero phase difference, $\Phi d = (\Phi P - \Phi FOT)$, between the two signals, it will be reflected as an amplitude degradation affecting the *dc* component by $\cos(\Phi d)$. Considering the four channels are theoretically identical in construction, let us analyze two quadrature-relative channels, e.g., the channel of real pressure P_{Re} and the channel of imaginary pressure P_{Img}. If the pressure transducer delivers the pressure and flow signals (in volts with a gradient sensitivity of K_P *(unit: V/(cmH2O))* and K_F *(unit: V/(L/s))*, respectively, the output of the low pass filter can be obtained by integrating the amplified mixed signal as follows, (under the condition $1T \gg 1$):

$$P Re = 1T \int_0^T A V V re(t) P\,t\,dt \quad 47$$

$$P Img = 1T \int_0^T A V V img(t) P\,t\,dt \quad 48$$

where $P Re$ and $P Img$ are the in-phase and quadrature voltages respectively, (I and Q). T is the period of FOT reference signal, $V re$ and $V img$ are the real part and the imaginary part of the reference signal, respectively, $P\,t$ is the pressure input signal (modulated by lung impedance Z) to be demodulated, and A_V is the gain of the amplifier.

By mapping the $P Re$ and $P Img$ from cartesian to polar, the phase and magnitude are obtained,

$$A P = \sqrt{P Re^2 + P Img^2} \quad 49$$

$$\theta P = \tan^{-1}\left(\frac{P Img}{P Re}\right) \quad 50$$

By extracting the pressure vector as $P V = A P\, e^{j\,\theta P}$ and in the same way, the flow vector $F V = A F\, e^{j\,\theta F}$, the time-dependent lung impedance can be represented as the ratio of both $P V$ $F V$,

$$Z = \frac{A P}{A F} e^{j\,(\theta P - \theta F)} \quad 51$$

Z gains its time dependance from the amplitude and phase angles of pressure and flow. In other words, by computing the relative angles and magnitudes of both $P\,t,\omega$ and $F\,t,\omega$, the lung impedance can be extracted in real time.

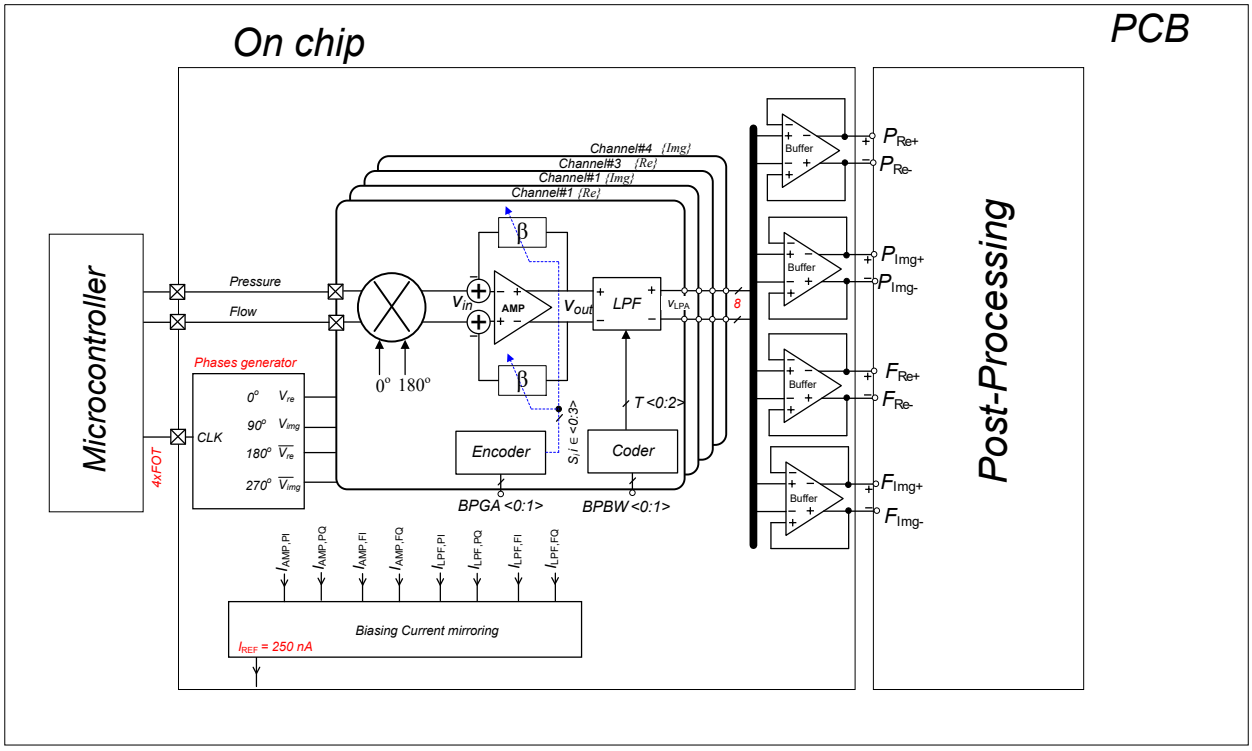

***Figure 25**: System level architecture.*

B. Model Verification

To examine the functionality of the proposed approach, the design has been developed and modeled (MATLAB-Simulink) as a demonstration. The model is tested under synthesized breathing signals and with a hybrid testbench, including actual data of several scenarios (different breathing cases, amplitudes, noise levels, speakers, CPAPs, and mesh resistors). The obtained output impedance is then compared to the typical FOT including the postprocessed FFT as a reference. The results demonstrate functionality with substantial area-efficiency and less fluctuations. Figure 26 shows the experiment to verify the approach against the STFT approach.

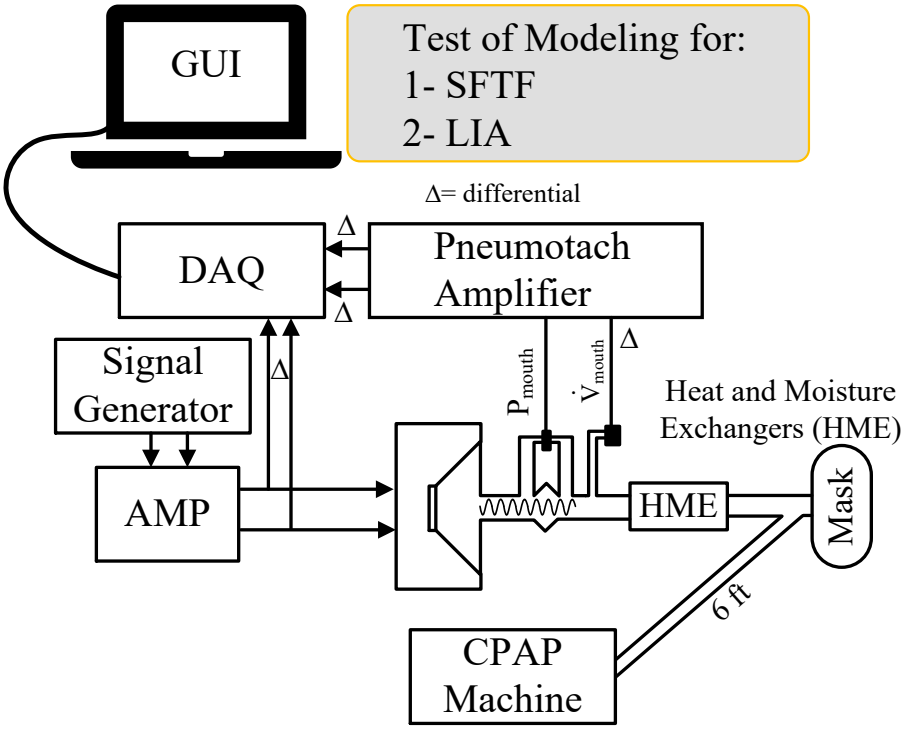

***Figure 26**: The modeling-experiment verification. An extensive hybrid testbenches has been carried out in the phase of the modeling and compared to the conventional SFTT methodology.*

C. Implementation Details

The top-level system is built in *n-well* 0.18µm CMOS process (1 poly and 6 metal layers). The pin-to-pin design is presented in Figure 27. The down-conversion operation is achieved using square wave pulse trains instead of pure sinusoids as depicted in Figure 29(b). The square waves which drive the mixer inputs, can be described by the Fourier series in the following equation:

$$V_{mix}(t) = \pi d + n = 1 \to \infty \; 2n \cdot sin(\pi nd) \cdot \cos(n\theta - 2\pi nt) \quad (52)$$

Where the mixer input $V[mix[t]$ is governed by its duty cycle d, (d < ¼ for four non-overlapping phases) and θ, where $\theta = 0,\ \pi[2[,\ \pi,\ 3\pi[2[$ for the phases (0, 90, 180, 270) respectively. Each mixer input takes two pulse trains. A "real" signal path takes $V[re[$ and $V[re[[$, which corresponds to 0 and 180 respectively, while an "imaginary" signal path takes $V[img[$ and $V[img[[$ or 90 & 270 degrees. Thus, the modulated *a.c.* pressure and flow signals are mixed by quadrature voltage commutating passive mixer-first receivers, using these complimentary pulse trains in four channels: real pressure ($P[re[$), imaginary pressure ($P[img[$), real flow ($F[re[$), and imaginary flow ($F[img[$). In addition to its linearity, and unlike the Gilbert cell, the passive mixer-first [76] can be biased at zero *dc* current to alleviate flicker noise contributions. Since the mixer input impedance is signal-dependent, a buffer is inserted between the mixer and the pressure transducer (at the PCB level) to provide isolation. The mixer is followed by a programmable gain amplifier (PGA) (22−47 dB), which is wrapped by a pair of chopping switches so that the contribution of *1/f* noise, and or dc offsets (mainly by the PGA folded-cascode amplifier) can be mitigated. The low pass filtering of each lock-in cell is performed by a capacitive multiplier structure to reduce area consumption while maintaining a sub-Hertz cutoff frequency. Another advantage of this implementation is the minimum use of circuitry due to square wave demodulation that can be achieved. The main disadvantage is that the square wave waveform causes the introduction of several harmonics in the reference signal. The effect of these harmonics, with frequencies other than the required, are in great part mitigated by the demodulation and averaging process. The parallel combination of C and $R[PGA[$ in Figure 27(a) sets the -3dB point.

$$A\,s[= -\ \ R[PGA[[\ R[in[[[1 + s\,R[PGA[C[\qquad 53$$

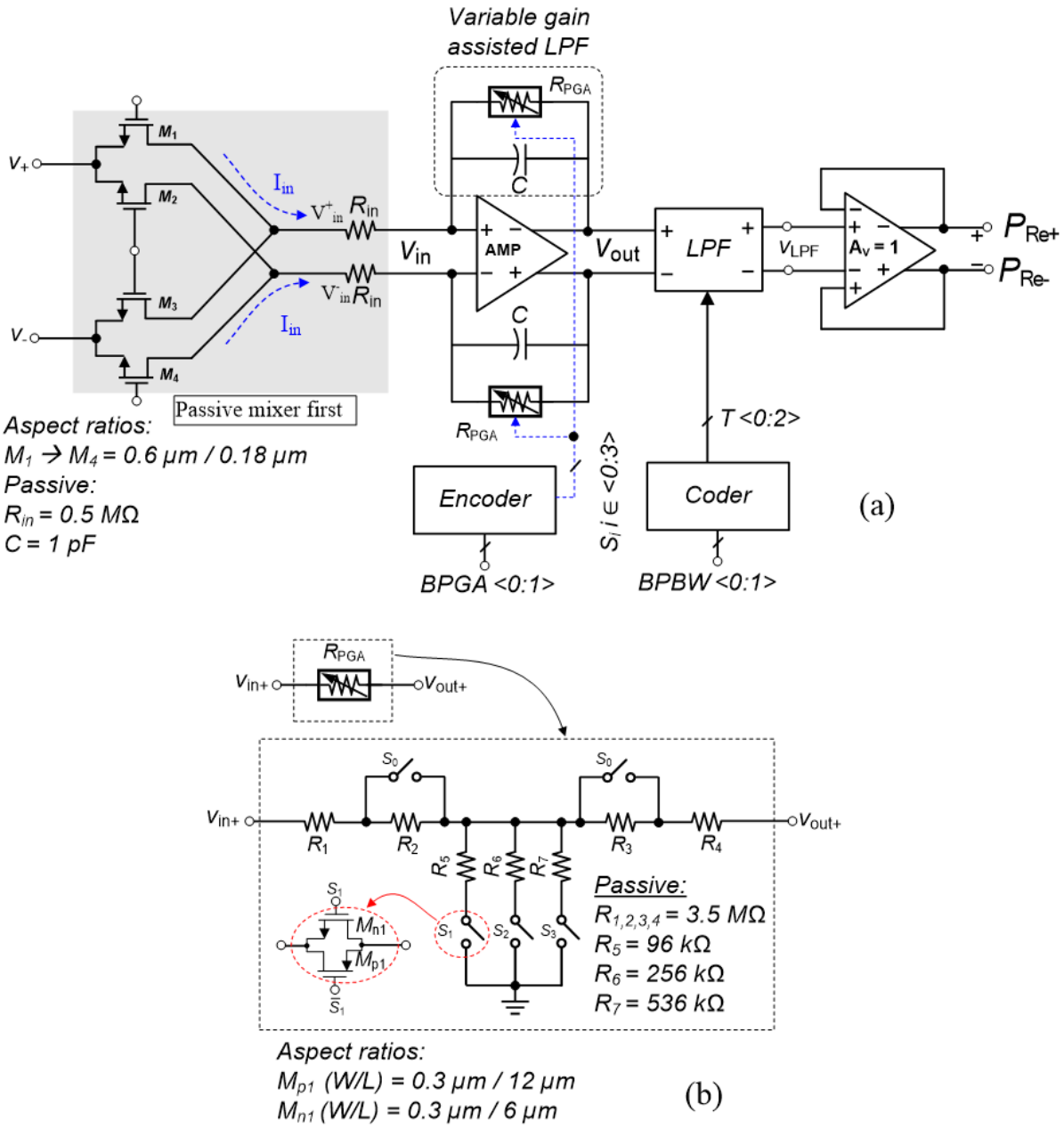

***Figure 27**: One channel contains (a) mixer-first receiver, chopped amplifier, and low pass filter. (b) Digitally programmable resistor implementing the R_{PGA} that enables A_V tuning of the first-order active-R filter after the chopping.*

At low frequencies, the impedance of the capacitor *C* is much higher than R_{PGA}, so the *dc* gain is mainly set by the standard inverting formula of R_{PGA}/R_{in}. As the frequency increases the

capacitor's impedance decreases reducing the impedance of the parallel combination of *Xc*|| $R\_PGA\_$, until eventually at a high enough frequency, *Xc* reduces to ~ zero. The advantage here is that the circuits input impedance is now just R_in_. With the components in the feedback circuit that determines the corner frequency, the R_PGA_C set-point is unaffected by variations in source impedance and the *dc* gain can be adjusted independently of the corner frequency especially for this low frequency application. Having a programmable gain for the amplifier offers an extra functionality, as some sensor outputs may be in the millivolt range, others can be pre-amplified (> 100 mV *ac*) and could saturate the amplifier. Adding an $R\_PGA\_$ network offers this kind of freedom. The programmable $R\_PGA\_$ network structure is shown in Figure 27(b). The Equations governing the forward and backward transfer characteristics of $R\_PGA\_$ are given, respectively, as $V\_out\_\ V\_in\_ = R\_1\_ + R\_2\_\_ + R\_3\_ + R\_4\_\_||\ R\_5,6,7\_\_$ and $V\_in\_\ V\_out\_ = R\_3\_ + R\_4\_\_ + R\_1\_ + R\_2\_\_||\ R\_5,6,7\_\_$. Because of the choice of resistance and S<0> being tied to both sides, the transfer characteristics are symmetrical, $R\_3\_ + R\_4\_\_ = R\_1\_ + R\_2\_\_$. The value of resistance for $R\_5,6,7\_$ can only take on 4 values, as the encoder block only keeps one switch active (or none) at once. Combined with S<0>, this results in 3-bit functionality, or $2\_3\_$ gain permutations. This structure replaces the resistor $R\_PGA\_$ in the feedback path of the amplifier. Changing its value would also alter the bandwidth behavior of the first low-pass filter stage. It is favorable to ensure that the smallest value of resistance from the network still offers a cutoff below the chopping frequency, this can be achieved by tuning the value of C to keep the R_PGA_C product below that of $1\_\ \omega\_CH\_\_$ for the smallest value of $R\_PGA\_$. This can be applied, as long as those resistors are connected to virtual ground, which simulates the proper operating condition of the programmable resistor network. As indicated in Figure 28, the structure of the differential folded-cascode implementation is chosen as a single-stage opamp that needs no special frequency compensation network which is suitable for this low frequency application.

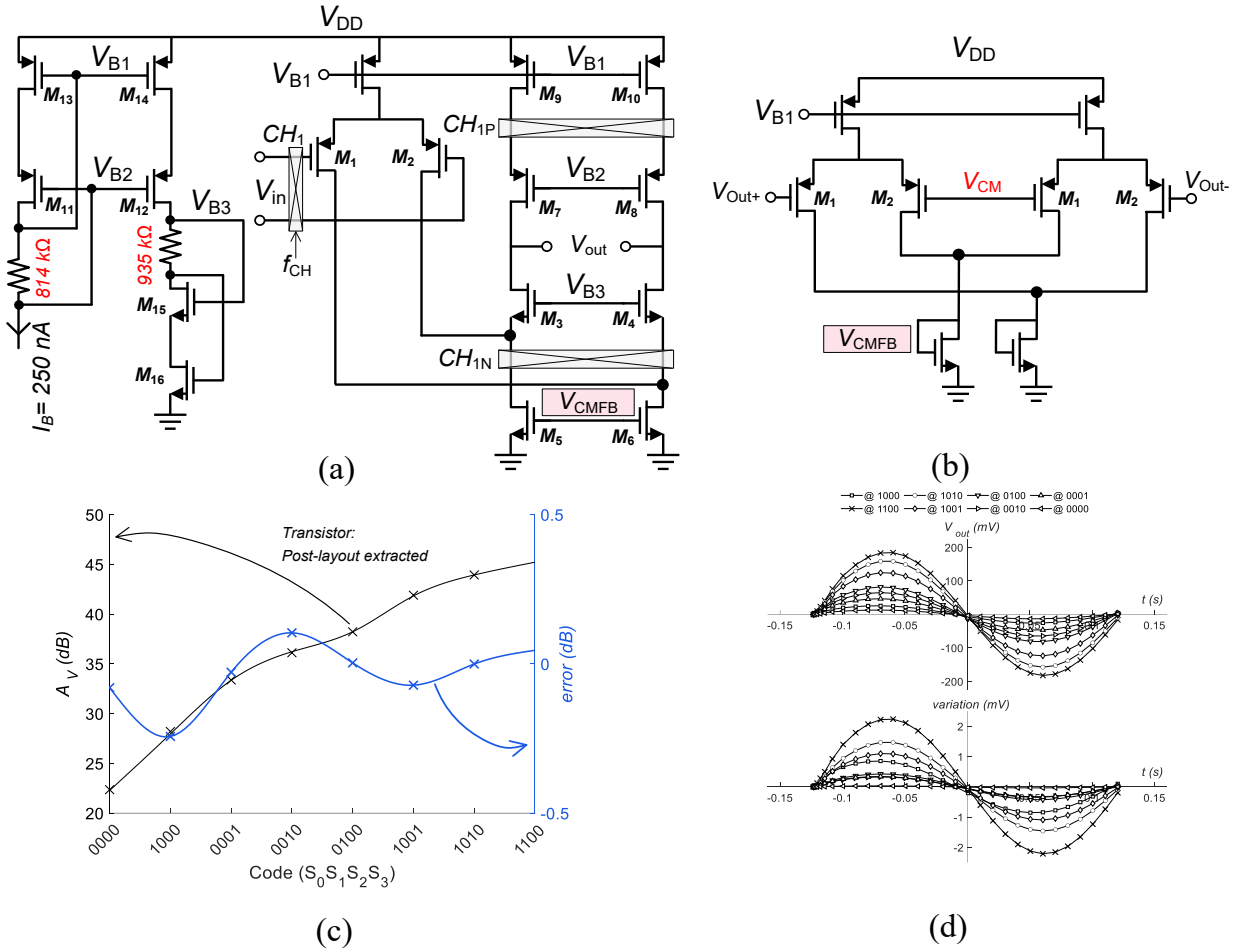

***Figure 28**: Folded cascode amplifier (a) Transistor details (b) Common-mode feedback (c) Post-layout extracted results (d) Transient domain output waveforms when the input in only 1 mV. R_1 & R_2 are biasing resistors used to balance voltages in the network for low power operation.*

PMOS is selected for the differential pairs since an n-well technology is available. The small-signal open loop gain is given by:

$$A_v \approx g_{m1} R_{out} \qquad 54$$

where the R_{out} is the output impedance and it is derived as:

$$R_{out} = g_{m3} + g_{mb3} r_{o3} \; r_{o1} || \; r_{o5} \; g_{m7} + g \qquad 55$$

The postlayout simulation results presented in Figure 28(c&d) displays the gain programmability and the transient simulation, respectively. One of the disadvantages of the feedback resistor network is its non-monotonic behavior. The results are not compared to the best curve fitting in this case, instead it's compared to the expected gain out of the R_{PGA} value. The generation of non-overlapped reference phase is shown in Figure 29(a) and its timing diagram is shown in Figure 29(b).

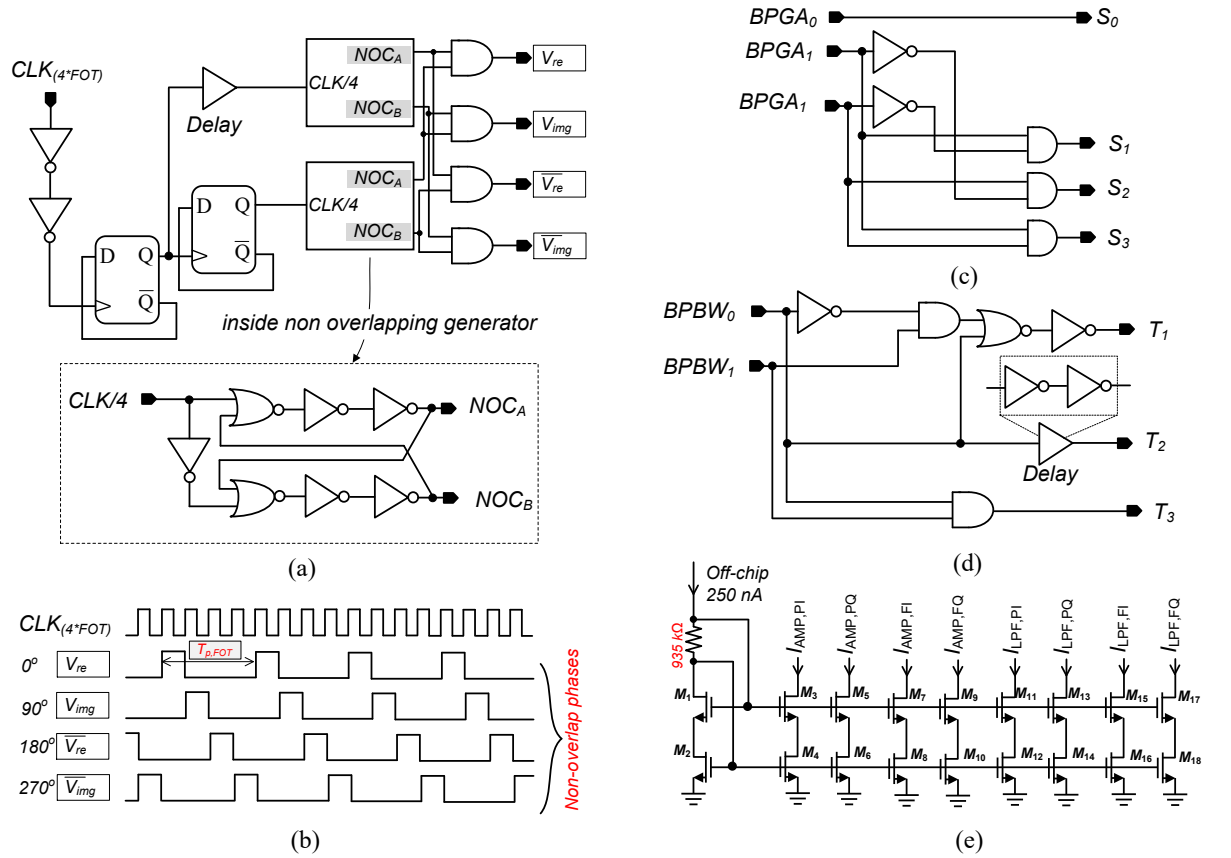

***Figure 29**: The reference FOT signal four phases generation and (b) the timing diagram of the waveforms. (c) The PGA encoder. (d) Bandwidth switch encoder. (e) Biasing current distribution.*

The CLK input is four times higher than the FOT signal and is divided on chip for the appropriate mixing phases. Figure 29(c&d) shows the digital encoder for programming the gain and bandwidth respectively. This process is accomplished by changing the bit off-line to meet the signal requirement. The current distribution network is shown in Figure 29(e). To accomplish very low cutoff frequencies (< 10 Hz), the required *RC* product size needs to be very large as shown in Figure 30.

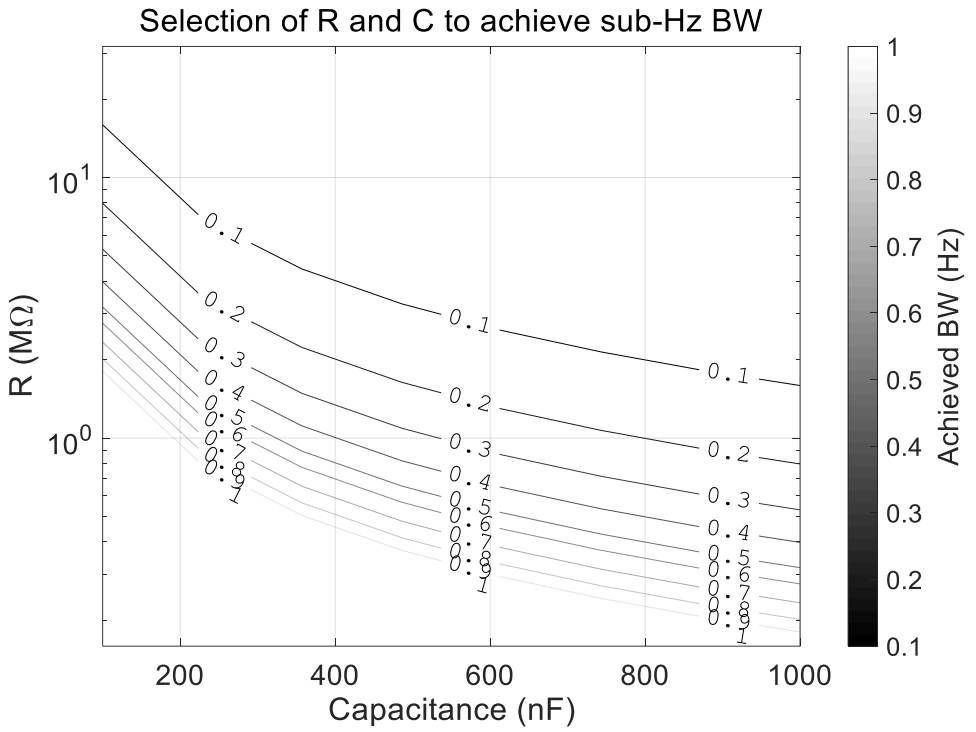

***Figure 30**: R and C projection for sub-Hertz bandwidth*

This may not be possible considering the small on chip capacitance values available in the CMOS technology which limit the on-chip practical capacitor values to less than 50 pF. To combat this issue, a capacitor-multiplier based filter was used. Though modified to consume less power, and achieve a higher capacitive multiplication factor, it was adopted from the filter topology presented by [79]. The configuration of this approach is shown in Figure 31(a&b). The LPF transfer function is derived as follows:

$$V⁡out⁡⁡ V⁡in⁡⁡ = \quad a⁡o⁡⁡ \tau⁡2⁡⁡⁡ \ R⁡2⁡ C⁡eq⁡2⁡s⁡2⁡ + 3R\ C⁡eq⁡s + 1⁡ \qquad 56$$

where $V⁡out⁡$ is the filter's output voltage (i.e., $V⁡LPF⁡$) and $V⁡in⁡$ is the PGA amplifiers output voltage. By comparing (58) to the standard form of the second order system in (59) as:

$$H\ s⁡ = \quad a⁡o⁡⁡ \tau⁡2⁡⁡⁡ \ s⁡2⁡ + \ 2\zeta⁡\tau⁡s + \ 1⁡ \ \tau⁡2⁡⁡⁡ \qquad 57$$

where $\tau = R\ C\square eq\square = 1\square\ \omega\square 3dB\square\square$ and $\zeta = 1.5$ which is the damping ratio ($Q = 1\square 2\zeta\square$). The value of resistor $R = 28.5\ M\Omega.dc\ gain = a\square o\square\square\ \omega\square 3dB\square 2\square\square \approx -6\ dB$, and the $C\square eq\square$ is calculated according to (60),

$$C\square eq\square = \beta\ C\square A\square + j = 1\square 3\square\ T\square j\square\ C\square L(i)\square\square\square \qquad 58$$

where $i \in \{1:3\}$ and $L\ i\square \in \{B:D\}$, and β is ~ 300 in this design topology (Figure 31).

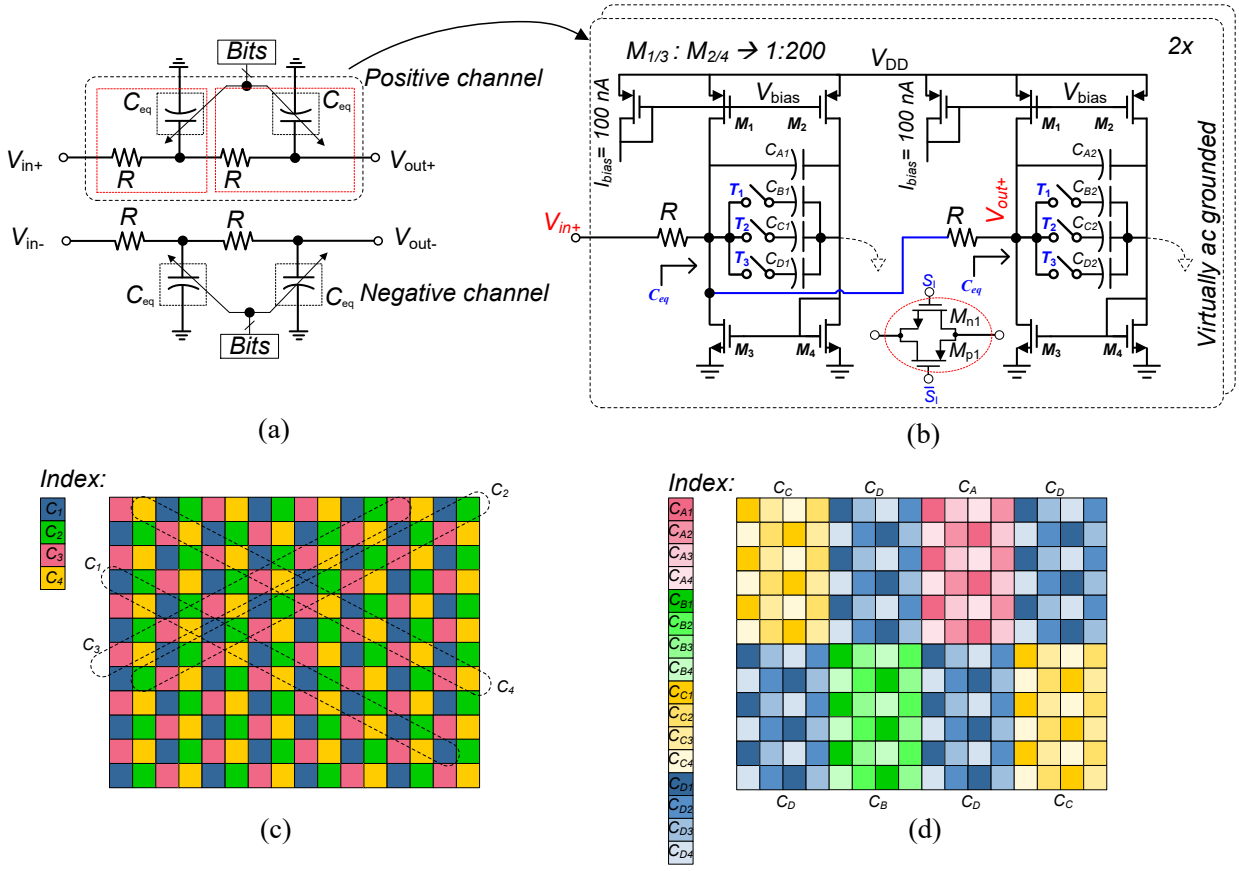

Figure 31: *(a) DC components filtering scheme: (b) Capacitor matching between Channels & 1st / 2nd stages (c) Capacitor matching between banks (d) Full capacitor distribution.*

The value of capacitors are as follows: C_A= *6 pF*, C_B= *6 pF*, C_C= *12 pF*, and C_D= *24 pF*. Process variations affecting capacitance and bandwidth were a major consideration. The four equivalent

capacitors in Figure 31 (a) are physically staggered as shown in Figure 31(c), to prevent mismatch between differential channels. The capacitor banks that are switch controlled in Figure 31(b), are broken down further in Figure 31(d). Capacitors with subscripts 1 and 2 are in the signal path V_{in+}, These are identical to capacitors with subscripts 3 & 4, which are in the V_{in-} signal path. The frequency response is presented in Figure 32 with the configurable bandwidth.

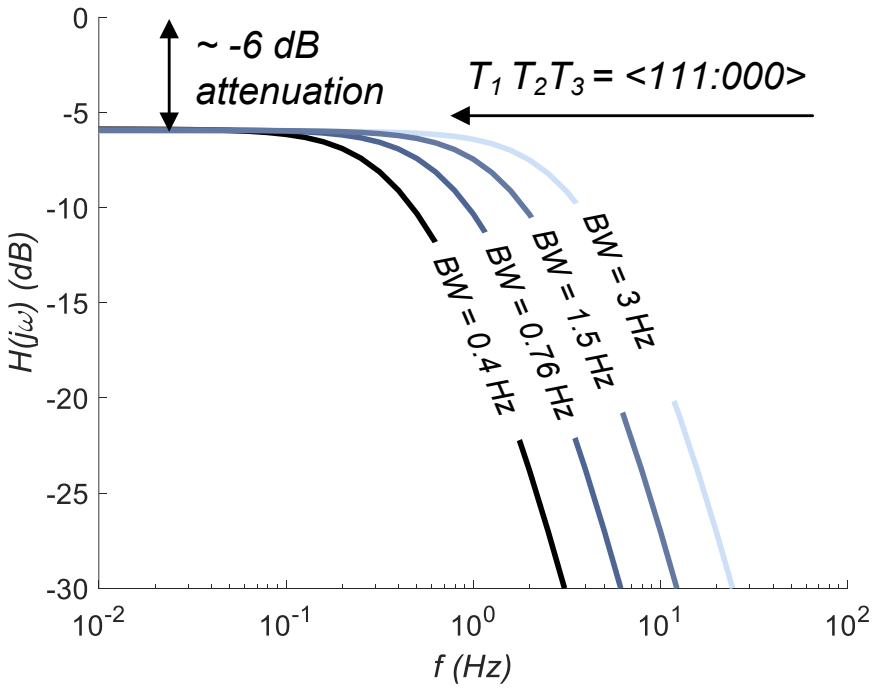

***Figure 32**: Transistor-level frequency response of the c-multiplier based filter in Fig. 10(a) and formula (22).*

The very last stage to capture the pressure and flow information, is the high impedance buffer. There are four fully differential buffers for four channels. The circuit is shown in Figure 33. As an application-specific low frequency environment, the common-mode detection is accomplished by using passive resistors as linear elements. While NMOS transistors are faster than PMOS, in this circuit PMOS have been chosen for handling lower input swing as the speed is not a requirement for the design. Also, PMOS is selected for the differential pairs since an n-well technology is available.

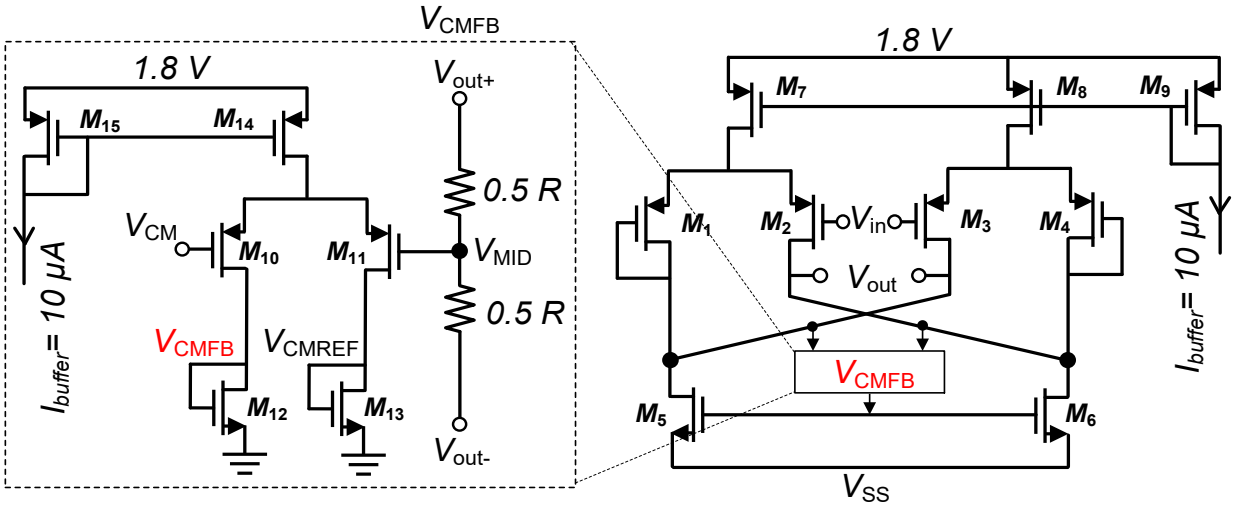

***Figure 33**: The buffer circuitry details.*

IV. Measurement Results

The proposed sensor based on the quadrature lock-in concept is fabricated in a standard 0.18µm TSMC 1P6M mixed-signal process. Figure 34 shows the chip microphotograph of the manufactured design and its layout.

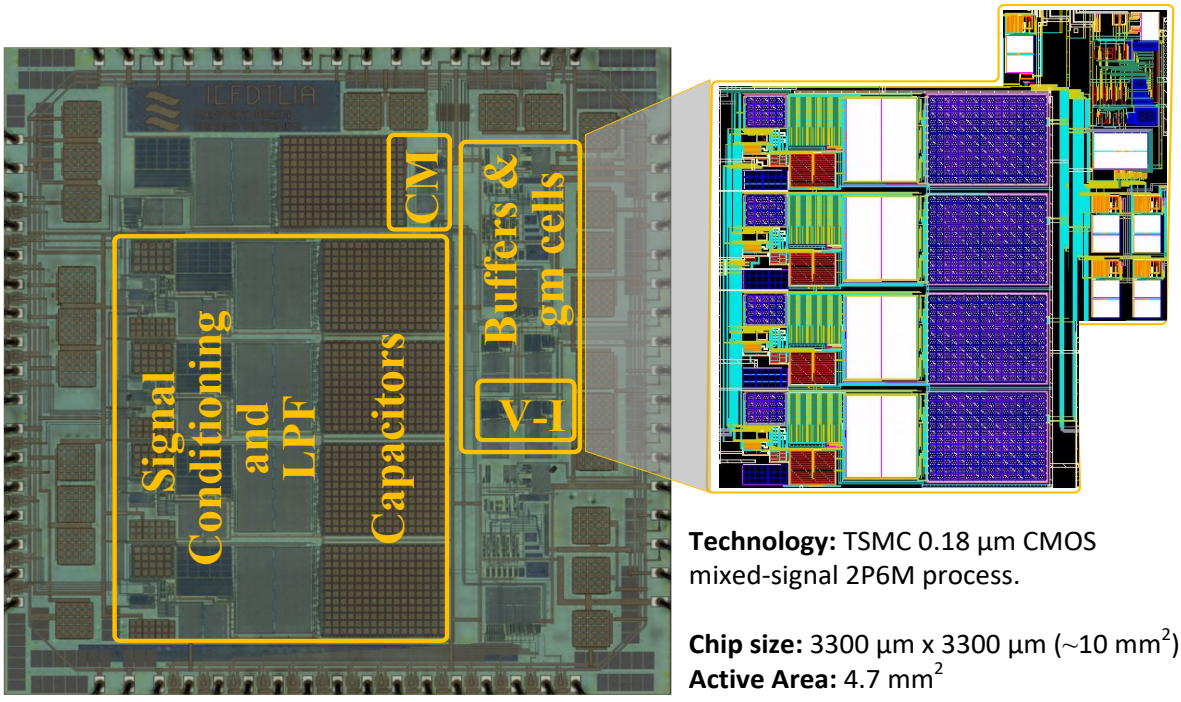

Technology: TSMC 0.18 µm CMOS mixed-signal 2P6M process.

Chip size: 3300 µm x 3300 µm (~10 mm^2)
Active Area: 4.7 mm^2

***Figure 34**: Chip microphotograph.*

The system occupies an active area of 4.7 mm^2. The die is packaged and mounted on a PCB for a configurable experiment. A four-channel 6.25 GS/s MSO54 high-speed real-time Tektronix oscilloscope is used to observe the waveforms of the circuit. Input signals for pressure and flow are generated through a Keysight 81150A-120 MHz function generator. Power to the PCB housing the chip is supplied by a Sorensen XPF60-10D power supply. The control and timing signals are generated on the PCB from an Arduino© *firmware* board, and finally, a PSoC 6 BLE evaluation board is used for its 16-channel scanning SAR ADC to sample and stream the data to a laptop computer. The experiment setup is shown in Figure 35.

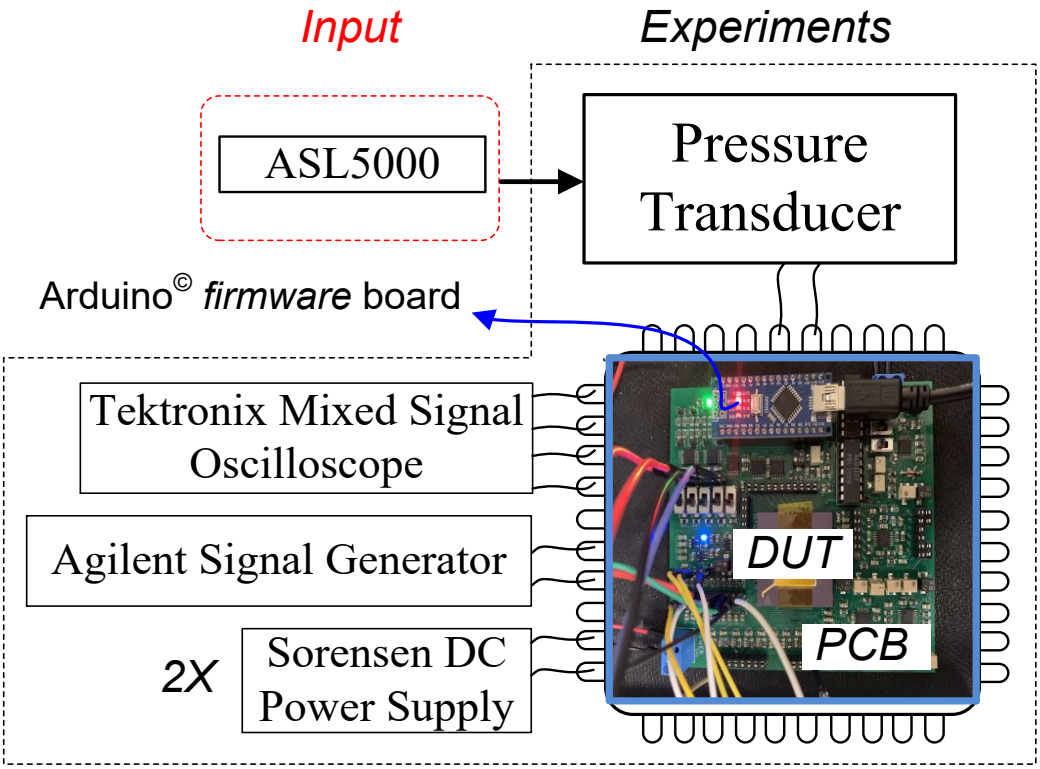

***Figure 35**: Experiment setup block diagram configuration.*

The characterization of the chip is done in multiple ways. One, by sweeping the phase $(0 \rightarrow 2\pi)$ between the input and down-conversion clock phase for a single channel and capturing the output.

The input phase and expected output phase measured by the LIA is compared for phase measurement accuracy. The signal with sweepable phase was sourced by a function generator and placed on the flow input pin of the chip. The pressure input channel was used as a control to measure the phase drift of the input over time, as the function generator was not phase locked with the down conversion frequency. With raw data collected from both the down converted and filtered, in-phase and out-of-phase, flow and pressure channels, (F_Img, F_Re, P_Img, P_Re), the phase drift offset was then corrected by subtracting the reference phase (measured as a control on the pressure input) from the intentionally incremented phase (measured on the flow input) as shown below:

$$\phi\_offset = \tan^{-1}\left(\frac{F\_Img(n)}{F\_Re(n)}\right) - \tan^{-1}\left(\frac{P\_Img\ n}{P\_Re\ n}\right) \quad 59$$

The raw and corrected phase measurements are shown in Figure 36.

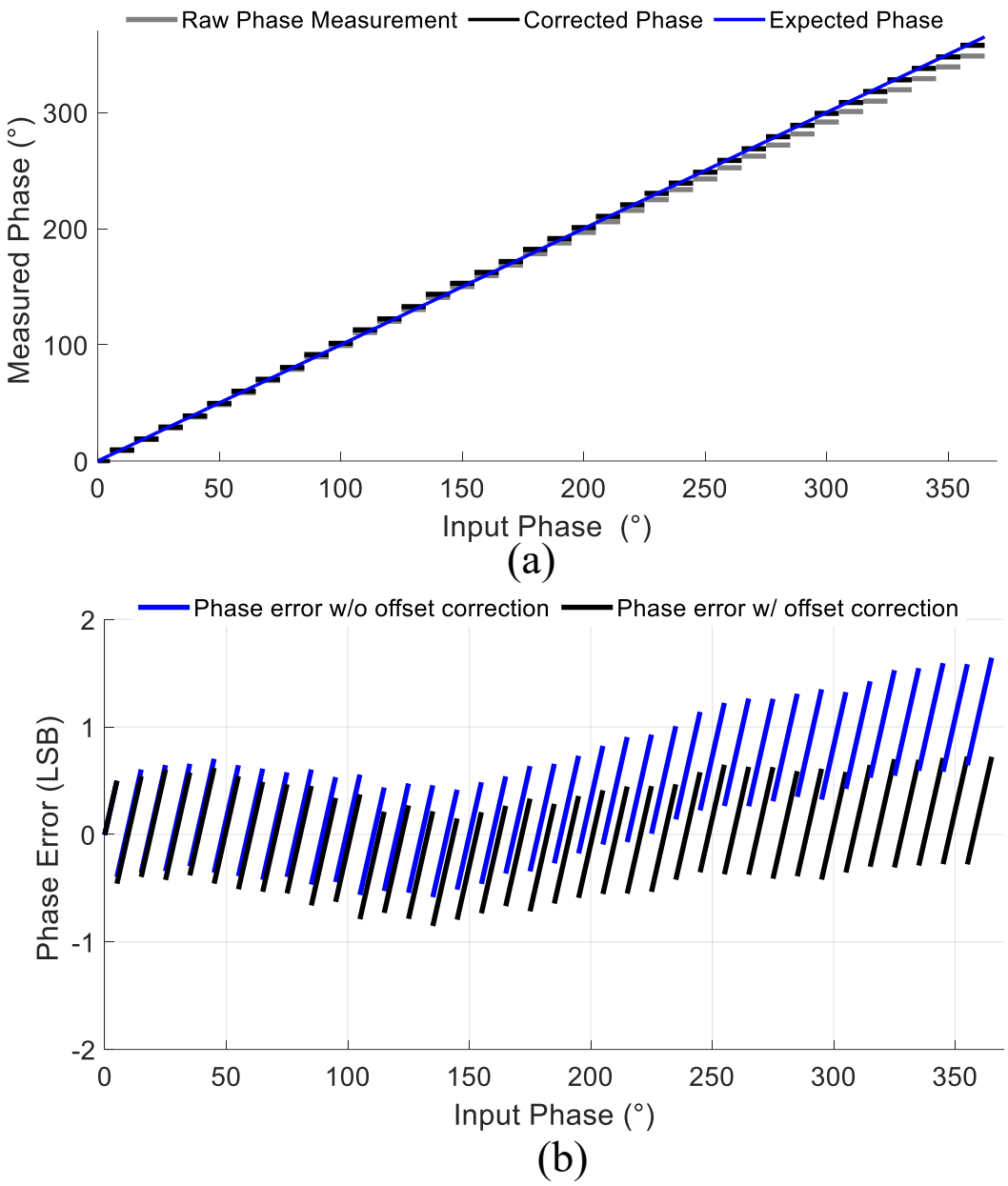

***Figure 36**: Phase transfer characteristics. Shows the linearity of the phase measurement and error. Function generator was stepped in 10° increments*

The second method involves sweeping frequency above and below the mixing frequency, then observing the filtered output signals amplitude responses. Figure 37. demonstrates this principle, where progressive increases in Δf, (Δf being the difference between the down-conversion and input frequency) cause time dependent variations in the filtered outputs. When the frequencies are matched, Figure 37(a), there is no variation in time. Though with only 0.1Hz offset, Figure 37(b),

the signal can be seen changing in response to the phase accumulation between the mixing frequency and input frequency. This accumulation is very small compared to the period of FOT, and therefore is only visible on the large time scale of the I&Q measurements. As Δf increases further, Figure 37(c&d), the frequency variations increase, and amplitude response sharply declines.

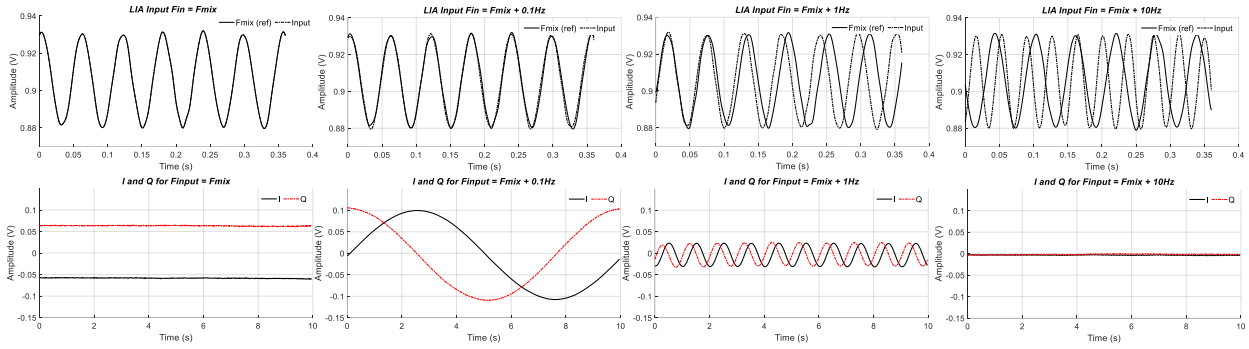

***Figure 37**: Frequency drifting measurements. As the input frequency deviates from the down-conversion frequency, the phase accumulation can be seen by a low frequency DC variation, with higher frequency variations being heavily suppressed.*

In Figure 38, additional amplitudes are swept along with frequency to make visualizing the response more intuitive. This results in a linear relationship as amplitude varies at the down conversion frequency, and a sharp non-linear decline in signal amplitude as the frequency is varied. This normalized LIA response is shown in Figure 38.

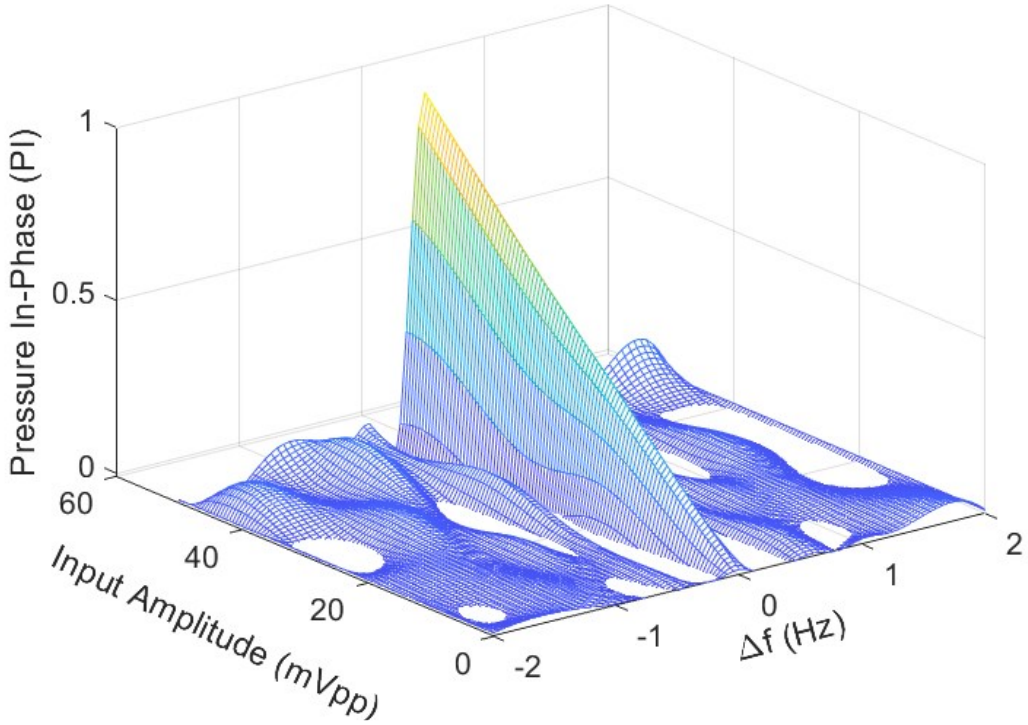

***Figure 38**: Normalized LIA response as a function of frequency drift and input amplitude. This shows how the response is linear in amplitude changes at the down conversion frequency and highly non-linear in frequency deviations.*

Power characterization is done by measuring the voltage drop across 100 Ω resistors, routed from the LDO's, in series with each of the power pins feeding the chips major components, then sampled, and their difference to the supply voltage taken. The architecture system consumes ~ 429.63 µW (including buffers). The breakdown of this power dissipation is indicated in Figure 39.

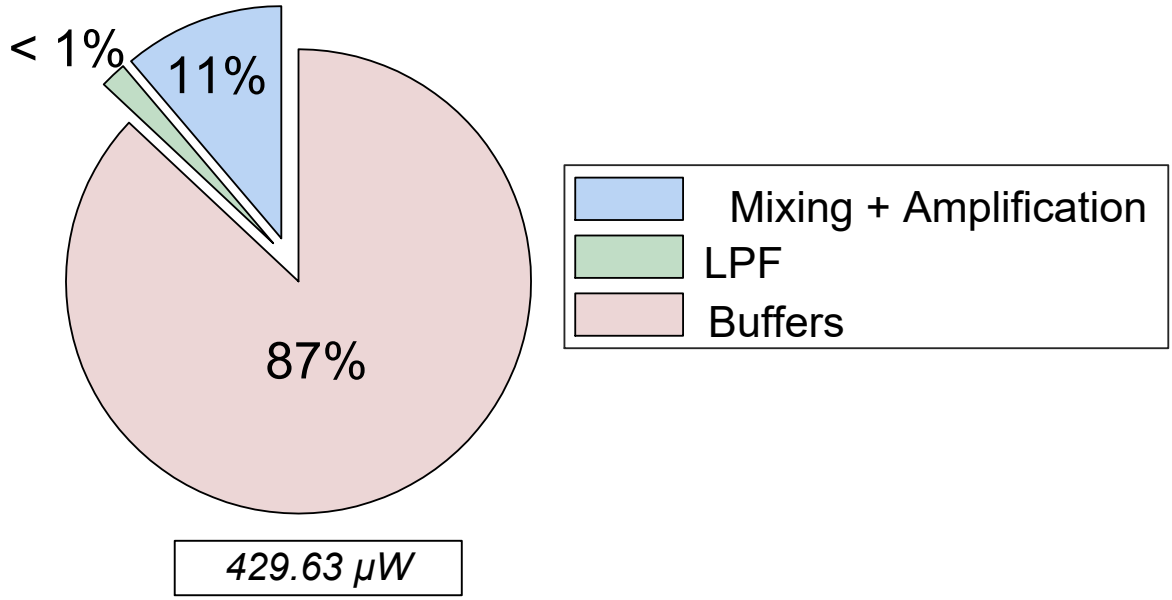

***Figure 39**: Power dissipation breakdown. Mixing and amplification consumes 48.83 µW, LPF consumes 0.8 µW, and drivers consumes 380 µW.*

Further characterization is done by using ADSL500 lung simulator machine (to emulate the real patient) with FOT, driving a speaker connected to the respiratory system and capturing the resulting pressure and flow, AC coupling this signal to the chip, and measuring the resulting signals. The raw data collected by the LIA would be processed and evaluated in MATLAB, then compared to the conventional STFT methodology. The impedance reading $Z(\omega)$ ($R(\omega)+jX(\omega)$) would be obtained in $cmH_2O/L/s$ according to the following ratio:

$$Z = Z * \frac{K_P}{K_F} \qquad 60$$

where K_P (in cmH_2O) and K_F (in L/s) are the pressure and flow transfer gain of the system, respectively. This gain can be different from transducer to transducer. In summary, the proposed architecture functions as expected. It outputs the impedance information proportional to the amplitude and phase of the frequency of interest.

V. Conclusion

This work demonstrates the functionality of a silicon-based solution to synchronously extract parameters of lung mechanics. By leveraging the concept of homodyne down conversion, the information of the phase and the amplitude of the stimulation frequency is obtained instantaneously. The proposed lock-in approach is an area and power efficient solution and is suitable for standard CMOS manufacturing. The obtained measurement results are very promising, making this sensor an alternative option to measure lung impedance, thus empowering the current challenges of implementing portable integrated systems to offer affordable health monitoring devices.

Acknowledgment

The authors would like to acknowledge the Natural Sciences and Engineering Research Council of Canada (NSERC) and NovaResp Technologies, Halifax, Nova Scotia, Canada, for supporting this project. Acknowledgment is also due to Dalhousie University for providing the facilities. The authors also acknowledge CMC Microsystems, Kingston, Ontario, Canada, for IC fabrication services and CAD tool support.

Chapter 5 : SUPPLEMENTAL ANALYSIS & RESULTS

This chapter includes additional information, design, simulation, and results for the lock in amplifier blocks, and ultrasonic sensor that supplements the previous two chapters. This chapter includes analysis of the time-of-flight capture methodology and analysis, additional sensor geometry results, sampling / pulse repetition rate experimentation and temperature data. Additional results and analyses of the Amplifier and low pass filter blocks are included, as well as the synchronous generation of FOT and clock driving signals.

I. Introduction

Adequate resolution, reliability of measurement, reduction of noise and sampling frequency are paramount to sensor and signal processing design. The supplementary details in this chapter highlight their analyses and design process and measure the reliability, sampling rate, noise profile and resolution of the various platforms in this dissertation. Supplementary details for Chapter 3 are included in Section II, while supplementary details for Chapter 4, included in Section III.

In Section II.A, two major methods of time-of-flight capture for ultrasonic waves, both envelope detection and zero crossing have been investigated and compared for efficacy in reliability of measurement and invariance to variation in pulse energy. Mathematical simulations relating the envelope to channel amplitude noise are shown, as well as how zero crossing detection eliminates this source of noise. After proving that zero crossing detection is superior for noise suppression, in Section II.B, the analysis of clock jitter and standard deviation in measurement due to phase uncertainly in the time to digital conversion is investigated and conclusions about use cases are made. In Section II.C, the sampling frequency of the ultrasonic sensor platform is investigated, and anti-phase pulsing is introduced to reduce ring-down time in an attempt to improve pulse repetition rate with limited success. With these analyses concluded, in Section II.D, the temperature cancellation effect of a bi-directional measurement and the linear relationship between temperature and speed of sound is shown. The bi-directional measurement is demonstrated to show how the up and down stream measurements move together, whose difference effectively cancels

speed of sound variations. Finally, in Section II.E, as a conclusion to the ultrasonic sensor, the geometry of each sensor is compared for flow resolution and range by altering the angle and length of the sensor.

Supplemental results of the lock-in amplifier in Section III.A) include additional images of cadence simulations and real data acquired from testing the amplifier output from the lock-in to demonstrate the output characteristics based on inputs before filtering. In Section III.B) The low pass filtering, bode characteristics of the low pass filter for each bandwidth setting is shown. Finally, in Section III.C), the methodology of how the synchronous demodulation is generated is shown.

II. Ultrasound Measuring System

This section is an expansion of results and analyses for Chapter 3, broken down into 5 sub-sections, A through E.

A. Time-Of-Flight Capture

Envelope and zero crossing detection are methods for extracting the time of flight of ultrasonic waves [43], [44], [52]. Envelope detection and single sided wave capture was initially considered and tested in the first prototype for the sensor platform in Chapter 3. Triggering on the envelope proved to be very noisy and only provided data that was indicative of flow and was susceptible to variations in the speed of sound, thus the envelope was used as a coarse measurement to trigger the TDC capture on the following zero crossing. The speed of sound variations is covered in a later section, but to investigate why envelope detection was noisy, and how zero crossing detection was used as a solution, mathematical modelling of the waves, trigger point and envelope are needed.

Measuring and comparing the zero-flow state and steady state CPAP flow with no resistance, thought the sensor tube, the maximum time-of-flight difference in received waves was only 3.4us. The CPAP machine's flow generates a time of flight difference with little variation in wave amplitude at steady state, however, varying the flow rate within the sensor tube caused considerable variation in received wave amplitude. Any variation in voltage supply or received

signal energy modifies the peak-to-peak voltage of the received signal and causes missed and premature/late detections on the envelope. To understand the effect of envelope detection and its susceptibility to noise as a percentage of maximum expected time-of-flight, the waveform is first approximated using the following equations:

$$A\,t\square = E\,t\square f\,t\square \quad 61$$

$$A(t) = sin\square(2\pi \cdot f\square E\square \cdot t)\square\, sin\square(2\pi \cdot f\square u\square \cdot t)\square \quad 62$$

$$y\square T\square = |\, sin\square(2\pi \cdot f\square E\square \cdot t)\square| \quad 63$$

Where $A(t)$ represents the waveform captured at the receiver, $E(t)$ represents the envelope of the pulse, $f\square E\square$ is the envelope frequency, $y\square T\square$ is a constant amplitude trigger point, $f(t)$ represents the carrier wave, and $f\square u\square$ is the carrier frequency. Equations 62 & 63 show the approximated received waveforms. However, when only triggering on the envelope, the absolute value of the envelope can be taken irrespective of the carrier (Eqn. 63). In this example, an envelope frequency of 430Hz is used. The threshold of measuring the wave phase, $y\square T\square$ is maintained constant while the amplitude of the waves will be varied to see the effect on *perceived* time-of-flight changes at steady state, i.e., flow = constant.

The measured waveform shape and the approximated shape are shown in Figure 40 and Figure 41 respectively. Although the rise and fall of the received signal is slightly less sinusoidal, the sinusoidal envelope is a close approximation and will work for the scope of the analysis.

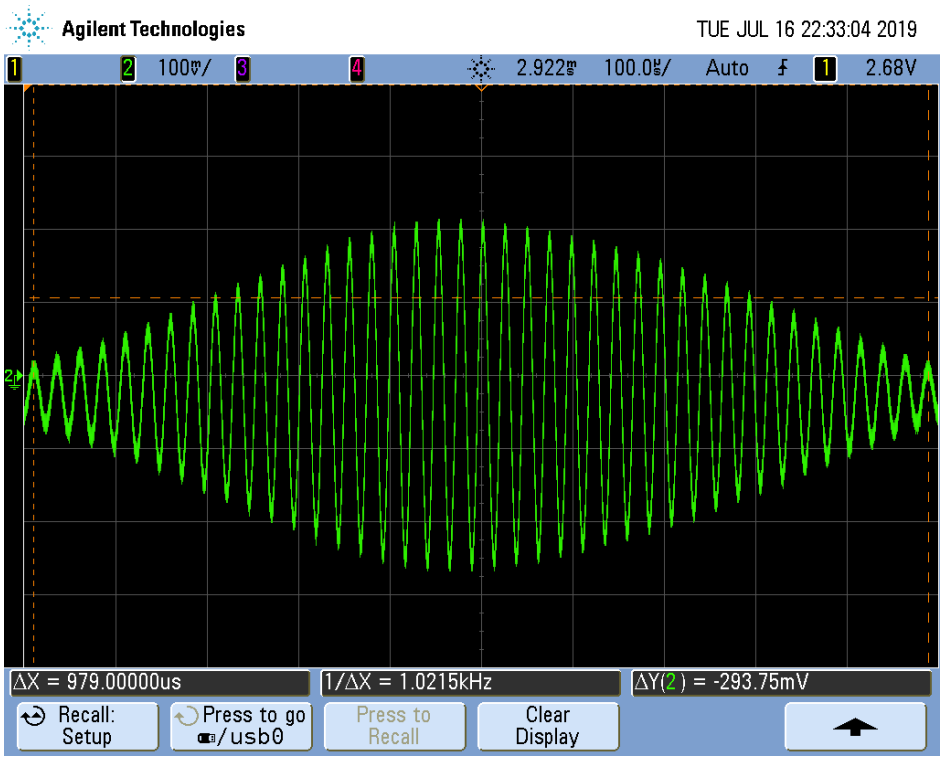

***Figure 40**: Scope capture of received ultrasonic wave. Steady state flow indicated a phase change of 3.4us using the 45-degree angled tube sensor geometry.*

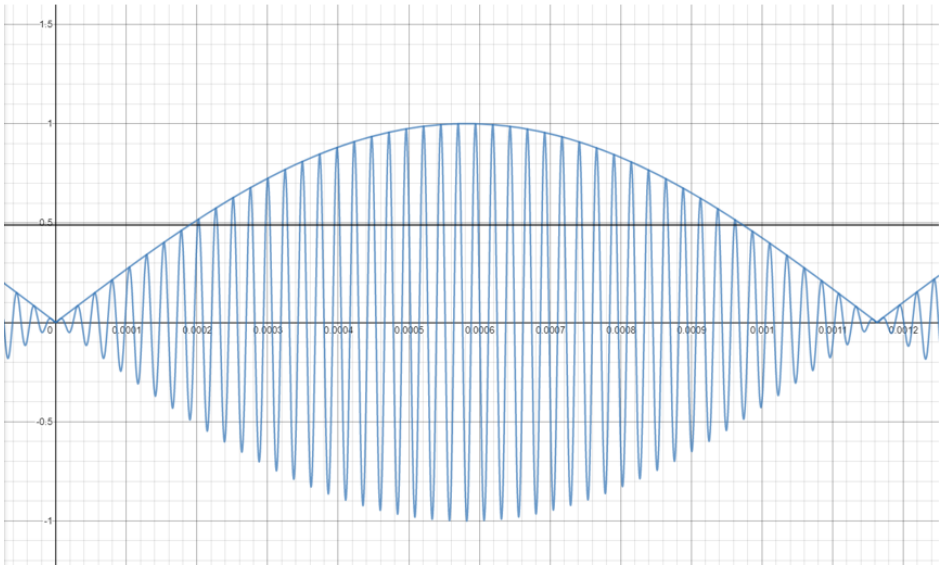

***Figure 41**: Mathatical approximation of the ultrasonic captured wave, envelope and capture threshold.*

Picking some constant threshold $y(T)$, the time t, at which an intersection occurs along the envelope wave can be derived using Equation 63, where a becomes an amplitude scaling factor, in this case,

our source of amplitude noise. The absolute value is ignored, as we only care about relative capture times.

$$y_{Th} = a \cdot \sin(2\pi \cdot f_{Err} \cdot t_{Err}) \quad (64)$$

Rearranging for time t, we get:

$$t = \frac{\sin^{-1}(y_{Th}/a)}{2\pi \cdot f_{Err}} \quad (65)$$

Using these times, the perceived phase difference measurement between two enveloped waves with differing amplitudes, and same threshold, can be expressed as a difference in time, i.e., subtracting two instances of Eqn. 65.

$$t_{diff} = t_1 - t_2 \quad (66)$$

Substituting Eqn. 65 into Eqn. 66, and setting $a = 1$ in the reference instance, and merging denominators, the time difference can be expressed as:

$$t_{diff} = \frac{\sin^{-1}(y_{Th}) - \sin^{-1}(y_{Th}/a)}{2\pi \cdot f_{Err}} \quad (67)$$

When a is 1, the terms cancel out and the perceived time difference $t_{diff} = 0$. However, as a changes, the terms no longer cancel, and a measurable time difference emerges. Working backwards with the measured time-of-flight difference earlier (3.4us), the amplitude noise that could cause a late detection of 3.4us would be calculated as follows: Using $t_{diff} = 3.4us$, $y_{Th} = 0.5$, $f_{Err} = 480Hz$, and solving for a:

$$a = \frac{y_{Th}}{\sin[\sin^{-1}(y_{Th}) - 2\pi \cdot f_{Err} \cdot t_{diff}]}, \quad a = 1.018 \quad (68)$$

Thus, only a 1.8% change in wave amplitude causes a full measurement range of error (3.4us ΔTOF) when y_{Th} is chosen at 0.5. Demonstrating this effect in Figure 42, we have a zoomed in image of three sinusoids and their respective envelopes, one with zero phase shift, another with a phase difference equal to 3.4us and a third with an amplitude scaling of 1.7%. We can see in Fig. 42 that the red and green waveforms appear to have the same phase shift compared to the blue waveform when triggered on their envelopes, indicating a very large flow rate in both cases, but the green case has no flow rate change, only amplitude scaling.

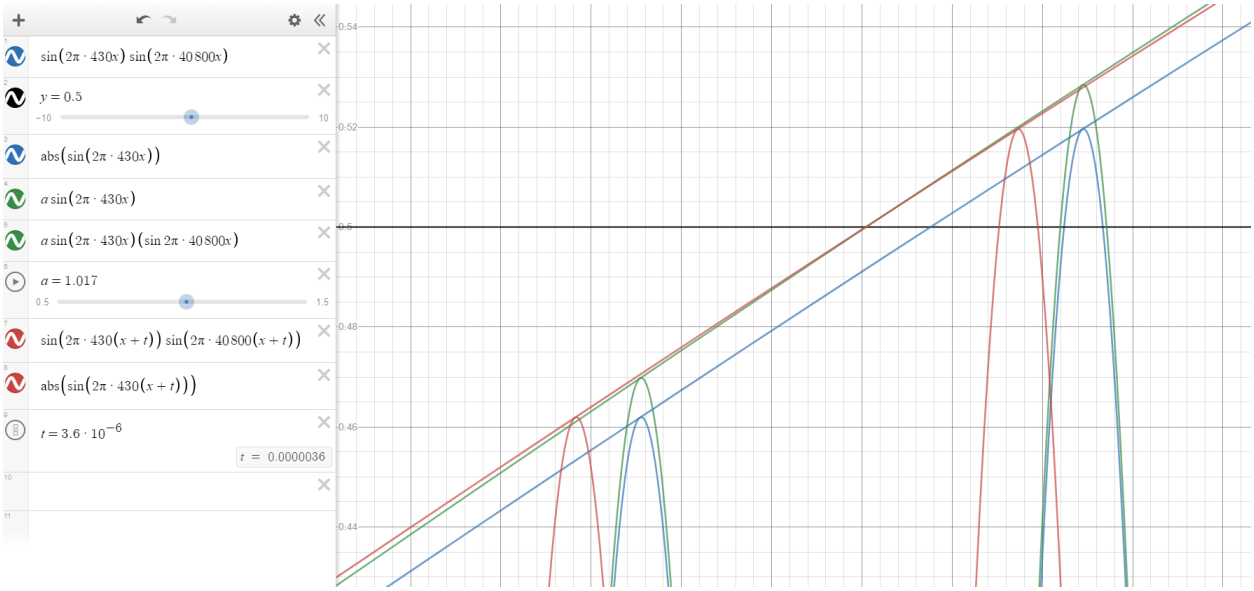

***Figure 42**:. Verifying in Desmos (online plotting tool), blue is the original signal, red is the signal with the CPAP running at max flow, and the green is the original signal with no phase shift but with an amplitude scaling equal to (a = 1.7%) and black shows the threshold line.*

This indicates that the moment an envelope triggers a TOF measurement that is 3.4us greater than expected, it's not clear whether it was a massive change in flow, or a very small change in amplitude. Ultrasonic envelope detection time-of-flight TDC is thus highly susceptible to noise that affects wave amplitude.

With this knowledge, we know the ideal scenario is where the perceived time difference, $t\Delta d$, is 0 at steady state, and $t\Delta d$ is also linearly related to the flow being measured when not in steady state. This perceivable time difference due to amplitude variations will go to zero as the relative amplitude goes to 1, this means that normalizing the data before triggering could reduce or remove this effect dependent on the efficacy of normalization process. More importantly though, as the trigger level (yT) approaches zero, the effect of amplitude scaling diminishes, isolating the phase changes from amplitude dependence. This means that using zero crossings of a waveform decouples time-of-flight measurements from noise affecting wave amplitude. However, when using the envelope as a trigger point, the envelope never crosses zero, i.e., goes negative, due to the nature of an envelope detector. Thus, triggering on the zero-crossings of fC at 40Khz would be more effective in determining phase changes, as it would be invariant to wave amplitude.

Using this knowledge, the first prototype was simulated in Tina. The simulated circuitry is shown in Figure 43. The envelope of the wave was used as a coarse “measurement” to trigger the zero-crossing detection. A kind of pulse energy detection, to signify that an ultrasound wave has arrived. A pre-set timer would also work for triggering a measurement, though this would be used in later designs. The rising edge of the envelope was detected with a rising edge detector, which enabled the following rising edge of the zero-crossing detector to signal a capture of the TDC value as a finer measurement. The simulated circuit results are shown in Figure 44 & Figure 45. The TDC measurement was still reliant on the amplitude in some sense, considering the envelope was used to determine the coarse time of when to take the measurement. Though this was offset by taking the modulus of the measurement with 2π. This had the effect of making the measurement capped to a 0 - 2π measurement, though was now largely independent of pulse energy. The breadboard layout for the simulated circuit is shown in Figure 46 while the actual results of the circuitry are shown in Figure 47 & Figure 48. We can see how the simulation matches the implementation very well, comparing figure pairs Figure 44 / Figure 47 and Figure 45 / Figure 48

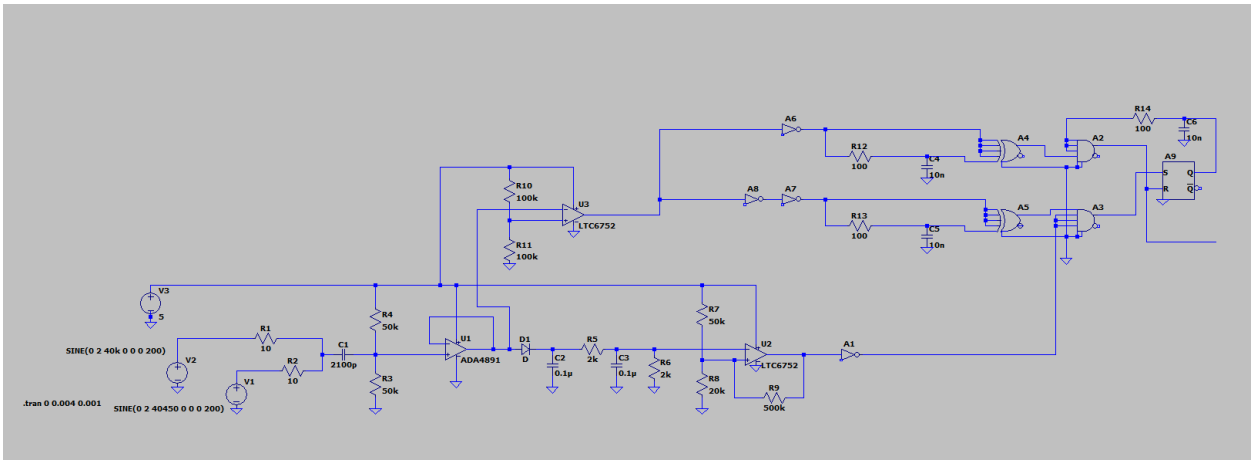

***Figure 43**: Simulated circuitry for Time of Flight generation and measurement*

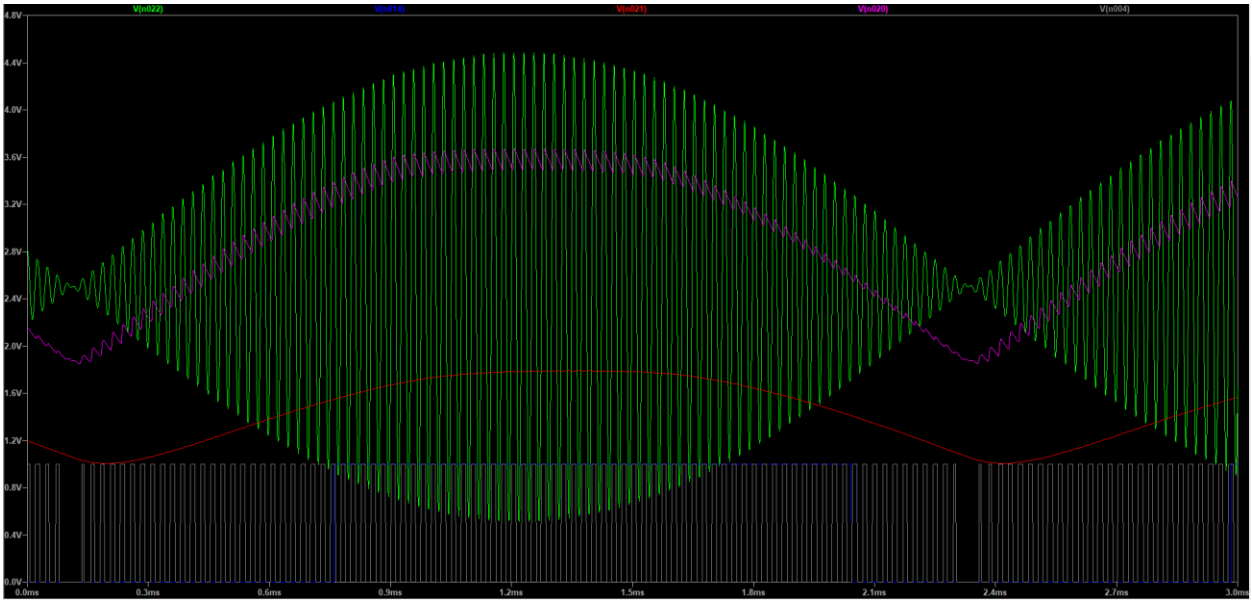

***Figure 44**: Simulation result of the time-of-flight generation and capture for initial prototype. Green = Received wave, Pink = 1st stage envelope filter, Red = 2nd stage envelope filter, blue = Trigger output from 2nd stage envelope filter, grey = zero crossing trigger.*

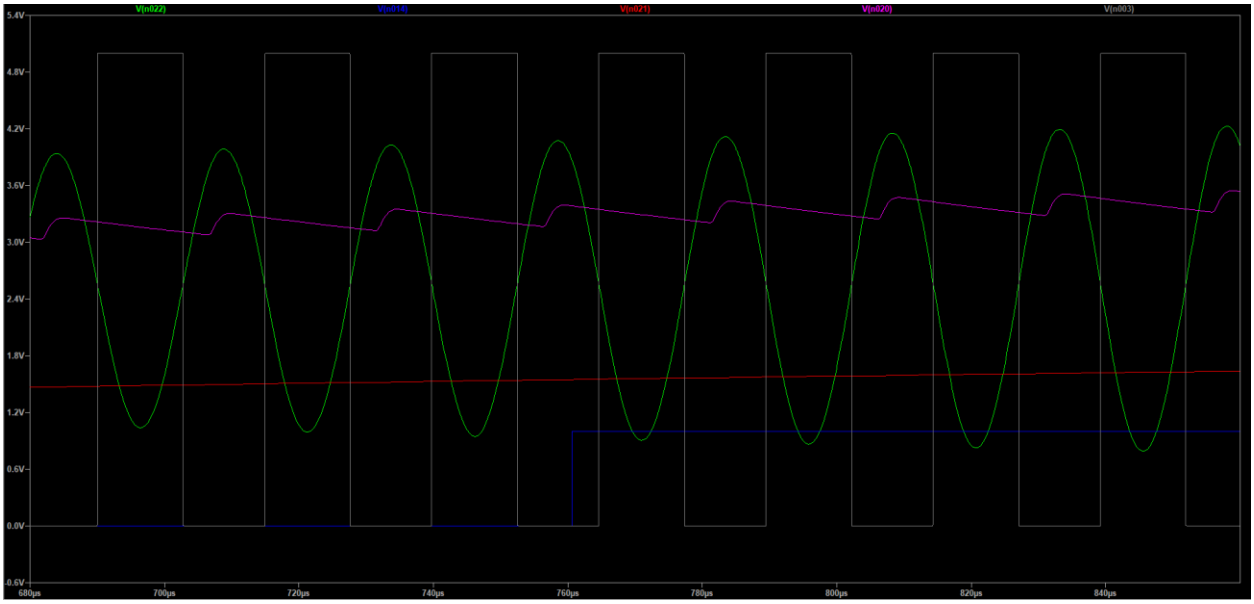

***Figure 45**: Simulation result of the time-of-flight generation and capture for initial prototype, zoomed in. 2. Green = Received wave, Pink = 1st stage envelope filter, Red = 2nd stage envelope filter, blue = Trigger output from 2nd stage envelope filter, grey = zero crossing trigger.*

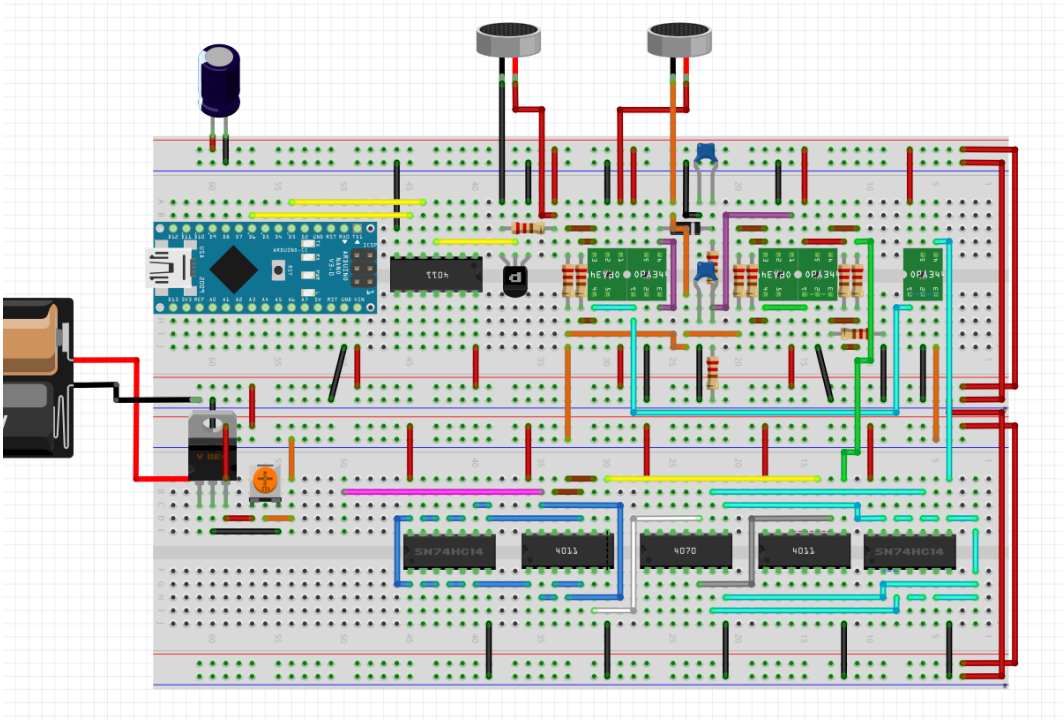

***Figure 46**: Ultrasonic sensor first prototype breadboard layout plan*

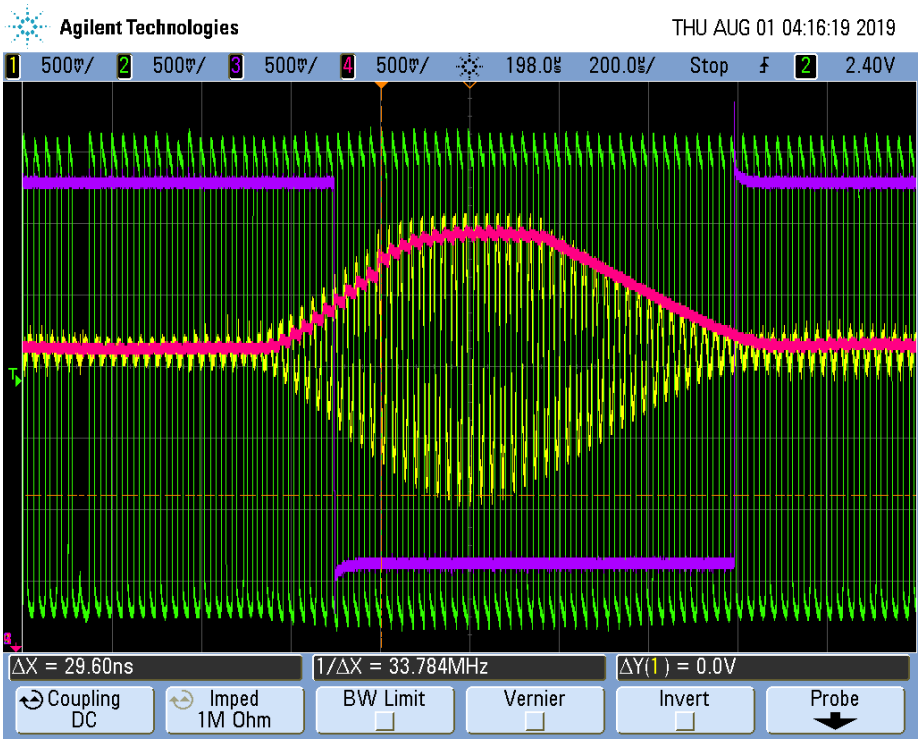

***Figure 47**: Scope results for the initial prototype for time-of-flight generation and capture. Purple (Envelope detector trigger), green (zero crossing detection trigger), Yellow (Received waveform), Pink (Wave envelope)*

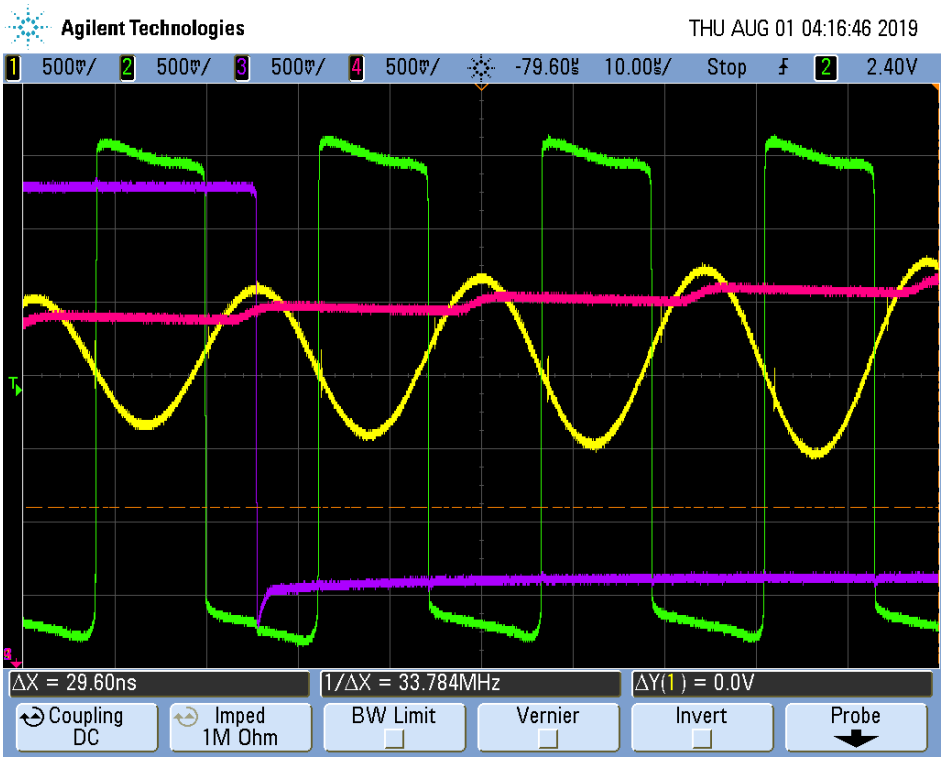

***Figure 48**: Zoomed in scope results for the initial prototype for time-of-flight generation and capture. Purple (Envelope detector trigger), green (zero crossing detection trigger), Yellow (Received waveform), Pink (Wave envelope)*

The sensor was hooked up to a 3L syringe, and air was blown in and out of the sensor in an oscillatory pattern (Figure 49), which shows the function of the sensor is working, though susceptible to speed of sound variation and is not as high resolution as it could be. This proof of concept was promising, and further development could occur.

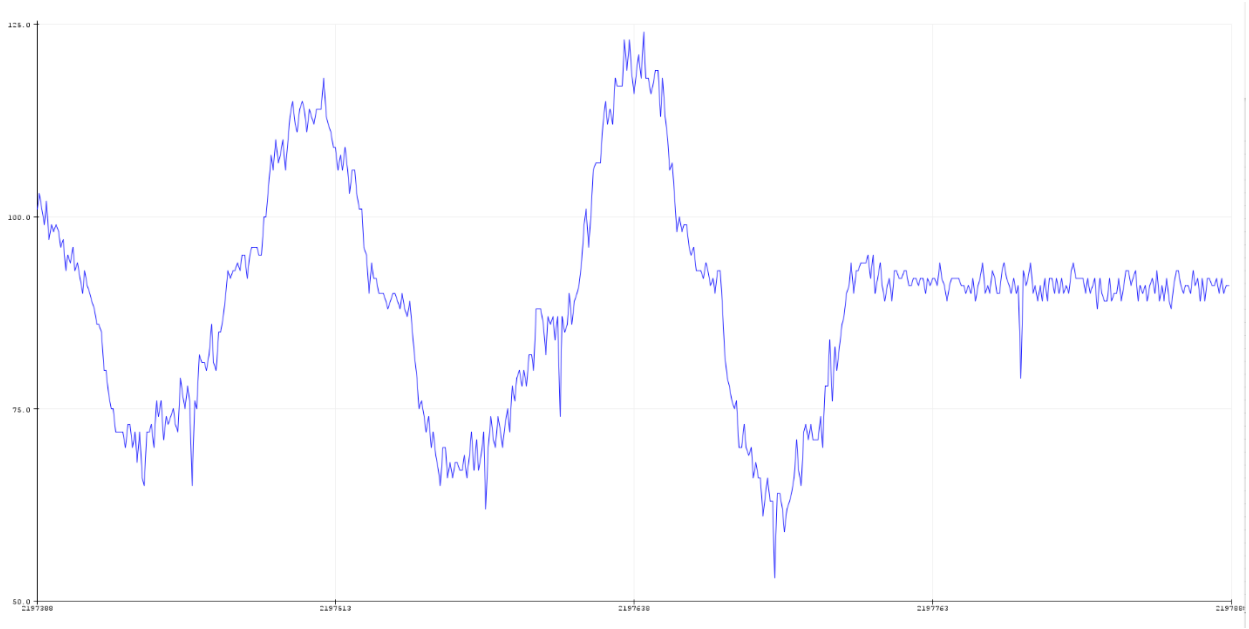

***Figure 49**: Data captured from ATMega328p and fed to PC through USB. A 3L Syringe was used to induce the flow patterns seen in the figure.*

B. Time of Flight Measurement STD

To improve upon the sensor, data was captured to analyze sources of error. 10,000 samples (30 seconds of data at ~320 samples/second) of send and receive waveforms were saved, showing over 200,000 zero-crossings in a zero-flow state. 18 zero crossings per sample were taken along each recieve waveform, beween 340us and 834us and plotted. Figure 50 & Figure 51 show the captured data and how the zero crossing measurements were taken.

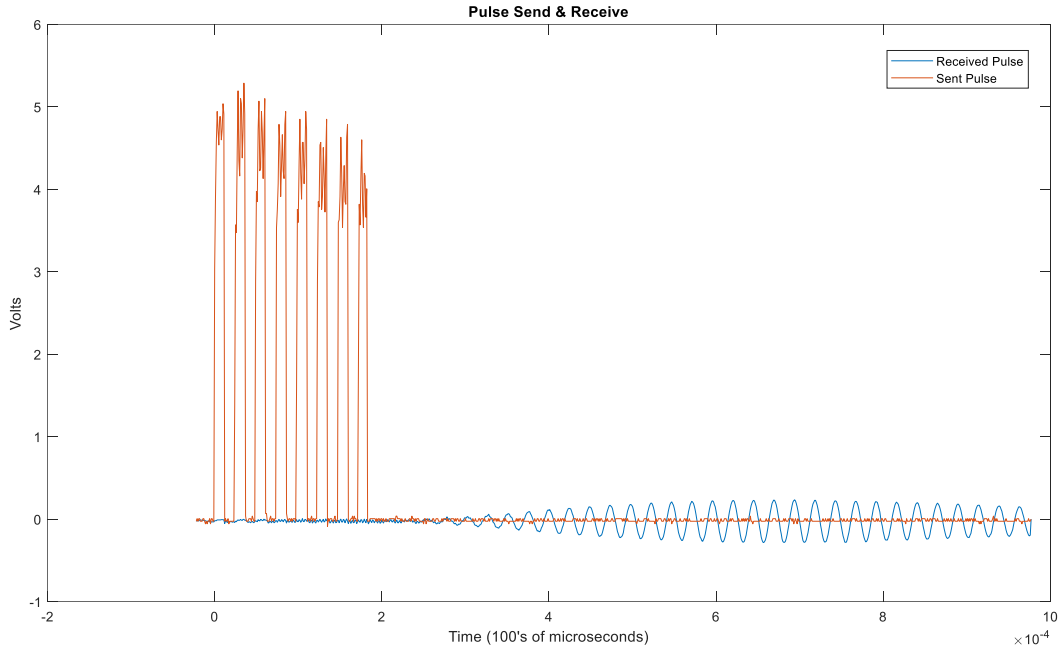

***Figure 50**: One data set graphed in MATLAB for a send and receive pulse.*

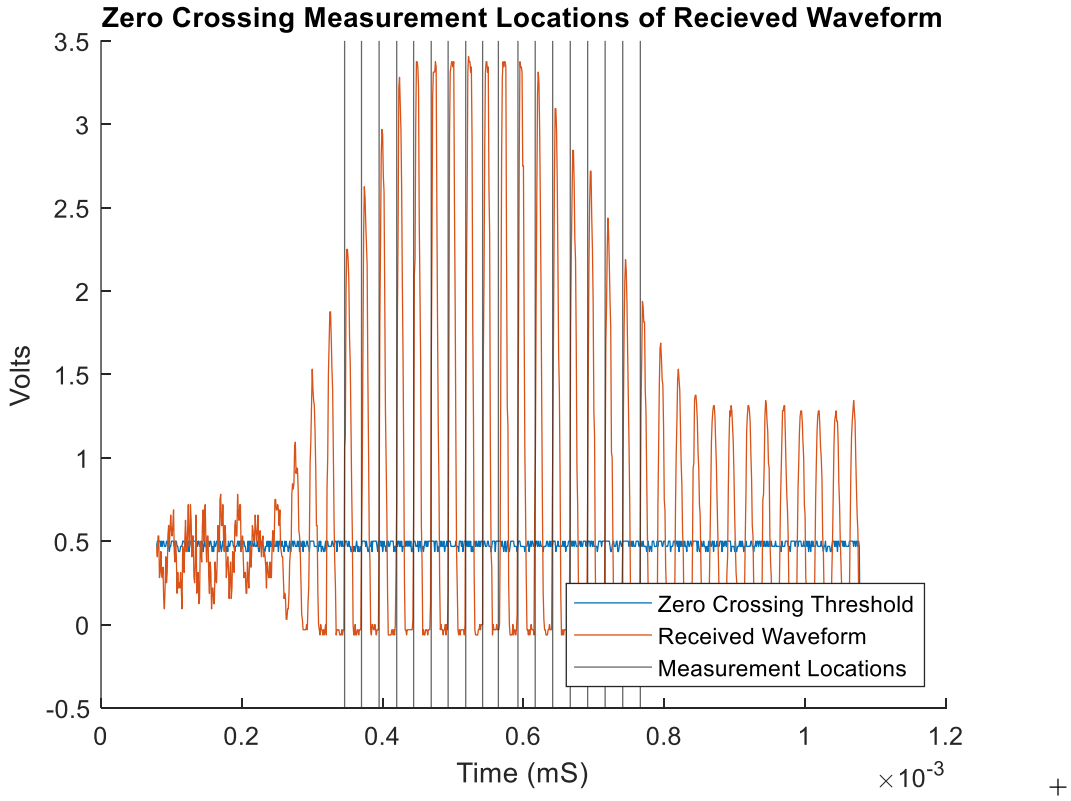

***Figure 51**: Waveform phase capture locations.*

To illustrate the effect of "when" the time-of-flight measurement is taken, on measurement reliability, all of these zero crossings (Figure 51) were plotted with their TDC value (Figure 53). Where Figure 52 shows only one zero crossing, but in more detail. Figure 53 shows all of the measurements plotted on the same scale, with the y-axis is in nanoseconds and x-axis in sample #. Each zero-crossing was offset to place them on the same plot for better visualization. Using this data, Figure 54 was constructed to demonstrate how the standard deviation in TDC measurements is linearly proportional to zero-crossing location.

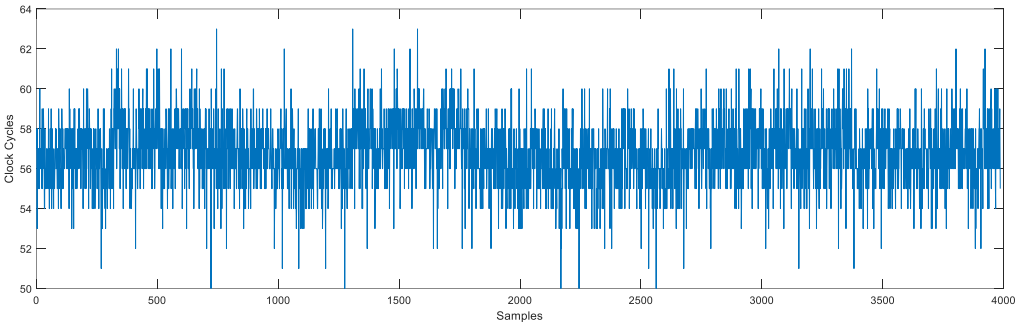

***Figure 52**: Phase measurements plotted one after another for the same zero-crossing location. The phase uncertainty is visible.*

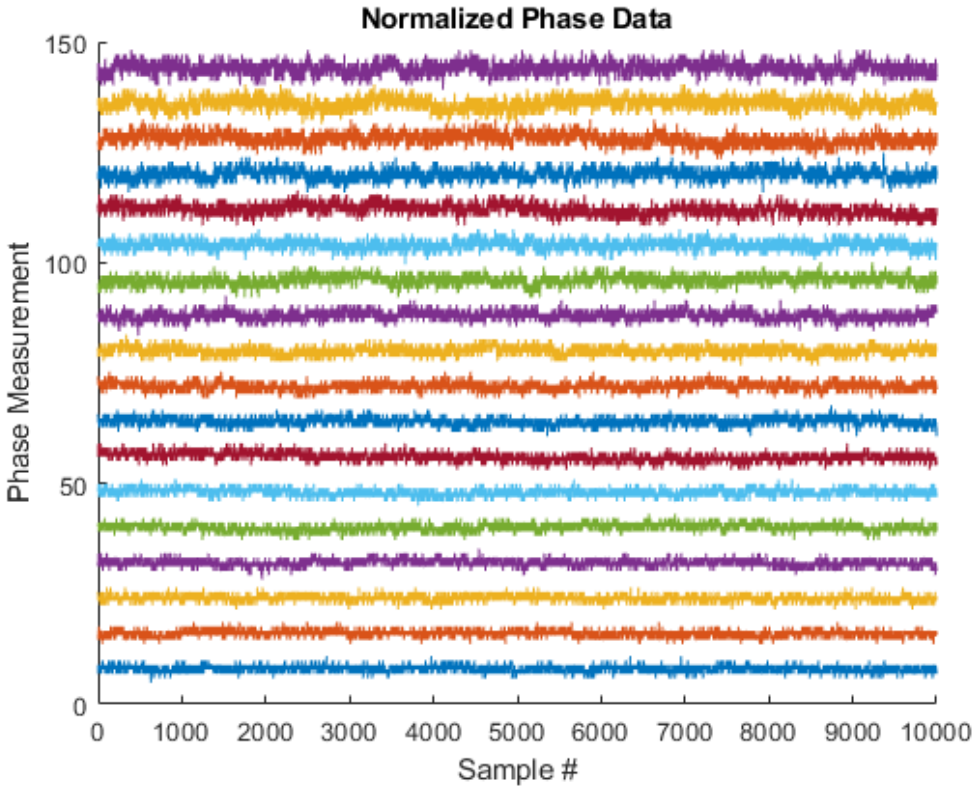

***Figure 53**: Multiple phase measurements plotted for multiple zero crossing locations. The further away (positive Y-axis) in time the measurement is taken, the more uncertainty exists in the measurement.*

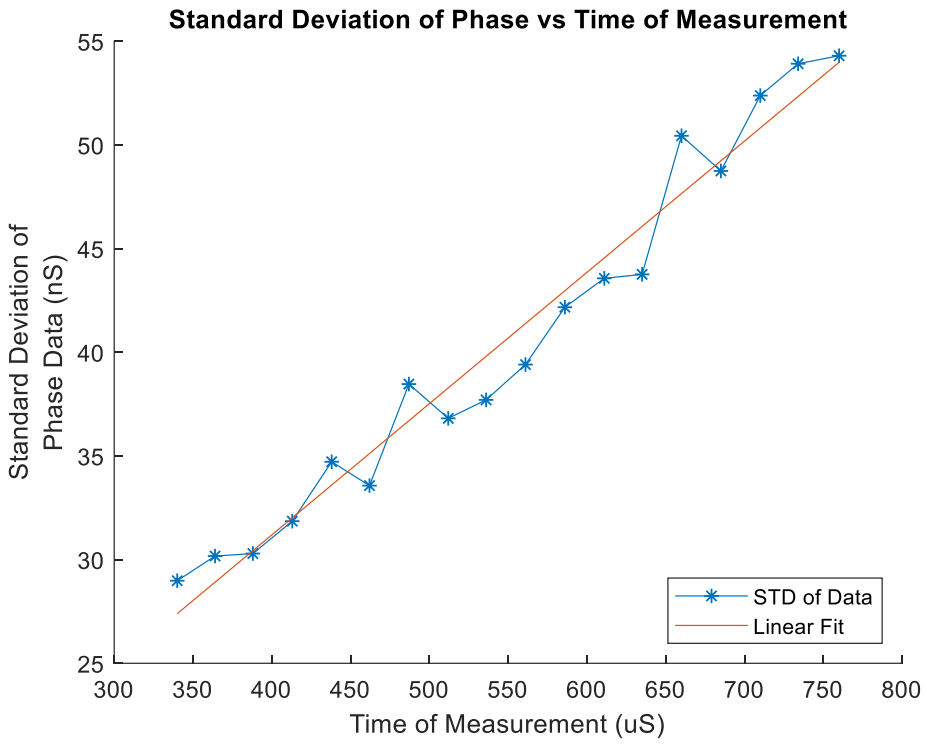

***Figure 54**: Data from multiple instances of zero-crossings are plotted for their variance against time of occurrence. Plot demonstrates the clear linear pattern that exists.*

The clock signal frequency deviation, and resulting phase accumulation is then linearly related to time of measurement (Figure 54). Thus, later detections of phase show more error than earlier detections. In this case, an explanation for this phenomenon is that the MCU (Microcontroller) clock has had more time to accumulate phase errors and the variance in measurement increases. This meant that taking the zero-crossing measurement sooner was better than later. These measurements expose a fair bit of phase noise, the solution to this was to reduce the uncertainty in frequency generation, by using a phase locked loop in conjunction with a crystal oscillator. This improved the few parts per thousand (PPT) deviation in frequency generation, to only a few parts per million (PPM) which dramatically improved uncertainty in signal recovery. With persistence on, we can see how the phase certainty of the zero-crossing trigger is vastly improved with an 8MHz crystal oscillator in Figure 55.

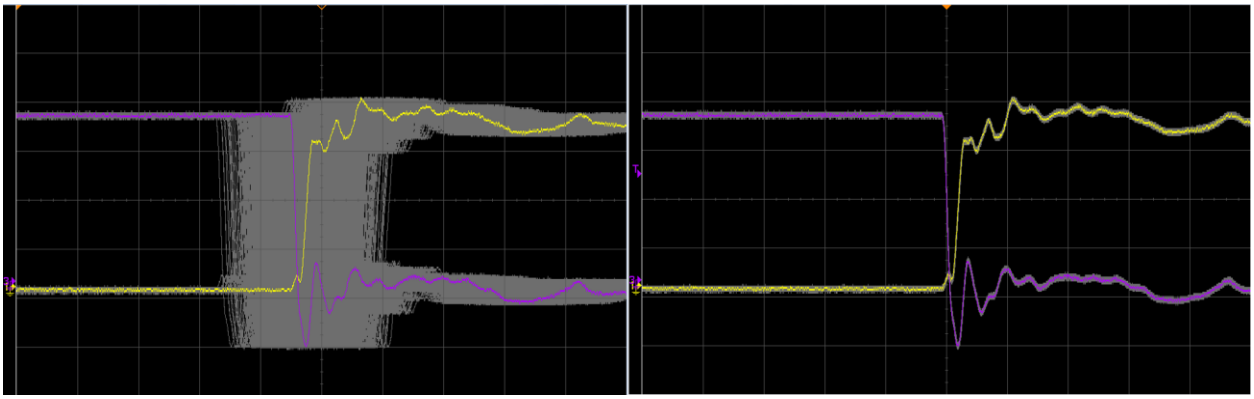

***Figure 55**: Demonstration of phase uncertainty. (Left no crystal oscillator) (right with 8MHz crystal oscillator in PLL with TDC clock)*

C. Pulse Repetition Rate

Pulse repetition rate determines the maximum sampling frequency of the sensor. A high sampling rate is desirable to receive high resolution data. The pulse repetition rate is limited by transmitter transducer ring-down time, since the transmitter and reciever roles are swapped after each ultrasonic pulse. Letting the transmitter ring out prevents interference between the previous transmitted pulse phase and the next received pulse phase, though this ring out time is long, on the order of 2ms. This means the highest sampling frequency achievable by this sensor is roughly 500 samples per second, though this frequency is more than adequate for sampling past Nyquist for breathing signals. As an attempt to increase this sampling frequency, anti-phase pulses were added after each transmit sequence, where a few extra square-wave cycles, 180 degrees shifted from the driving pulse, were meant to actively cancel the ring out, seen in Figure 56 / Figure 57.

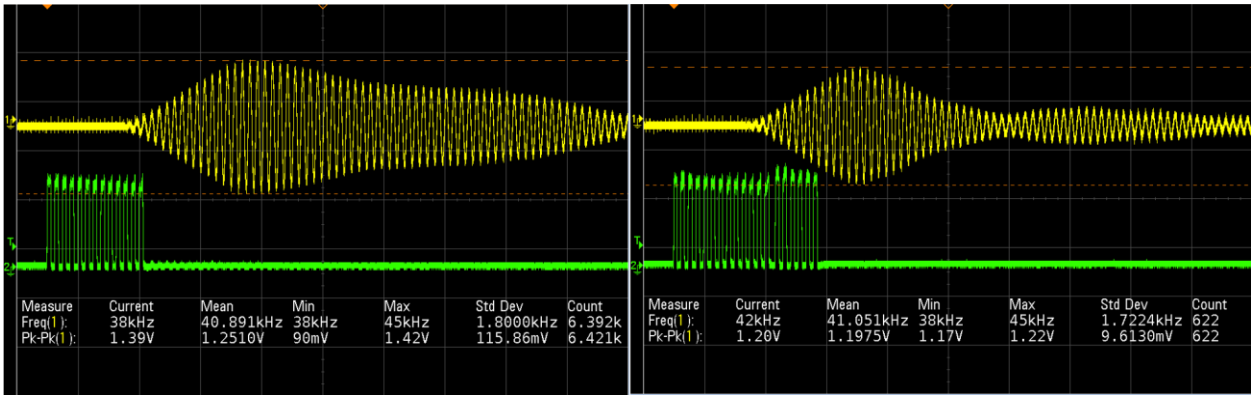

***Figure 56**: Full Length Pulse (Left), Reduced pulse with anti-phase driving signal (Right)*

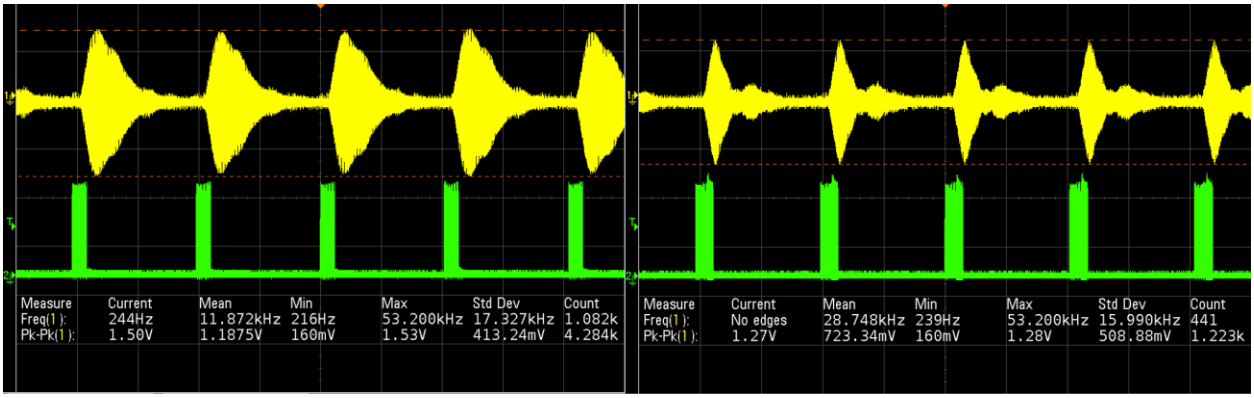

***Figure 57**: Regular pulse train (Left), antiphase supplemented pulse train (Right)*

Though anti-phase pulsing did reduce the total power of the signal at the reciever, unfortunately, it did not have a positive effect on ringdown time at the receiver, thus it may be possible that the transmitter is also unaffected in terms of settling time. Considering the transmitter is the device in question, seeing the effect on this transducer directly would be more effective in measuring the effect of anti-phase pulsing, though this would likely require a different measurement solution, such as an optical one, as letting the sensor terminals float at the gate of a buffer amplifier to measure the voltage as a function of displacement, would also alter the ringdown effects. Though I suspect active cancellation may be required to reduce ringdown. Sampling frequency is adequate for the application; therefore, this can be benched for future research.

D. Temperature Cancellation

Breathing signals contain a fair bit of humidity and temperature, which alter the speed of sound. This alteration of the speed of sound obscures fluid flow measurements when using time-of-flight. Internal body temperature would be the maximum temperature expected to be ejected from the lungs, and while humidity is a concern, its effects are far less noticeable than temperature, though they may account for discrepancies in the expected linear relationship between time of flight and temperature.

An AD590JF temperature sensor was added to the inside of the tube containing the ultrasonic sensor. Hot air was blown into the tube to heat it, and the ends were capped to allow the temperature to gradually decay. During the time the temperature sensor was capturing data (Figure 58), the ultrasonic sensor was capturing up-and downstream measurements for time of flight. The phase difference captured was plotted against temperature and a linear relationship emerged, as shown in Figure 59.

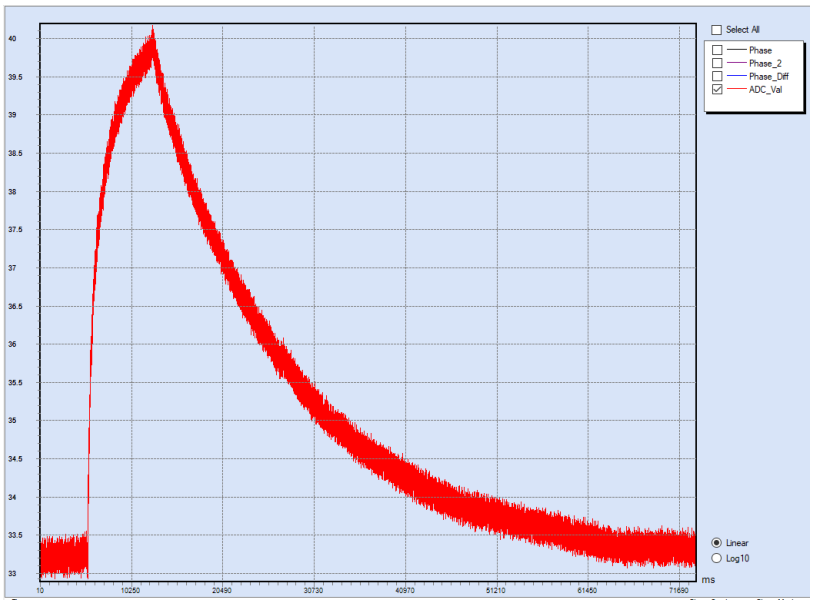

***Figure 58**: Temperature sensor step response*

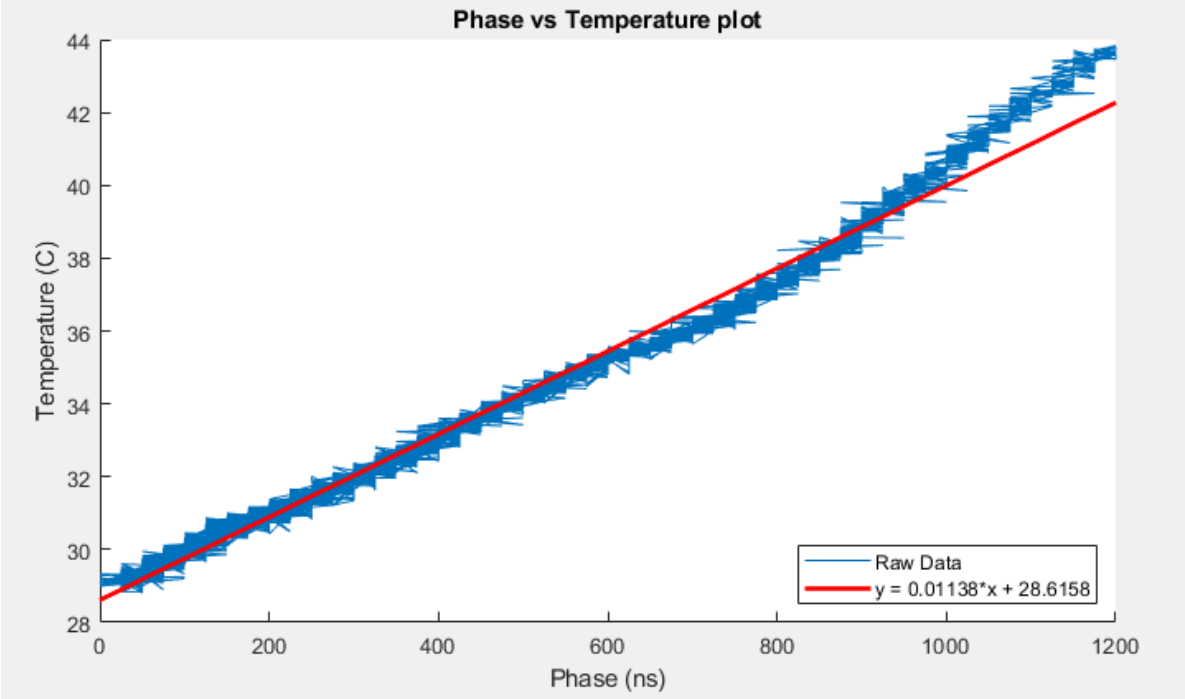

***Figure 59**: Relationship between measured phase shift, (phase accumulation due to speed of sound changes) and temperature.*

The bi-directional effect of temperature cancellation is very powerful, even during steady state, the variations in speed of sound are staggering. Figure 60 shows how much single sided phase measurements vary in time with no fluid flow in the channel, and how their difference shows a net zero flow.

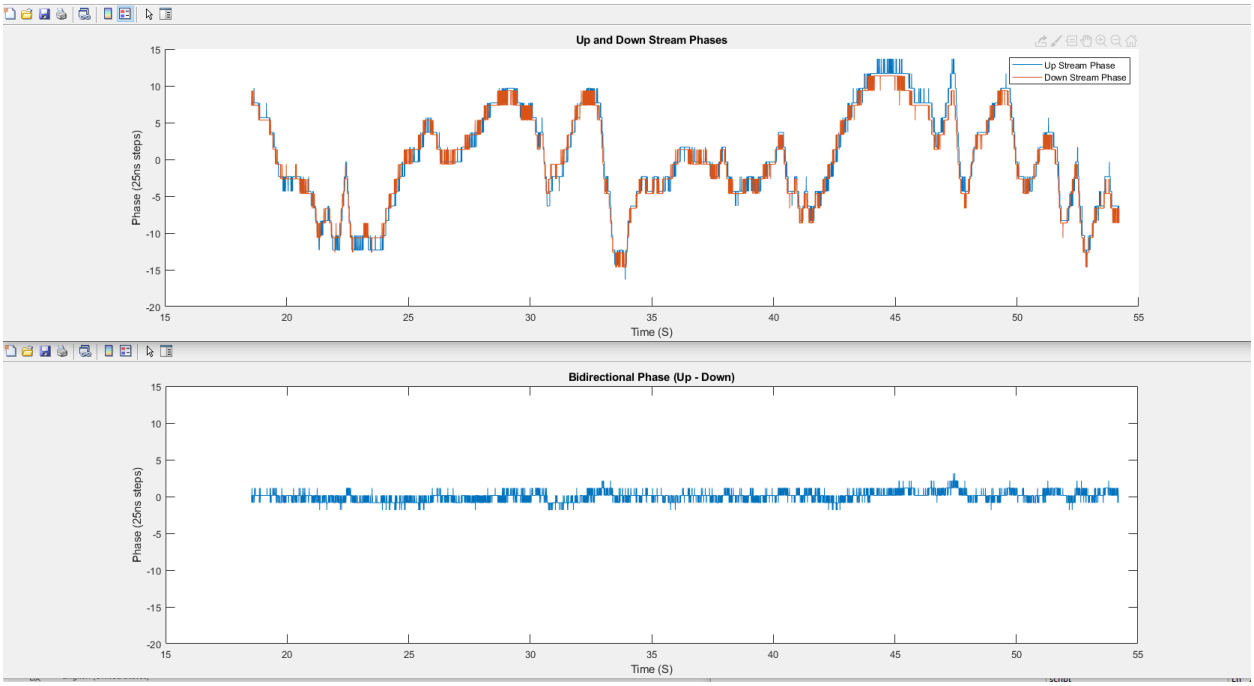

***Figure 60**: Demonstration of the steady state changes in time-of-flight despite no induced drift velocity, and demonstration of the effect of temperature cancellation when taking their difference.*

E. Geometry

As mentioned in chapter 3, the geometry of the sensor was of great consideration. Multiple geometries were investigated and tested for their sensitivity, linearity, and size. The results of the tests on the geometries shown in Figure 61. are shown in Figure 62.

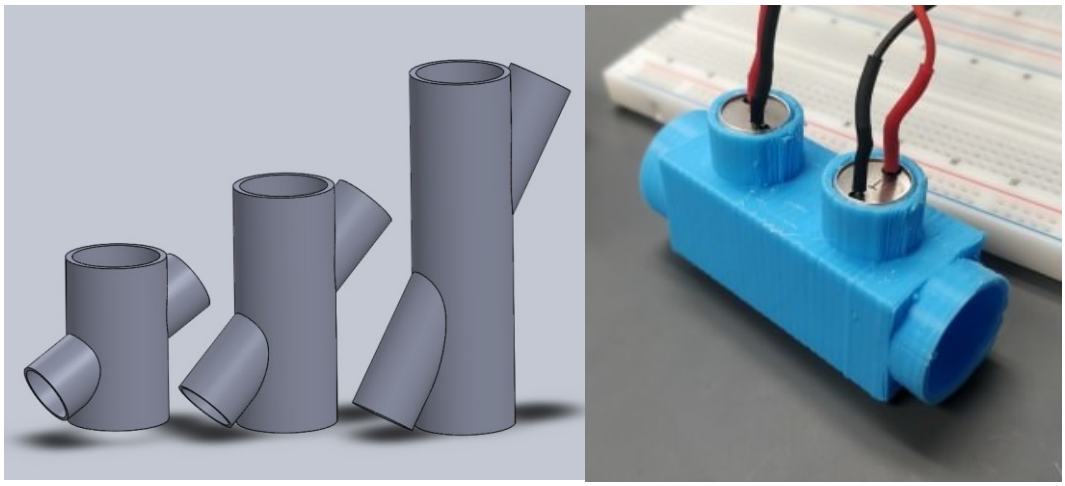

***Figure 61**: Various geometries of ultrasonic sensor tested. Left to Right (30 degree, 45, degree, 60 degree, Box)*

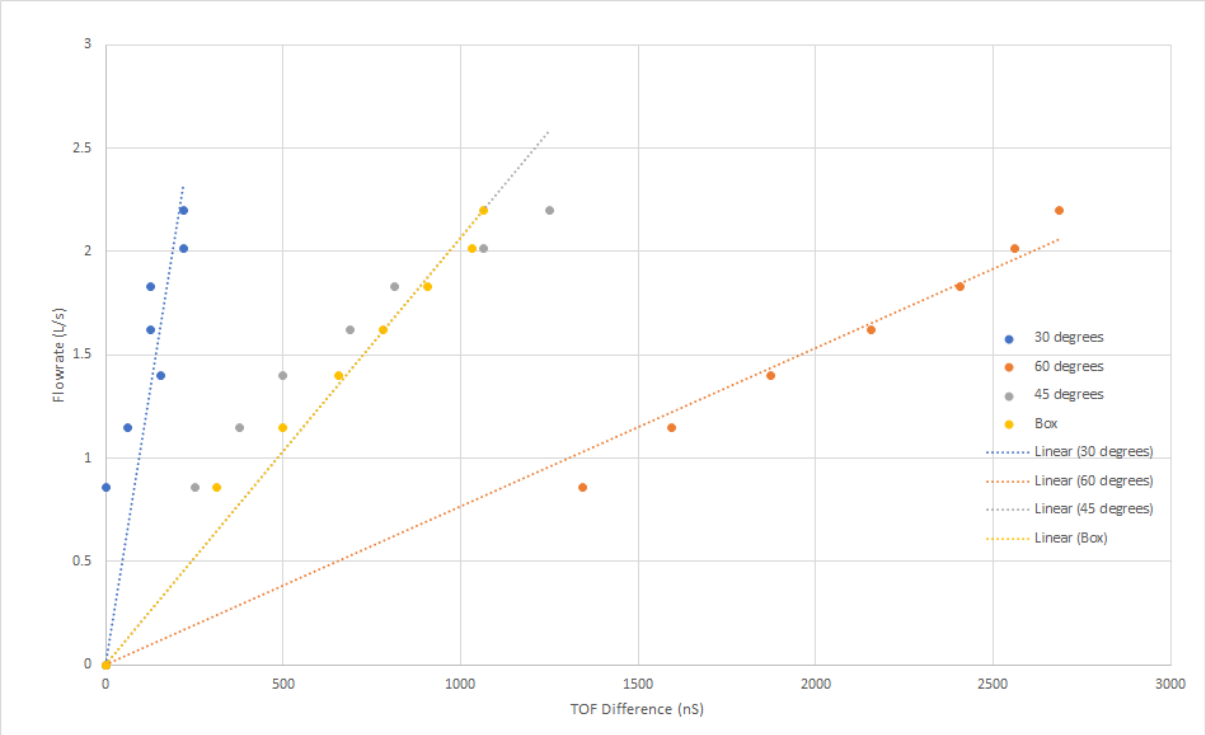

***Figure 62**: Results from testing the linearity, resolution and range of flow as tube angle changes. Results were taken using a signle sided measurement and no crystal oscillator.*

These geometries all show a relatively linear relationship between flow and time of flight. These tests were done on one of the earlier prototypes that do not take advantage of the double sided (bi-directional) measurement or the phase locked loop clock stabilization, which is what likely contributes to the noise seen in these measurements. What is surprising is that the square tube also showed a linear relationship between flow and time of flight, with a linear regression almost identical to the 45-degree angled tube, which may give an avenue for a new geometry not yet seen in literature.

III. LIA Components

A. Amplifier

To verify functionality of the amplifier and to debug potential issues with saturation, stability and gain, the amplifier outputs were routed off chip for inspection. The signals shown in Figure 63 highlight the operation of the amplifier when subjected to an input signal at various frequencies and phases, pre-mixed with the FOT signals.

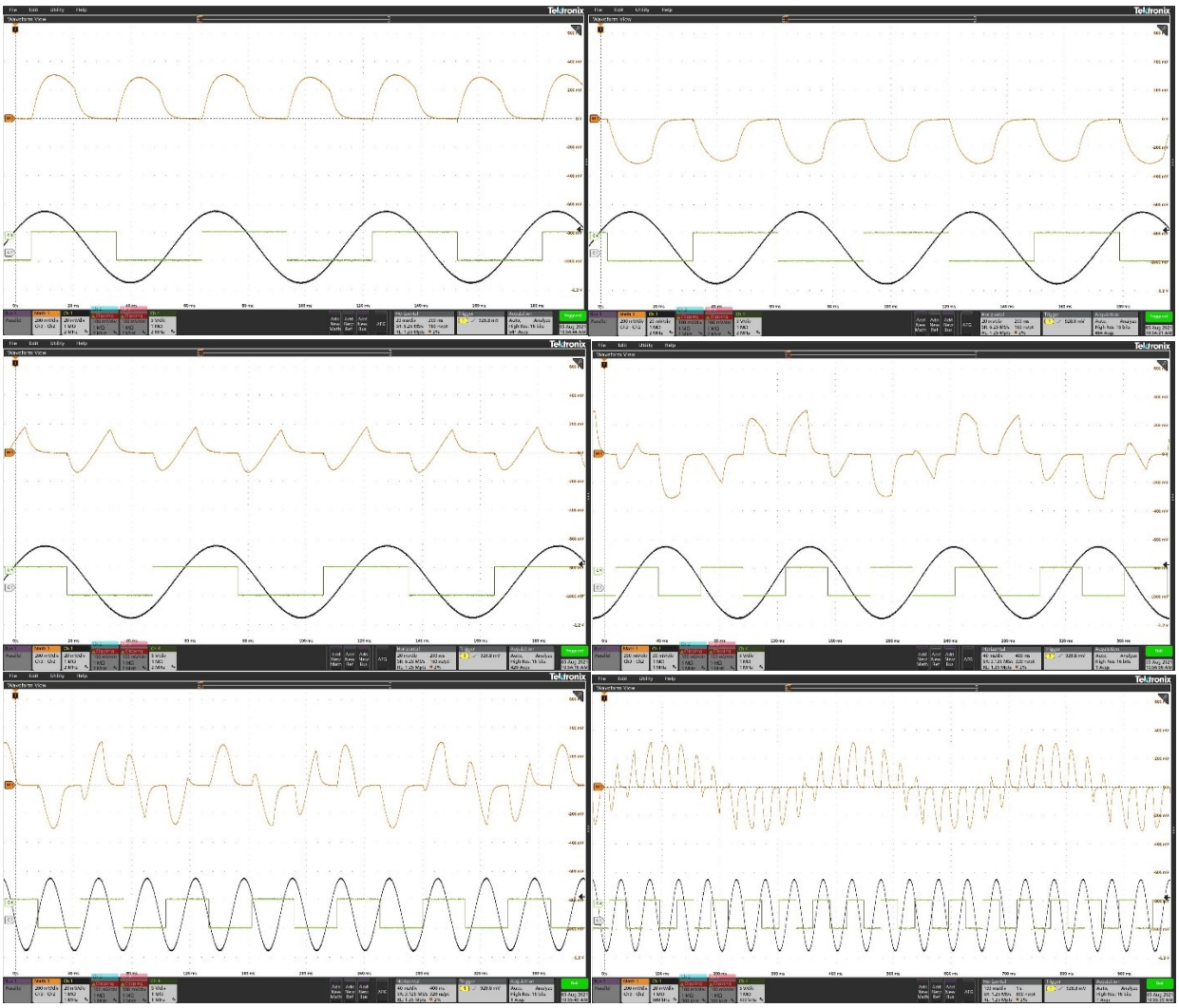

***Figure 63**: Demonstration of mixing occurring before the Low Pass Filter. (black – input)(green - demodulation) (yellow – output)*

(Top Left)	*Input is frequency matched and in-phase (~0°) relative to demodulation signal*
(Top Right)	*Input is frequency matched and in-phase (~180°) relative to demodulation signal*
(Mid. Left)	*Input is frequnecy matched and out-of-phase (~90°) relative to demodulation signal*
(Mid. Right)	*Input has large (~10Hz) frequency deviation relative to demodulation signal*
(Bot. Left)	*Input has small (~1Hz) frequency deviation relative to demodulation signal*
(Bot Right)	*Input has a very small (~0.1Hz) frequency deviation relative to demodulation signal*

To understand the effectiveness of flicker noise suppression in the amplifier, the chopper stabilization was tested. Using the testbench PCB in Chatper 4, a PSoC 6 (Programmable System on Chip) and its built in scanning SAR ADC (Successive Apprimation Register Analog to Digital Converter), four channels; Amplifier Input Positive (AI+), Amplifier Input Negative (AI-), Amplifier Output Positive (AO+) and Amplifier Output Negative (AO-) were sampled. The ADC was averaged over 128 samples for an effective 15 bit resolution, with 200Hz sampling rate. Both AI+ and AI- were shorted together and grounded through a capacitive coupling to supress as much noise at the input as possible to get a good measurement of the noise floor. Figure 64 shows the resultrs of this test.

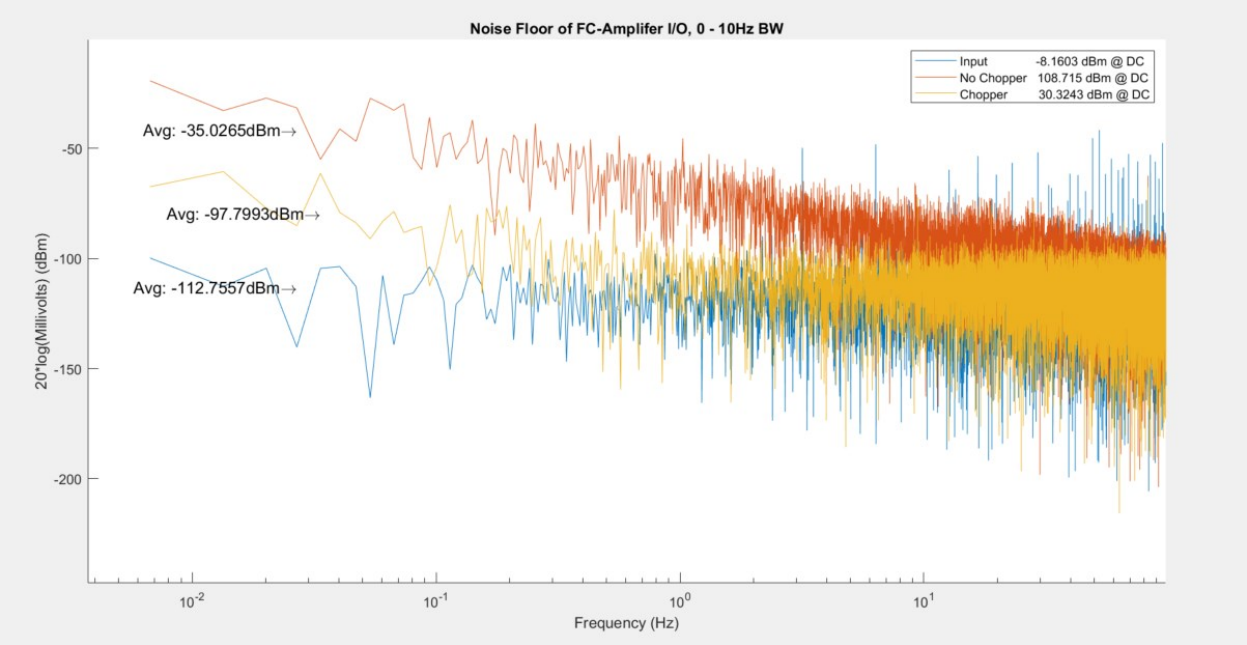

***Figure 64**: Effect of chopper stabilization on noise floor characteristics for the folded-cascode amplifier.*

The input has a approximate noise floor at -112dBm, and is flat white noise. With the choppers off, the noise floor of the output was measured, and a prominent pink noise emerged, roughly +75dBm above the input, but when the choppers are engaged, the noise drops 60dBm, closing the gap to the input noise floor to only an average of 15dBm over 10Hz bandwidth, showing that the choppers are highly effective at reducing noise around, and at DC.

B. Low Pass Filter

The low pass filter bandwidth was tested using a function generator. The input was set to a 1Vpp sine wave, at 900mV DC offset. The frequency was swept from 0.1Hz up to 50Hz. The peak-to-peak voltage of the output signals as a ratio of the input gave the characteristic plot in Figure 67. The Simulated frequency response is shown in Figure 65, while Tektronix oscilloscope offered a chirp signal bode plot in Figure 66.

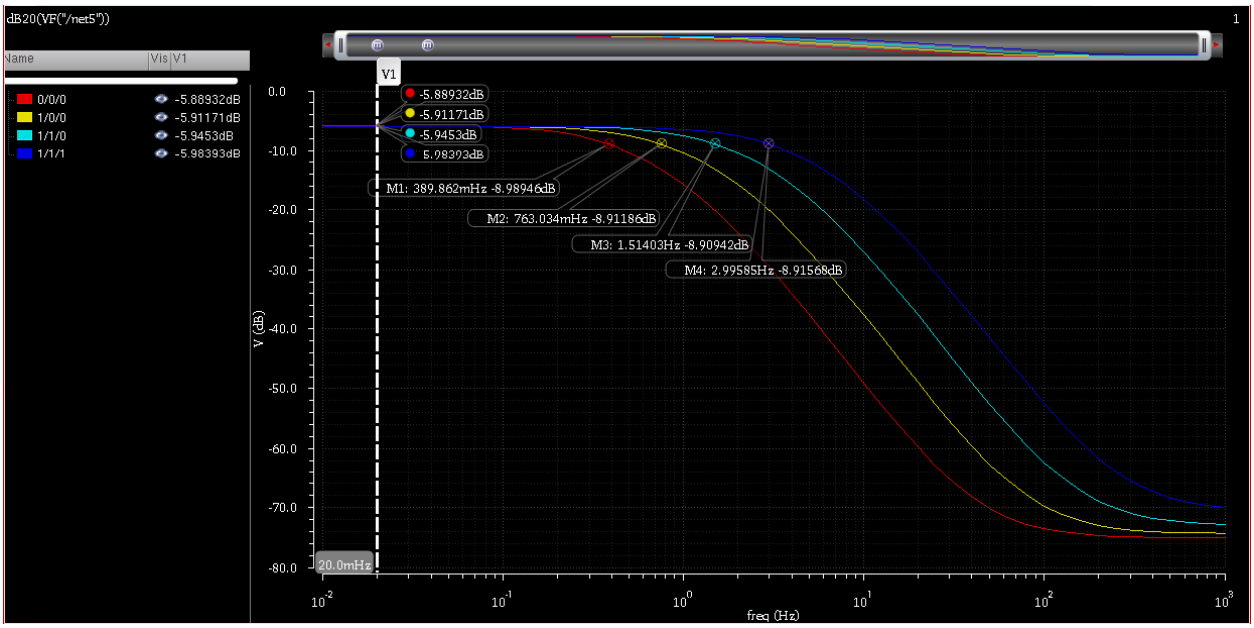

***Figure 65**: Simulated low pass filter bandwidths based on bandwidth setting.*

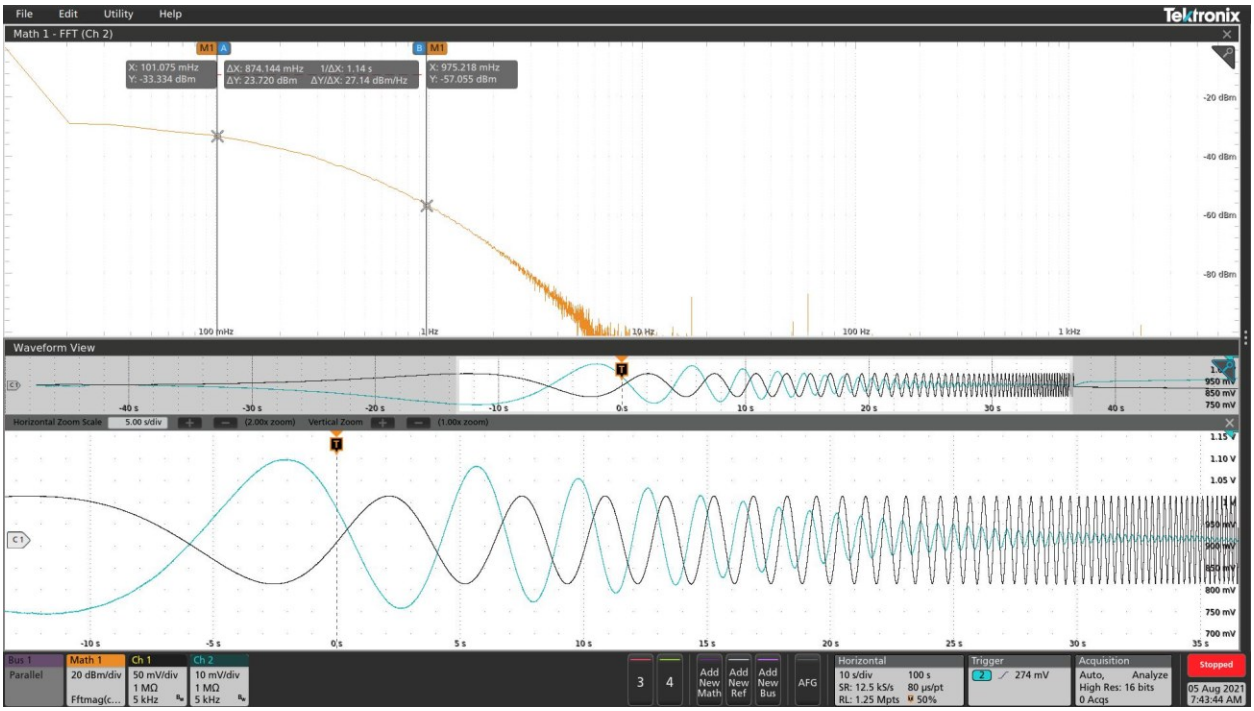

***Figure 66**: One example of the filter response for the low pass filter using a chirp signal.*

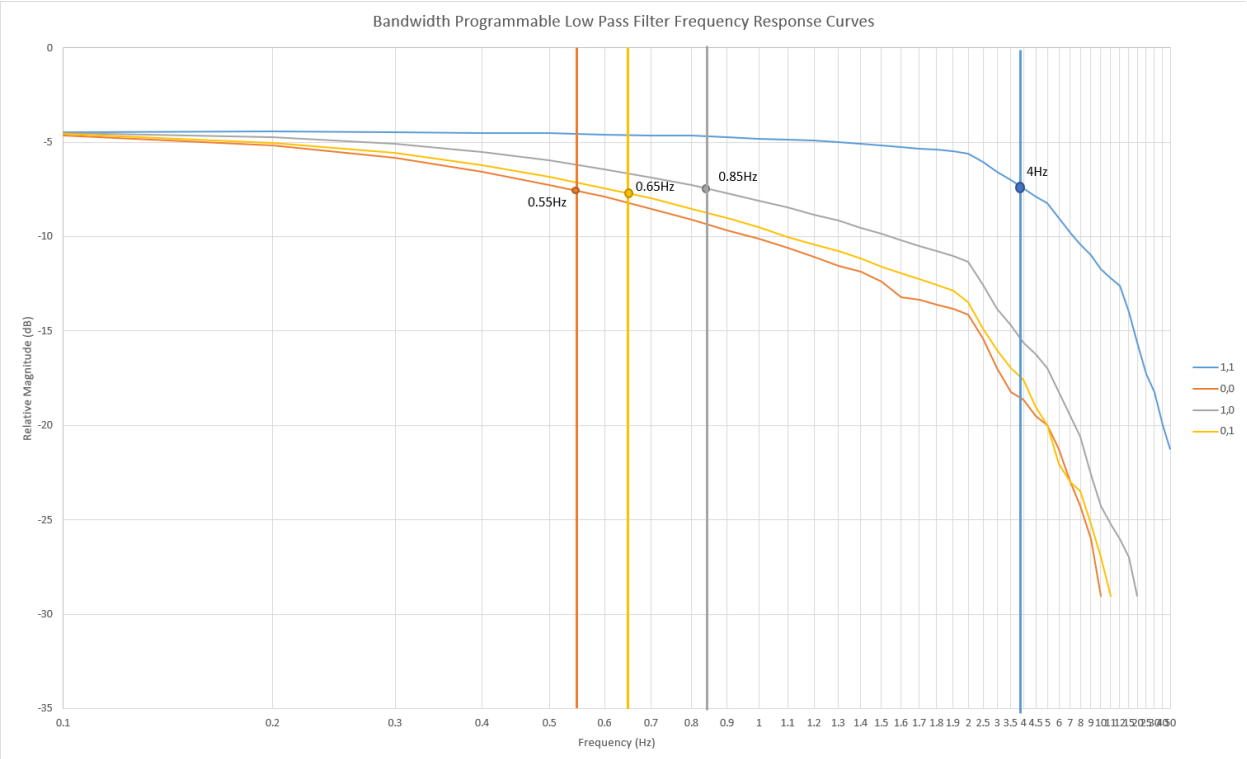

***Figure 67**: Results from multiple bandwidth settings for the low-pass filter. (Legend refers to the bandwidth pragramming bits, [BW0, BW1])*

The low pass filter required a sub-1Hz cutoff frequency to reject the lowest expected FOT frequency. Despite having ~300x capacitive gain, the filter could still occupy a larger area than intended if the capacitance and resistances in the filter were not weighted accordingly. The RC time constant should be as large as possible for a given area, i.e. the area should be optimum for the given resistor and capacitor value. The RC time constant can be written as:

$$\tau = RC \tag{69}$$

Where resistance and capacitance (R, C) can be related to their occupied area (A_R, A_C) by the resistance per unit area R_A and capacitance per unit area C_A of the CMOS components:

$$C = A_C \cdot C_A \qquad R = A_R \cdot R_A \tag{70}$$

The total area that any one stage of the filter would consume would just be the sum of these two areas:

$$A_T = A_R + A_C = \frac{C}{C_A} + \frac{R}{R_A} \tag{71}$$

Now we have two relationships for R and C, we want to optimize τ to be as large as possible, and total area A_T to be as small as possible. Say we fix τ at a value that gives us the sub 1Hz cutoff desired. Making this a constant and substituting either R or C as simply a ratio of the other value, (lets pick R in this case), we get the relationship:

$$A_T = \frac{C}{C_A} + \frac{\tau}{C \cdot R_A} \tag{72}$$

This relationship has an optimum value for area. By taking the derivative of capacitance with respect to area and setting that derivative to zero, we get:

$$\frac{dA_T}{dC} = \frac{1}{C_A} - \frac{\tau}{R_A}\frac{1}{C^2} = 0 \tag{73}$$

Solving for C, and doing the same derivation for R:

$$\frac{1}{C_A} = \frac{\tau}{R_A}\cdot\frac{1}{C^2} \qquad \tau \cdot C_A R_A = C^2 \qquad C = \pm\sqrt{\tau \cdot C_A R_A}, \; R = \pm\sqrt{\tau \cdot R_A C_A} \tag{74}$$

What this tells us is, (taking only the positive real root of C and R), resistance and capacitance do not depend on one-another, only on the ratio of their value per unit area and the time constant chosen. This means that even with a capacitive gain, i.e., the capacitance looks larger than it is, the

optimum ratio of area they consume doesn't change, only the value of total area. It just so happens that the optimum choice that yields the lowest area footprint for a given τ is when $A_R = A_C$. This is shown by substituting R and C for their optimal values and merging their per unit areas into the square roots.

$$A_T = A_R + A_C = \left(\frac{\tau \cdot C_{A\square}}{R_{A\square}}\right)^{\frac{1}{2}} + \left(\frac{\tau \cdot R_{A\square}}{C_{A\square}}\right)^{\frac{1}{2}} \quad 75$$

$$A_T = A_R + A_C = \left(\frac{\tau \cdot C_{A\square}}{R_{A\square} \cdot C_{A\square}}\right)^{\frac{1}{2}} + \left(\frac{\tau \cdot R_{A\square}}{C_{A\square} \cdot R_{A\square}}\right)^{\frac{1}{2}} \quad 76$$

$$A_T = A_R + A_C = \left(\frac{\tau}{R_{A\square} \cdot C_{A\square}}\right)^{\frac{1}{2}} + \left(\frac{\tau}{R_{A\square} \cdot C_{A\square}}\right)^{\frac{1}{2}} \quad 77$$

$$\therefore A_R = A_C \quad , \quad A_T = 2 \cdot \left(\frac{\tau}{R_{A\square} \cdot C_{A\square}}\right)^{\frac{1}{2}} \quad 78$$

This relationship holds provided the assumption that capacitance and resistance are linearly related to their area through their per unit area values. This relationship can determine what optimum areas can be taken for a given desired time constant, as in this case, or in the case where space is even more limited, what optimum size of time constant can be achieved given the total area available. Figure 68 shows the total areas on chip were matched based on their per unit areas. The Resistors packed slightly better than the capacitors, as the capacitors needed extra space between them to allow for matching and routing of the switched banks. In hindsight, further optimization could have been done based on the effective scaling factors for per unit areas on the capacitors.

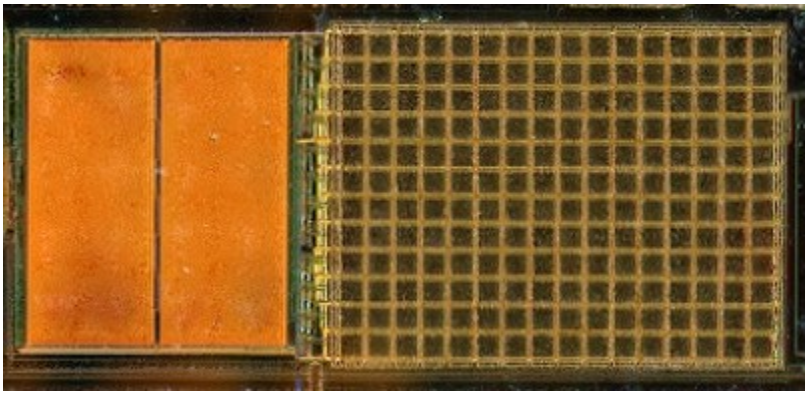

Figure 68*: Microscope image of the capacitor banks (Right) and resistors (Left). Entire image contains 4 filter stages.*

C. Synchronous Waveform Generation

A powerful aspect of the lock in amplifier is the high quality-factor effective bandpass filtering that can be done. The quality factor is only limited by the low pass filtering, which can be further augmented by ADC sampling and averaging. Though, this power is lost if the selection or generation of frequency is poor. Thus, the need for maintaining a phase lock between the generation and stimulation waveforms is a must for producing accurate results. The system level diagram that includes the synchronous generation of FOT and demodulation waveforms, along with how those signals propagate through the system at a high level is shown in Figure 69.

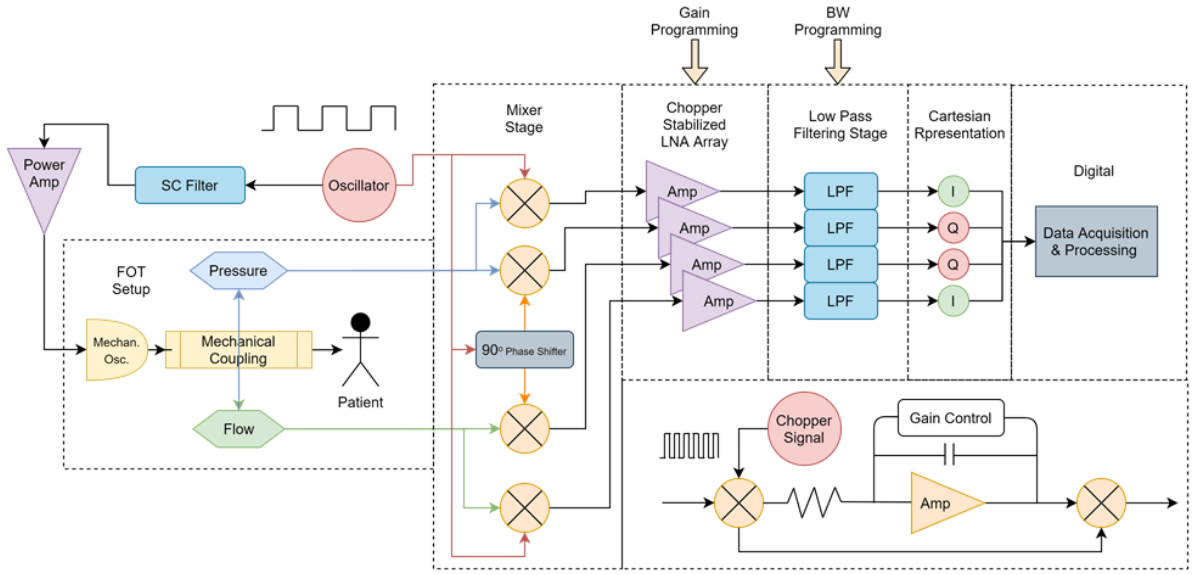

***Figure 69**: High level system diagram showingf the full signal paths from waveform generation, to capture and processing.*

To generate synchronous waveforms, an 8-bit register with timer interrupts on an ATMega328p chip was used. These interrupts occur at the $F\square OSC\square$ frequency. The interrupt routine then toggles the LSB of the 8-bit register. The CLK signal for the 4-phase generator (which creates the demodulation signals) is tapped at the 5th bit in the register. The stimulation waveform needs to be 4x lower frequency, so the 7th bit is tapped for this. The CLK signal goes directly to the chip, while the FOT signal gets buffered and passed through an 8th order switched capacitor filter to generate the stimulation waveform. The switch capacitor filter requires a clock signal that is 100x the cutoff frequency, therefore $F\square OSC\square$ is fed to the SC filter to drive it. The signal is then cleaned up with

passive filtering to ensure no clock-feedthrough, and send to an amplifier to drive the speaker. The CLK, ISR, FOT and F_{OSC} waveforms and their relationships are shown in Figure 70.

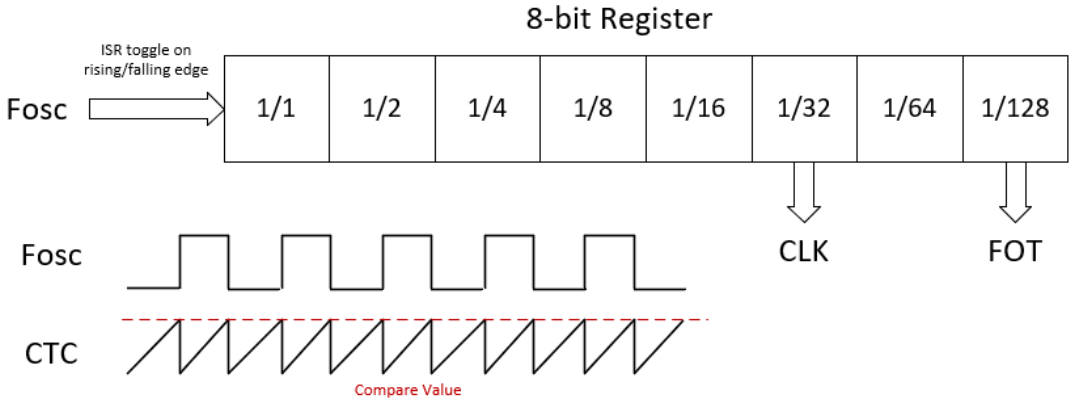

***Figure 70**: Relationship between clock generation signals, FOT signals and filtering clocks for the SC filter.*

Chapter 6 : DISCUSSION

In this chapter, I summarize the original research and results presented in this dissertation, discuss the original contributions of the research, and suggest future directions for continuation of the research.

I. Summary

A. Synchronous Demodulation

In Chapter 4, a novel analog lock in amplifier is designed to leverage small area consumption and power consumption of low-power CMOS devices, while also gaining the benefit of the high-

quality factor effective bandpass filtering and phase sensitive detection of the synchronous demodulation principle. Traditional methods for phase and amplitude extraction of FOT waves in both pressure and flow are done using a sliding window FFT, or Short Time Fourier Transform (STFT). The STFT relies on a precise selection and generation of the frequency used in FOT, any slight deviation in selection or generation causes degradation in SNR. Additionally, the data is captured and processed in the digital domain which introduces quantization noise and requires a relatively high degree of power to accomplish the FFT correlation techniques on an MCU. In a battery powered device like a portable ventilator, this would prove undesirable. The lock-in-amplifier is a powerful tool for determining the phase and amplitude of a very precise band of a signals spectrum and can be done in the analog domain. Proper selection and design can reduce the power requirements drastically. The lock in amplifier is designed in CMOS 0.18um technology, leveraging a passive mixer front end to perform the demodulation operation and to extend the usable linear range of sensor signals, while introducing less noise and consuming less power than its gilbert cell counterpart. The signals are then amplified and filtered through a folded cascode amplifier with added chopper stabilization for increased noise suppression around DC, then heavily filtered by a redesigned, floating ground, active capacitor multiplier. The capacitive multiplier structure, in combination with passive resistors, provides a sub 1Hz passband for high-effective quality-factor bandpass filtering around the FOT frequency after demodulation to DC. The output signals are sampled and averaged for even greater quality factors. The demodulation signals and FOT stimuli are derived from the same source which gives the synchronous demodulation scheme its name, and utility as an incredibly sensitive phase detection device. Four channels were designed and fabricated on chip to provide an in-phase and quadrature measurement for both pressure and flow. FOT signals were simulated using a function generator while in-phase and quadrature correlation factor measurements were taken on two channels to measure sensitivity to amplitude and phase variations and showed a high degree of linearity in these measurements.

B. Ultrasonic Flow Meter

Chapter 3 delves into the novel design of an ultrasonic flow metering device that competes in linearity, sampling rate, and resolution with a typical pneumotachograph device. Pneumotachographs introduce an unwanted resistance in the path of breathing and thus mechanical

loading that works against delivering airflow to the user of a ventilation device which may also obscure oscillometric measurements. The ultrasonic based flow meter removes the need for this resistance in the path of breathing and changes the measurement from requiring expensive vacuum sealed microelectromechanical integrated circuits to using inexpensive piezoelectric actuators. The sensor platform is designed using a mixed signal programmable system on chip (PSoC) to handle the digital signal waveform generation, while capturing and processing the analog signals. The sensor utilizes a zero-crossing detection algorithm and time to digital conversion (TDC) techniques to determine the time of flight of ultrasonic waves across the fluid flow medium. The time difference in up and down stream phase measurements yields a speed-of-sound invariant measurement which effectively cancels out effects of temperature, humidity and density of the fluid when determining fluid drift velocity. The sensor data is then augmented by an offline least mean square (LMS) algorithm and shows a high degree of linearity and resolution when compared to a standard pneumotachograph.

III. Future Directions

1. The resolution of flow captured by the ultrasonic sensor can measure respiratory events, flow limitations, volume, etc. However, the TDC used is only a portion of the potential that can be explored. Even greater resolutions are possible, though increasing the TDC to the gigahertz range would introduce further challenges, and it may be best done on a custom IC.
2. In my research I had found a time to voltage principle for measuring time of flight, this would be valuable for merging the lock in amplifier and ultrasonic sensor without the need for a DAC between them.
3. An additional technique, known as the wave-tube technique has been used to calibrate and measure woodwind and brass instruments to determine their impedance profiles. This technique applied to respiratory system would essentially use the tube itself as the pneumotachographs impedance. By attaching an unknown impedance (breathing patient) to the known and calibrated impedance (mechanical coupling to airways), one could use the phase sensitive detection of the lock in amplifier and mathematical modelling to determine the impedance of the airways. This has a threefold benefit, the effective flow

measurement does not depend on an intrusive resistive element, like the ultrasonic sensor accomplished. It can take two pressure signals as input to the lock in amplifier, thus the gain and scaling of the input signals are similar, and the power of FOT can be lowered even farther than that of the measurement requiring flow, as SNR for pressure is already considerably higher than flow.

4. Knowing the resonant frequency of the airways has been shown to give information about the impedance of the airways, it would be interesting to explore the resonant properties of the airways to lower FOT power further.
5. It would be valuable to collect data on patients with respiratory disorders and those without, using both a traditional setup and the LIA. Compare the absolute measurements and sensitivity of the devices while lowering FOT power so see where the limit of detection of respiratory disorders is for both.

REFERENCES

[1] N. M. Punjabi, "The Epidemiology of Adult Obstructive Sleep Apnea," *Proceedings of the American Thoracic Society*, vol. 5, no. 2, pp. 136–143, Feb. 2008, doi: 10.1513/pats.200709-155MG.

[2] L. J. Akinbami, J. E. Moorman, and X. Liu, "Asthma prevalence, health care use, and mortality: United States, 2005-2009," *Natl Health Stat Report*, no. 32, pp. 1–14, Jan. 2011.

[3] D. M. Mannino, "COPD: Epidemiology, Prevalence, Morbidity and Mortality, and Disease Heterogeneity," *Chest*, vol. 121, no. 5, pp. 121S-126S, May 2002, doi: 10.1378/chest.121.5_suppl.121S.

[4] D. P. White, "Sleep Apnea," *Proceedings of the American Thoracic Society*, vol. 3, no. 1, pp. 124–128, Mar. 2006, doi: 10.1513/pats.200510-116JH.

[5] S. Lehman, N. A. Antic, C. Thompson, P. G. Catcheside, J. Mercer, and R. D. McEvoy, "Central Sleep Apnea on Commencement of Continuous Positive Airway Pressure in Patients With a Primary Diagnosis of Obstructive Sleep Apnea-Hypopnea," *J Clin Sleep Med*, vol. 3, no. 5, pp. 462–466, Aug. 2007.

[6] C. O. Ribeiro, A. C. Faria, A. J. Lopes, and P. L. De Melo, "Forced oscillation technique for early detection of the effects of smoking and COPD: contribution of fractional-order modeling," *COPD*, vol. Volume 13, pp. 3281–3295, Oct. 2018, doi: 10.2147/COPD.S173686.

[7] A. S. LaPrad and K. R. Lutchen, "Respiratory impedance measurements for assessment of lung mechanics: Focus on asthma," *Respiratory Physiology & Neurobiology*, vol. 163, no. 1–3, pp. 64–73, Nov. 2008, doi: 10.1016/j.resp.2008.04.015.

[8] C. Torregiani *et al.*, "Monitoring respiratory mechanics by oscillometry in COVID-19 patients receiving non-invasive respiratory support," *PLOS ONE*, vol. 17, no. 3, p. e0265202, Mar. 2022, doi: 10.1371/journal.pone.0265202.

[9] H. Hanafi, K. El-Sankary, and G. N. Maksym, "Are Variations of Impedance in Time Contributing to Frequency Dependence of Resistance?," in *C108. ADVANCES IN LUNG FUNCTION ASSESSMENT*, in American Thoracic Society International Conference Abstracts. American Thoracic Society, 2016, pp. A6359–A6359. doi: 10.1164/ajrccm-conference.2016.193.1_MeetingAbstracts.A6359.

[10] H. H. Alamdari, K. El-Sankary, and G. N. Maksym, "Time-Varying Respiratory Mechanics as a Novel Mechanism Behind Frequency Dependence of Impedance: A Modeling Approach," *IEEE Transactions on Biomedical Engineering*, vol. 66, no. 9, pp. 2433–2446, Sep. 2019, doi: 10.1109/TBME.2018.2890055.

[11] H. Hanafi Alamdari *et al.*, "Tracking Respiratory Mechanics With Oscillometry: Introduction of Time-Varying Error," *IEEE Sensors Journal*, vol. 19, no. 1, pp. 311–321, Jan. 2019, doi: 10.1109/JSEN.2018.2873184.

[12] A. B. DuBois, A. W. Brody, D. H. Lewis, and B. F. Burgess, “Oscillation Mechanics of Lungs and Chest in Man,” *Journal of Applied Physiology*, vol. 8, no. 6, pp. 587–594, May 1956, doi: 10.1152/jappl.1956.8.6.587.

[13] L. Posada, H. Hanafi, G. Drapeau, and G. N. Maksym, “A Piezoelectric Actuated Airwave Oscillometry Device,” *CMBES Proceedings*, vol. 36, May 2013, Accessed: Jun. 06, 2023. [Online]. Available: https://proceedings.cmbes.ca/index.php/proceedings/article/view/422

[14] H. H. Alamdari *et al.*, “High Frequency-Low Amplitude Oscillometry: Continuous Unobtrusive Monitoring of Respiratory Function on PAP Machines,” *IEEE Transactions on Biomedical Engineering*, vol. 69, no. 7, pp. 2202–2211, Jul. 2022, doi: 10.1109/TBME.2021.3138965.

[15] M. Sinclair *et al.*, “The Beginning of the AI-Enabled Preventative PAP Therapy Era: A First-in-Human Proof of Concept Interventional Study,” *IEEE Transactions on Biomedical Engineering*, pp. 1–12, 2023, doi: 10.1109/TBME.2023.3263379.

[16] J. Turner, *Automotive Sensors*. Momentum Press, 2009.

[17] D.-H. Gao, M. Qin, H.-Y. Chen, and Q.-A. Huang, “A self-packaged thermal flow sensor by CMOS MEMS technology,” in *2004 IEEE SENSORS*, Oct. 2004, pp. 879–883 vol.2. doi: 10.1109/ICSENS.2004.1426311.

[18] N. Mandal, “Respirometers including spirometer, pneumotachograph and peak flow meter,” *Anaesthesia & Intensive Care Medicine*, vol. 7, no. 1, pp. 1–5, Jan. 2006, doi: 10.1383/anes.2006.7.1.1.

[19] J. A. F. Ferreira and A. Petraglia, “Analog integrated lock-in amplifier for optical sensors,” *IEEE Instrumentation & Measurement Magazine*, vol. 20, no. 2, pp. 43–50, Apr. 2017, doi: 10.1109/MIM.2017.7919134.

[20] © 2021 IEEE. Reprinted, with permission, from G. Begin, K. M. Al-Tamimi, H. H. Alamdari, D. C. Roach, M. Schmidt, and K. El-Sankary, “Respiratory Bidirectional Ultrasonic TOF Flow Sensor Resilience to Ambient Temperature Fluctuations,” *IEEE Sensors Journal*, vol. 21, no. 17, pp. 18920–18931, Sep. 2021, doi: 10.1109/JSEN.2021.3088713.

[21] G. Luciano, this link will open in a new window Link to external site, M. Quintel, and J. J. Marini, “‘Less is More’ in mechanical ventilation,” *Intensive Care Medicine*, vol. 46, no. 4, pp. 780–782, Apr. 2020, doi: 10.1007/s00134-020-05981-z.

[22] H. Li *et al.*, “Utah-Stanford Ventilator (Vent4US): Developing a rapidly scalable ventilator for COVID-19 patients with ARDS.” medRxiv, p. 2020.04.18.20070367, Apr. 22, 2020. doi: 10.1101/2020.04.18.20070367.

[23] S. L. Archer, W. W. Sharp, and E. K. Weir, “Differentiating COVID-19 Pneumonia From Acute Respiratory Distress Syndrome and High Altitude Pulmonary Edema,” *Circulation*, vol. 142, no. 2, pp. 101–104, Jul. 2020, doi: 10.1161/CIRCULATIONAHA.120.047915.

[24] T. kien Nguyen, D. H. Mai, A. N. Le, Q. H. Nguyen, C. T. Nguyen, and T. A. Vu, “A review of intraoperative lung-protective mechanical ventilation strategy,” *Trends in Anaesthesia and Critical Care*, vol. 37, pp. 9–17, Apr. 2021, doi: 10.1016/j.tacc.2020.11.001.

[25] N. B. Pride, “Forced oscillation techniques for measuring mechanical properties of the respiratory system.,” *Thorax*, vol. 47, no. 4, pp. 317–320, Apr. 1992.

[26] J. R. Badia *et al.*, “Clinical Application of the Forced Oscillation Technique for CPAP Titration in the Sleep Apnea/Hypopnea Syndrome,” *Am J Respir Crit Care Med*, vol. 160, no. 5, pp. 1550–1554, Nov. 1999, doi: 10.1164/ajrccm.160.5.9902085.

[27] S. D. Herkenrath *et al.*, “Extended evaluation of the efficacy of a proactive forced oscillation technique-based auto-CPAP algorithm,” *Sleep Breath*, vol. 24, no. 3, pp. 825–833, Sep. 2020, doi: 10.1007/s11325-019-01901-8.

[28] C.-L. Wei, C.-F. Lin, and I.-T. Tseng, “A Novel MEMS Respiratory Flow Sensor,” *IEEE Sensors Journal*, vol. 10, no. 1, pp. 16–18, Jan. 2010, doi: 10.1109/JSEN.2009.2035192.

[29] S.-H. Liao, W.-J. Chen, and M. S.-C. Lu, “A CMOS MEMS Capacitive Flow Sensor for Respiratory Monitoring,” *IEEE Sensors Journal*, vol. 13, no. 5, pp. 1401–1402, May 2013, doi: 10.1109/JSEN.2013.2245320.

[30] C.-L. Wei, Y.-C. Lin, T.-A. Chen, R.-Y. Lin, and T.-H. Liu, “Respiration Detection Chip With Integrated Temperature-Insensitive MEMS Sensors and CMOS Signal Processing Circuits,” *IEEE Transactions on Biomedical Circuits and Systems*, vol. 9, no. 1, pp. 105–112, Feb. 2015, doi: 10.1109/TBCAS.2014.2315532.

[31] M.-K. Tsai, T.-A. Chen, H.-Y. Chiu, T.-W. Wu, and C.-L. Wei, “Monolithic Airflow Detection Chip With Automatic DC Offset Calibration,” *IEEE Transactions on Circuits and Systems I: Regular Papers*, vol. 65, no. 1, pp. 107–117, Jan. 2018, doi: 10.1109/TCSI.2017.2715339.

[32] J. Jin and E. Sánchez-Sinencio, “A Home Sleep Apnea Screening Device With Time-Domain Signal Processing and Autonomous Scoring Capability,” *IEEE Transactions on Biomedical Circuits and Systems*, vol. 9, no. 1, pp. 96–104, Feb. 2015, doi: 10.1109/TBCAS.2014.2314301.

[33] D. Li, T. Li, and D. Zhang, “A Monolithic Piezoresistive Pressure-Flow Sensor With Integrated Signal-Conditioning Circuit,” *IEEE Sensors Journal*, vol. 11, no. 9, pp. 2122–2128, Sep. 2011, doi: 10.1109/JSEN.2010.2096536.

[34] M. Mercuri *et al.*, “A Direct Phase-Tracking Doppler Radar Using Wavelet Independent Component Analysis for Non-Contact Respiratory and Heart Rate Monitoring,” *IEEE Transactions on Biomedical Circuits and Systems*, vol. 12, no. 3, pp. 632–643, Jun. 2018, doi: 10.1109/TBCAS.2018.2813013.

[35] A. Sinharay, R. Rakshit, A. Khasnobish, T. Chakravarty, D. Ghosh, and A. Pal, “The Ultrasonic Directional Tidal Breathing Pattern Sensor: Equitable Design Realization Based on Phase Information,” *Sensors*, vol. 17, no. 8, Art. no. 8, Aug. 2017, doi: 10.3390/s17081853.

[36] S. D. Min, D. J. Yoon, S. W. Yoon, Y. H. Yun, and M. Lee, “A study on a non-contacting respiration signal monitoring system using Doppler ultrasound,” *Med Bio Eng Comput*, vol. 45, no. 11, pp. 1113–1119, Nov. 2007, doi: 10.1007/s11517-007-0246-2.

[37] L. Svilainis, “Review of high resolution time of flight estimation techniques for ultrasonic signals,” presented at the 52nd Annual Conference of the British Institute of Non-Destructive Testing 2013, NDT 2013, Sep. 2013.

[38] X. F. Wang and Z. A. Tang, “A novel method for digital ultrasonic time-of-flight measurement,” *Review of Scientific Instruments*, vol. 81, no. 10, p. 105112, Oct. 2010, doi: 10.1063/1.3493046.

[39] D. Grimaldi, “Time-of-flight measurement in ultrasound transducer by means of wavelet networks,” in *Second IEEE International Workshop on Intelligent Data Acquisition and Advanced Computing Systems: Technology and Applications, 2003. Proceedings*, Sep. 2003, pp. 365–370. doi: 10.1109/IDAACS.2003.1249588.

[40] L. Espinosa, J. Bacca, F. Prieto, P. Lasaygues, and L. Brancheriau, “Accuracy on the Time-of-Flight Estimation for Ultrasonic Waves Applied to Non-Destructive Evaluation of Standing Trees: A Comparative Experimental Study,” *Acta Acustica united with Acustica*, vol. 104, no. 3, pp. 429–439, May 2018, doi: 10.3813/AAA.919186.

[41] P. Hauptmann, N. Hoppe, and A. Püttmer, “Application of ultrasonic sensors in the process industry,” *Meas. Sci. Technol.*, vol. 13, no. 8, p. R73, Jul. 2002, doi: 10.1088/0957-0233/13/8/201.

[42] Q. Chen, W. Li, and J. Wu, “Realization of a multipath ultrasonic gas flowmeter based on transit-time technique,” *Ultrasonics*, vol. 54, no. 1, pp. 285–290, Jan. 2014, doi: 10.1016/j.ultras.2013.06.001.

[43] Y. P. Huang, J. S. Wang, K. N. Huang, C. T. Ho, J. D. Huang, and M. S. Young, “Envelope pulsed ultrasonic distance measurement system based upon amplitude modulation and phase modulation,” *Review of Scientific Instruments*, vol. 78, no. 6, p. 065103, Jun. 2007, doi: 10.1063/1.2745238.

[44] A. Carullo and M. Parvis, “An ultrasonic sensor for distance measurement in automotive applications,” *IEEE Sensors J.*, vol. 1, no. 2, p. 143, 2001, doi: 10.1109/JSEN.2001.936931.

[45] K.-Y. Lee, C.-F. Huang, S.-S. Huang, K.-N. Huang, and M.-S. Young, “A High-Resolution Ultrasonic Distance Measurement System Using Vernier Caliper Phase Meter,” *IEEE Transactions on Instrumentation and Measurement*, vol. 61, no. 11, pp. 2924–2931, Nov. 2012, doi: 10.1109/TIM.2012.2203871.

[46] M.-C. Lu, W.-Y. Wang, and C.-Y. Chu, “Image-based distance and area measuring systems,” *IEEE Sensors Journal*, vol. 6, no. 2, pp. 495–503, Apr. 2006, doi: 10.1109/JSEN.2005.858434.

[47] J. R. Gatabi, S. Das, and F. Forouzbakhsh, “The Effect of Amplitude Modulation on the Axial Resolution of Doppler-Based Ultrasonic Topography Measurement,” *IEEE Transactions on Instrumentation and Measurement*, vol. 65, no. 12, pp. 2780–2786, Dec. 2016, doi: 10.1109/TIM.2016.2600999.

[48] J.-D. Huang, C.-K. Lee, C.-S. Yeh, W.-J. Wu, and C.-T. Lin, “High-Precision Ultrasonic Ranging System Platform Based on Peak-Detected Self-Interference Technique,” *IEEE Transactions on Instrumentation and Measurement*, vol. 60, no. 12, pp. 3775–3780, Dec. 2011, doi: 10.1109/TIM.2011.2149391.

[49] R. Carotenuto, M. Merenda, D. Iero, and F. G. D. Corte, “Using ANT Communications for Node Synchronization and Timing in a Wireless Ultrasonic Ranging System,” *IEEE Sensors Letters*, vol. 1, no. 6, pp. 1–4, Dec. 2017, doi: 10.1109/LSENS.2017.2776136.

[50] R. Carotenuto, M. Merenda, D. Iero, and F. G. D. Corte, “Ranging RFID Tags With Ultrasound,” *IEEE Sensors Journal*, vol. 18, no. 7, pp. 2967–2975, Apr. 2018, doi: 10.1109/JSEN.2018.2806564.

[51] L. Márton, C. Nagy, and Z. Biró-Ambrus, “Robust trilateration based indoor localization method for omnidirectional mobile robots,” in *2016 European Control Conference (ECC)*, Jun. 2016, pp. 2547–2552. doi: 10.1109/ECC.2016.7810673.

[52] Y. S. Huang, Y. P. Huang, K. N. Huang, and M. S. Young, “An accurate air temperature measurement system based on an envelope pulsed ultrasonic time-of-flight technique,” *Review of Scientific Instruments*, vol. 78, no. 11, p. 115102, Nov. 2007, doi: 10.1063/1.2804115.

[53] E. Shi, D. de Godoy, P. R. Kinget, and K.-P. Pun, “A 9.6 nW, 8-Bit, 100 S/s Envelope-to-Digital Converter for Respiratory Monitoring,” *IEEE Transactions on Circuits and Systems II: Express Briefs*, vol. 67, no. 3, pp. 445–449, Mar. 2020, doi: 10.1109/TCSII.2019.2922661.

[54] J. Warchall, P. Theilmann, Y. Ouyang, H. Garudadri, and P. P. Mercier, “Robust Biopotential Acquisition via a Distributed Multi-Channel FM-ADC,” *IEEE Transactions on Biomedical Circuits and Systems*, vol. 13, no. 6, pp. 1229–1242, Dec. 2019, doi: 10.1109/TBCAS.2019.2941846.

[55] J. Cao and A. Sabharwal, “Portable forced oscillation device for point-of-care pulmonary function testing,” in *2016 38th Annual International Conference of the IEEE Engineering in Medicine and Biology Society (EMBC)*, Aug. 2016, pp. 2282–2286. doi: 10.1109/EMBC.2016.7591185.

[56] G. Bilen-Rosas and H. G. Rosas, “System and Method for Monitoring Airflow in a Subject’s Airway with Ultrasound,” US20190167227A1, Jun. 06, 2019 Accessed: Jun. 05, 2023. [Online]. Available: https://patents.google.com/patent/US20190167227A1/en

[57] T. H. Ruscher, A. A. Muelenaer, J. R. Tamez, and A. L. Wicks, “An Acoustic Sensor For Airflow In Pediatric Artificial Airways,” in *A56. PEDIATRIC AND NEONATAL CRITICAL CARE*, in American Thoracic Society International Conference Abstracts. American Thoracic Society, 2012, pp. A1850–A1850. doi: 10.1164/ajrccm-conference.2012.185.1_MeetingAbstracts.A1850.

[58] A. Shahshahani, Z. Zilic, and S. Bhadra, “An Ultrasound-Based Biomedical System for Continuous Cardiopulmonary Monitoring: A Single Sensor for Multiple Information,” *IEEE Transactions on Biomedical Engineering*, vol. 67, no. 1, pp. 268–276, Jan. 2020, doi: 10.1109/TBME.2019.2912407.

[59] A. Sabharwal, “Forced oscillation technique based lung function testing,” US11357421B2, Jun. 14, 2022 Accessed: Jun. 05, 2023. [Online]. Available: https://patents.google.com/patent/US11357421B2/en

[60] W. Karlen, S. Raman, J. M. Ansermino, and G. A. Dumont, “Multiparameter Respiratory Rate Estimation From the Photoplethysmogram,” *IEEE Transactions on Biomedical Engineering*, vol. 60, no. 7, pp. 1946–1953, Jul. 2013, doi: 10.1109/TBME.2013.2246160.

[61] A. B. Raine, N. Aslam, C. P. Underwood, and S. Danaher, “Development of an Ultrasonic Airflow Measurement Device for Ducted Air,” *Sensors*, vol. 15, no. 5, Art. no. 5, May 2015, doi: 10.3390/s150510705.

[62] H. Gupta, V. Arumuru, and R. Jha, “Industrial Fluid Flow Measurement Using Optical Fiber Sensors: A Review,” *IEEE Sensors Journal*, vol. 21, no. 6, pp. 7130–7144, Mar. 2021, doi: 10.1109/JSEN.2020.3045506.

[63] © [2022] IEEE. Reprinted, with permission, from G. Begin, K. M. AL-Tamimi, H. H. Alamdari, T. Witter, and K. El-Sankary, “Lung Mechanics Tracking with Forced Oscillation Technique (FOT) Based on CMOS Synchronous Demodulation Principle,” *IEEE Transactions on Biomedical Circuits and Systems*, pp. 1–13, 2022, doi: 10.1109/TBCAS.2022.3186161.

[64] A. Erden *et al.*, “Evaluation of 17 patients with COVID-19 pneumonia treated with anakinra according to HScore, SOFA, MuLBSTA, and Brescia-COVID respiratory severity scale (BCRSS) scoring systems,” *J Med Virol*, vol. 93, no. 3, pp. 1532–1537, Mar. 2021, doi: 10.1002/jmv.26473.

[65] B. Xie and H. Minn, “Real-Time Sleep Apnea Detection by Classifier Combination,” *IEEE Transactions on Information Technology in Biomedicine*, vol. 16, no. 3, pp. 469–477, May 2012, doi: 10.1109/TITB.2012.2188299.

[66] F.-C. Yen, K. Behbehani, E. A. Lucas, J. R. Burk, and J. R. Axe, “A noninvasive technique for detecting obstructive and central sleep apnea,” *IEEE Transactions on Biomedical Engineering*, vol. 44, no. 12, pp. 1262–1268, Dec. 1997, doi: 10.1109/10.649998.

[67] M. Baboli, A. Singh, B. Soll, O. Boric-Lubecke, and V. M. Lubecke, “Wireless Sleep Apnea Detection Using Continuous Wave Quadrature Doppler Radar,” *IEEE Sensors Journal*, vol. 20, no. 1, pp. 538–545, Jan. 2020, doi: 10.1109/JSEN.2019.2941198.

[68] G. Avanzolini and P. Barbini, “A Versatile Identification Method Applied to Analysis of Respiratory Mechanics,” *IEEE Transactions on Biomedical Engineering*, vol. BME-31, no. 7, pp. 520–526, Jul. 1984, doi: 10.1109/TBME.1984.325293.

[69] A. M. Lauzon and J. H. Bates, “Estimation of time-varying respiratory mechanical parameters by recursive least squares,” *Journal of Applied Physiology*, vol. 71, no. 3, pp. 1159–1165, Sep. 1991, doi: 10.1152/jappl.1991.71.3.1159.

[70] D. W. Kaczka, G. M. Barnas, B. Suki, and K. R. Lutchen, “Assessment of time-domain analyses for estimation of low-frequency respiratory mechanical properties and impedance spectra,” *Ann Biomed Eng*, vol. 23, no. 2, pp. 135–151, Mar. 1995, doi: 10.1007/BF02368321.

[71] N. McARDLE, G. Devereux, H. Heidarnejad, H. M. Engleman, T. W. Mackay, and N. J. Douglas, “Long-term Use of CPAP Therapy for Sleep Apnea/Hypopnea Syndrome,” *Am J Respir Crit Care Med*, vol. 159, no. 4, pp. 1108–1114, Apr. 1999, doi: 10.1164/ajrccm.159.4.9807111.

[72] M. Takhti and K. Odame, “Structured Design Methodology to Achieve a High SNR Electrical Impedance Tomography,” *IEEE Transactions on Biomedical Circuits and Systems*, vol. 13, no. 2, pp. 364–375, Apr. 2019, doi: 10.1109/TBCAS.2019.2894157.

[73] P. Kassanos, I. F. Triantis, and A. Demosthenous, “A CMOS Magnitude/Phase Measurement Chip for Impedance Spectroscopy,” *IEEE Sensors Journal*, vol. 13, no. 6, pp. 2229–2236, Jun. 2013, doi: 10.1109/JSEN.2013.2251628.

[74] D. Allegri, A. Donida, P. Malcovati, and D. Barrettino, “CMOS-Based Multifrequency Impedance Analyzer for Biomedical Applications,” *IEEE Transactions on Biomedical Circuits and Systems*, vol. 12, no. 6, pp. 1301–1312, Dec. 2018, doi: 10.1109/TBCAS.2018.2867172.

[75] J. Xu, G. Meynants, and P. Merken, “Low-power lock-in amplifier for complex impedance measurement,” in *2009 3rd International Workshop on Advances in sensors and Interfaces*, Jun. 2009, pp. 110–114. doi: 10.1109/IWASI.2009.5184779.

[76] G. Sciortino *et al.*, “Four-Channel Differential Lock-in Amplifiers With Autobalancing Network for Stimulated Raman Spectroscopy,” *IEEE Journal of Solid-State Circuits*, vol. 56, no. 6, pp. 1859–1870, Jun. 2021, doi: 10.1109/JSSC.2020.3046484.

[77] P. M. Maya-Hernández, B. Calvo-López, and M. T. Sanz-Pascual, “Ultralow-Power Synchronous Demodulation for Low-Level Sensor Signal Detection,” *IEEE Transactions on Instrumentation and Measurement*, vol. 68, no. 10, pp. 3514–3523, Oct. 2019, doi: 10.1109/TIM.2018.2881821.

[78] C. Andrews and A. C. Molnar, “A Passive Mixer-First Receiver With Digitally Controlled and Widely Tunable RF Interface,” *IEEE Journal of Solid-State Circuits*, vol. 45, no. 12, pp. 2696–2708, Dec. 2010, doi: 10.1109/JSSC.2010.2077151.

[79] I. Padilla-Cantoya and P. M. Furth, “Enhanced Grounded Capacitor Multiplier and Its Floating Implementation for Analog Filters,” *IEEE Transactions on Circuits and Systems II: Express Briefs*, vol. 62, no. 10, pp. 962–966, Oct. 2015, doi: 10.1109/TCSII.2015.2435751.

APPENDIX

Thesis / Dissertation Reuse

The IEEE does not require individuals working on a thesis to obtain a formal reuse license, however, you may print out this statement to be used as a permission grant:

Requirements to be followed when using any portion (e.g., figure, graph, table, or textual material) of an IEEE copyrighted paper in a thesis:

1) In the case of textual material (e.g., using short quotes or referring to the work within these papers) users must give full credit to the original source (author, paper, publication) followed by the IEEE copyright line © 2011 IEEE.
2) In the case of illustrations or tabular material, we require that the copyright line © [Year of original publication] IEEE appear prominently with each reprinted figure and/or table.
3) If a substantial portion of the original paper is to be used, and if you are not the senior author, also obtain the senior author's approval.

Requirements to be followed when using an entire IEEE copyrighted paper in a thesis:

1) The following IEEE copyright/ credit notice should be placed prominently in the references: © [year of original publication] IEEE. Reprinted, with permission, from [author names, paper title, IEEE publication title, and month/year of publication]
2) Only the accepted version of an IEEE copyrighted paper can be used when posting the paper or your thesis on-line.
3) In placing the thesis on the author's university website, please display the following message in a prominent place on the website: In reference to IEEE copyrighted material which is used with permission in this thesis, the IEEE does not endorse any of [university/educational entity's name goes here]'s products or services. Internal or personal use of this material is permitted. If interested in reprinting/republishing IEEE copyrighted material for advertising or promotional purposes or for creating new collective works for resale or redistribution, please go to http://www.ieee.org/publications_standards/publications/rights/rights_link.html to learn how to obtain a License from RightsLink.

If applicable, University Microfilms and/or ProQuest Library, or the Archives of Canada may supply single copies of the dissertation.

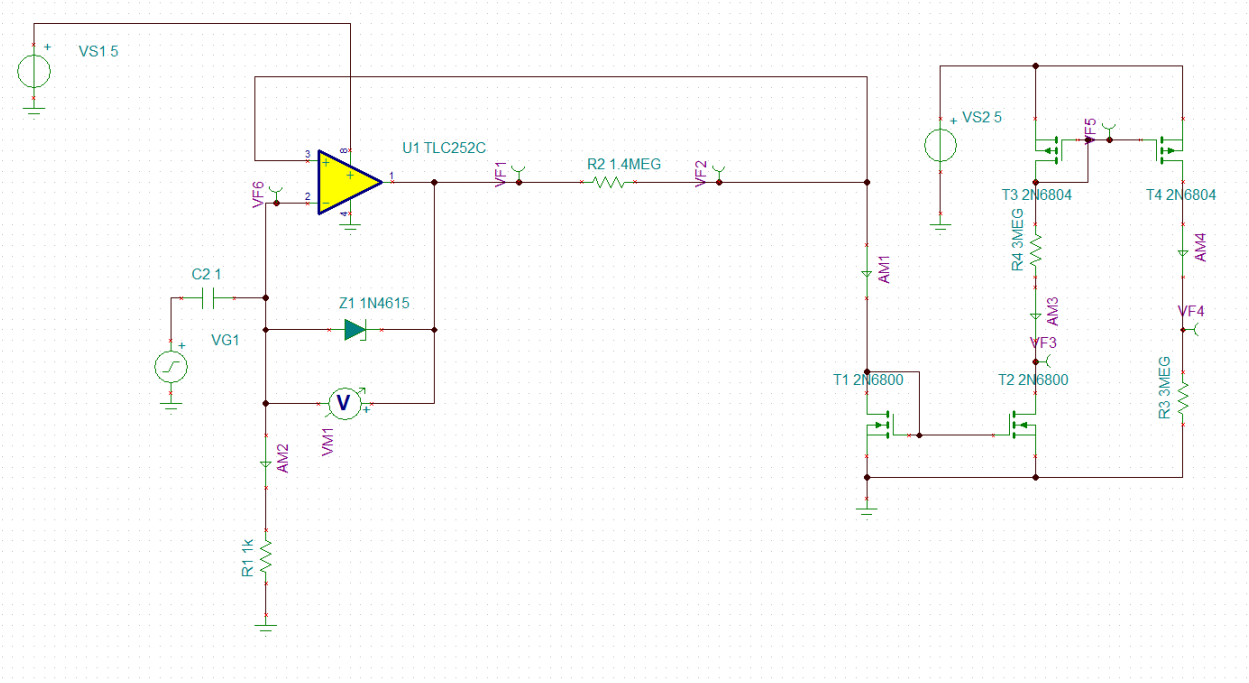

***Figure 71**: 250nA current source generation on PCB to bias on chip components.*

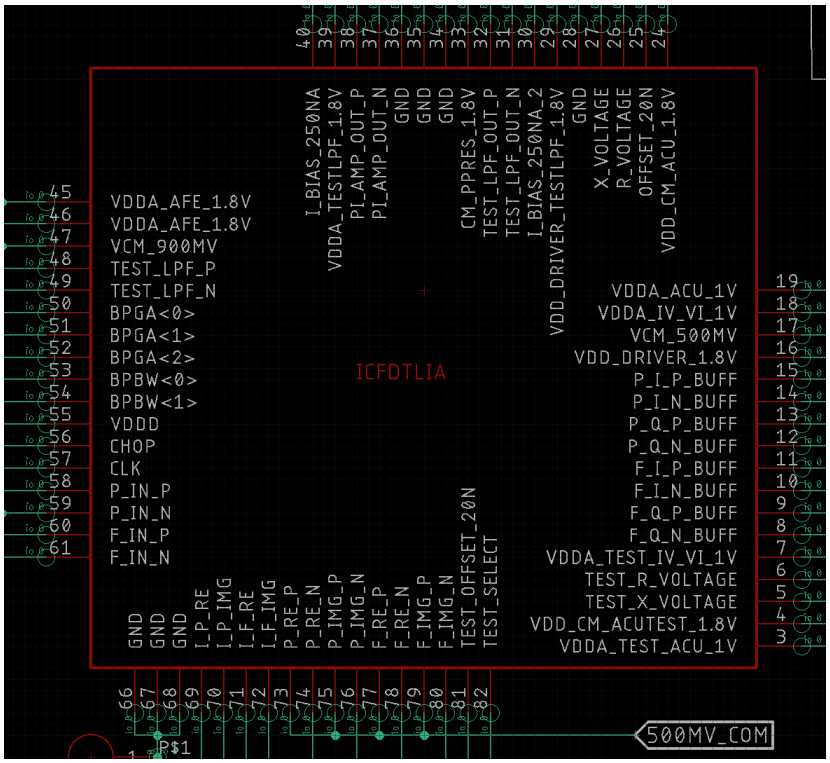

***Figure 72**: Pinout symbol of the ICFDTLIA chip on PCB.*

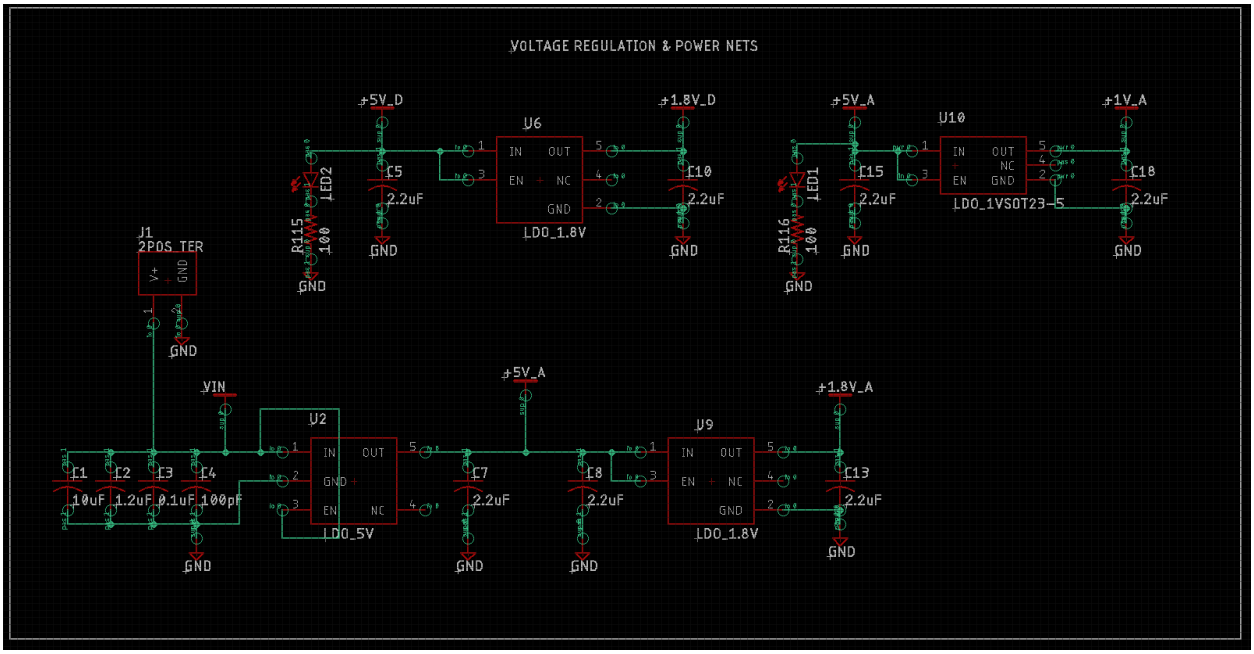

***Figure 73**: Voltage regulation and power distribution nets on PCB.*

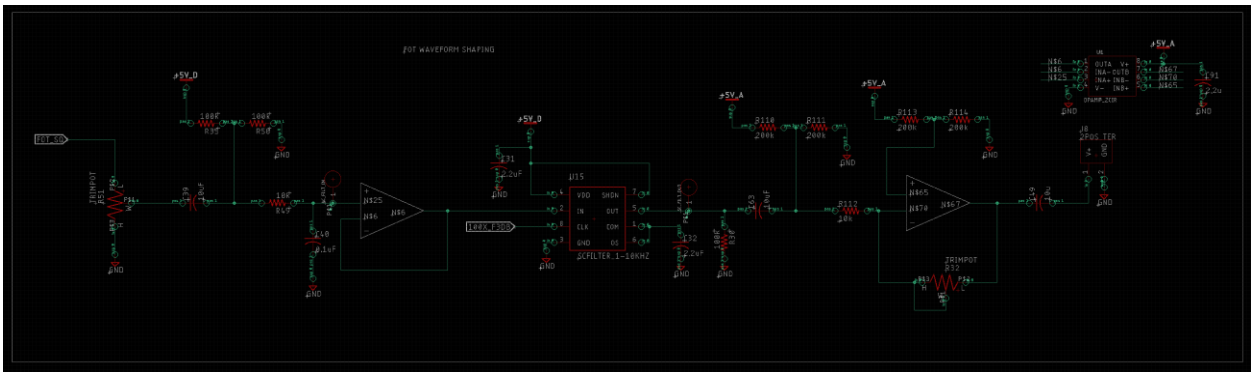

***Figure 74**: FOT analog waveform shaping circuit on PCB.*

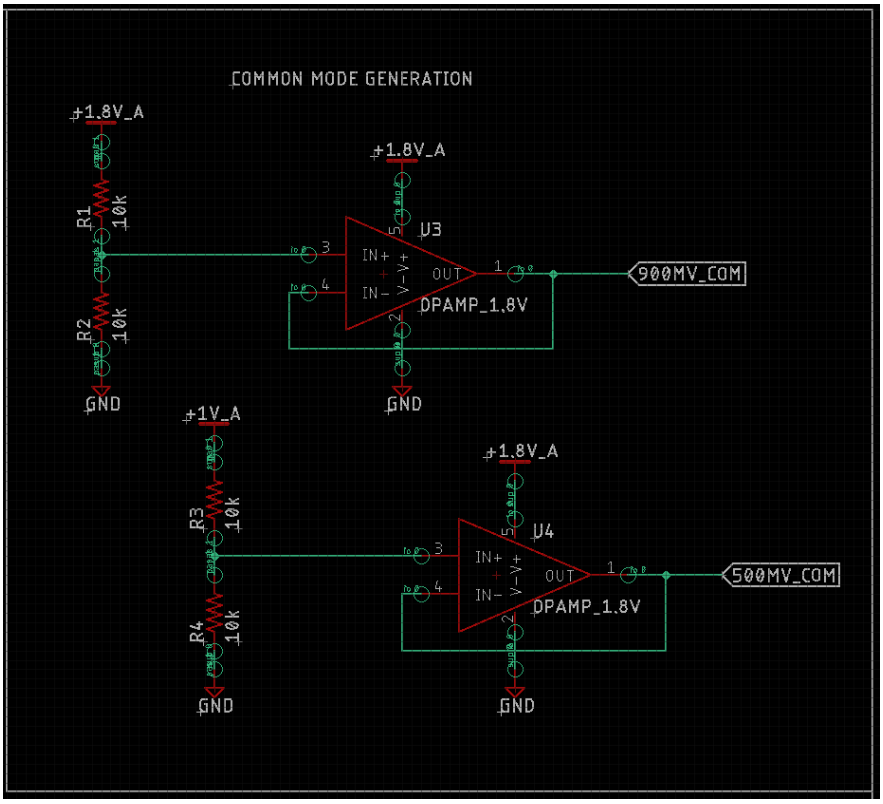

***Figure 75**: Common mode signal generation circuits on PCB.*

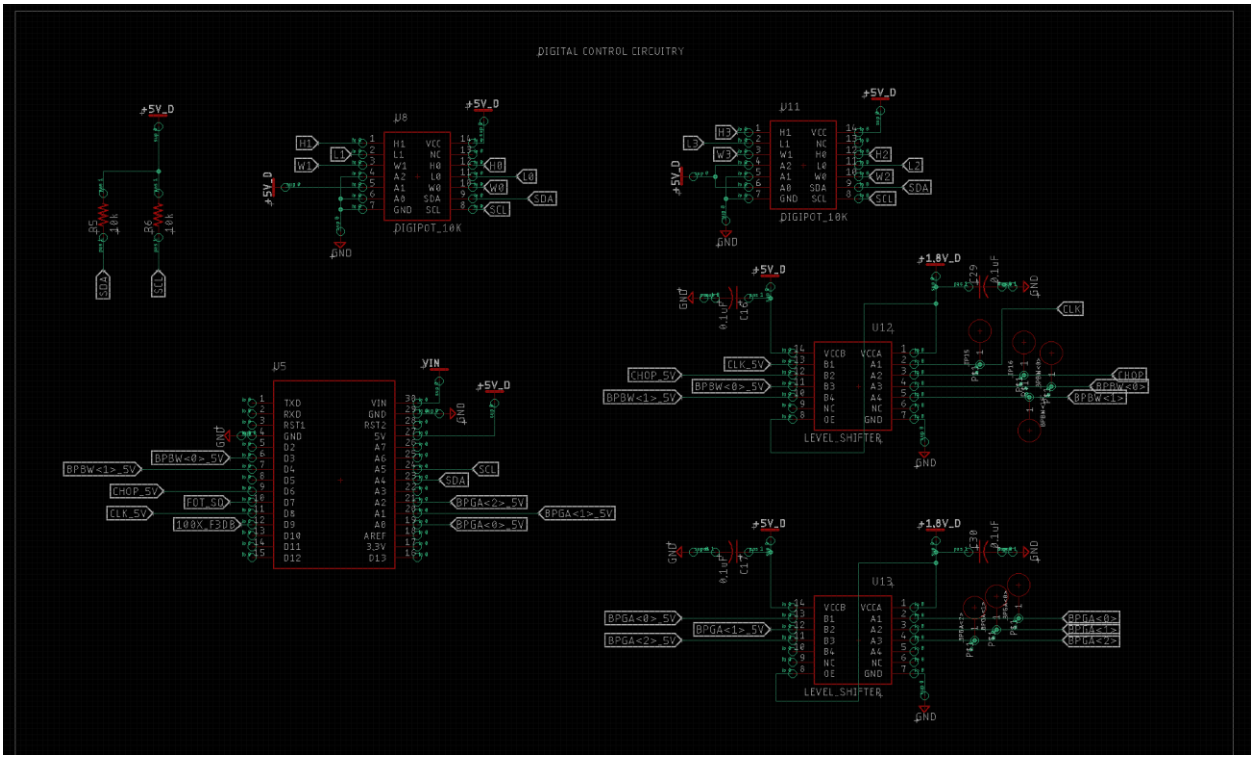

***Figure 76**: Digital control circuitry on PCB.*

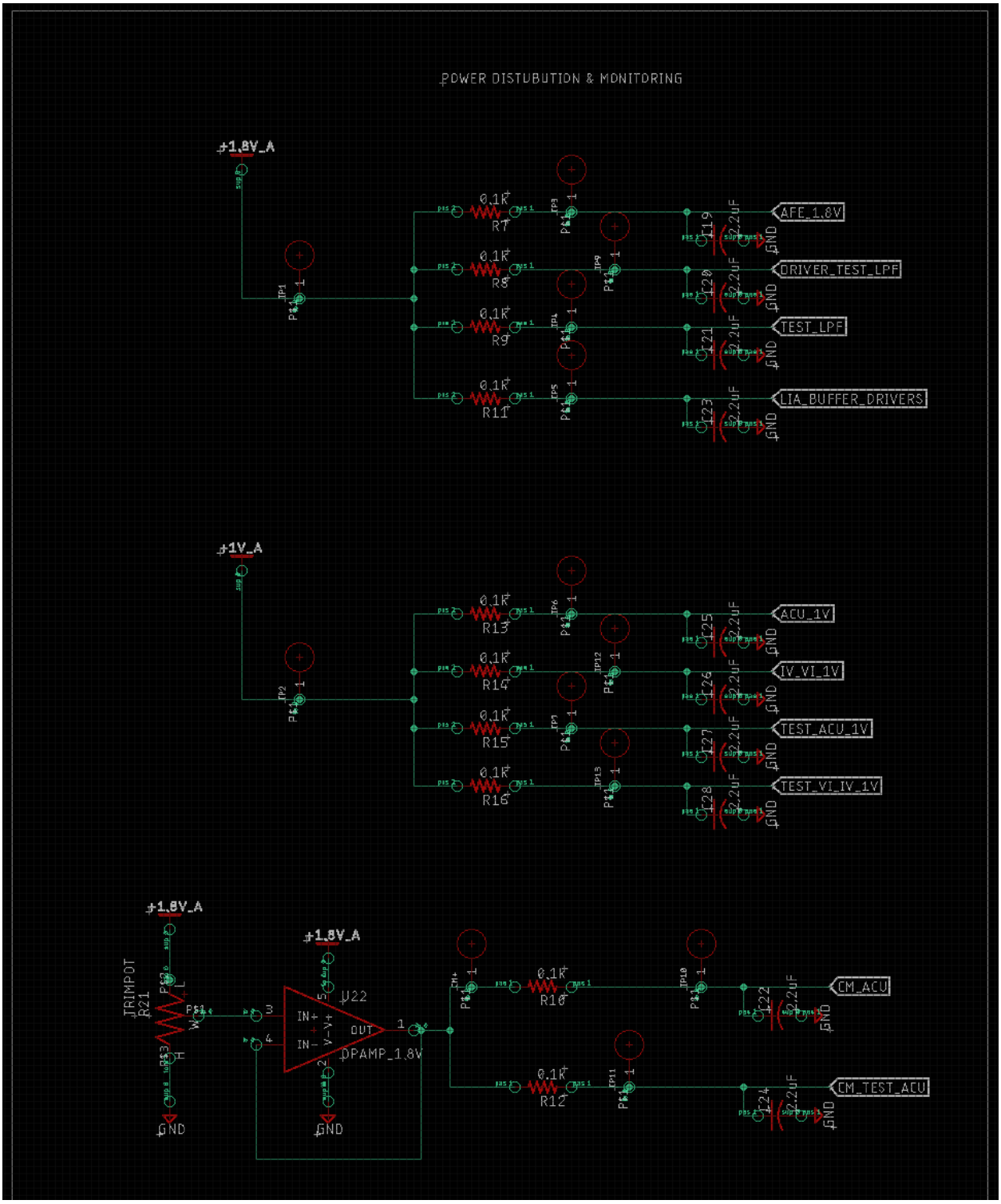

***Figure 77**: Power monitoring circuitry for analyzing power consumption of ICFDTLIA from PCB.*

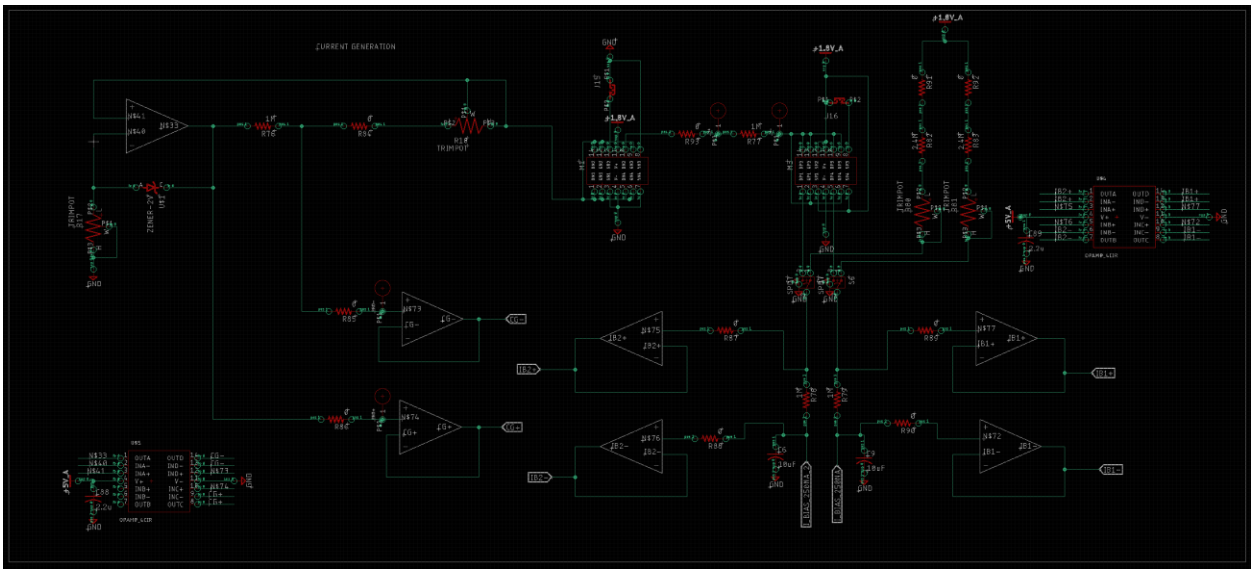

***Figure 78**: 250nA current generation circuitry schematic on PCB, including buffering/isolation of scope probes.*

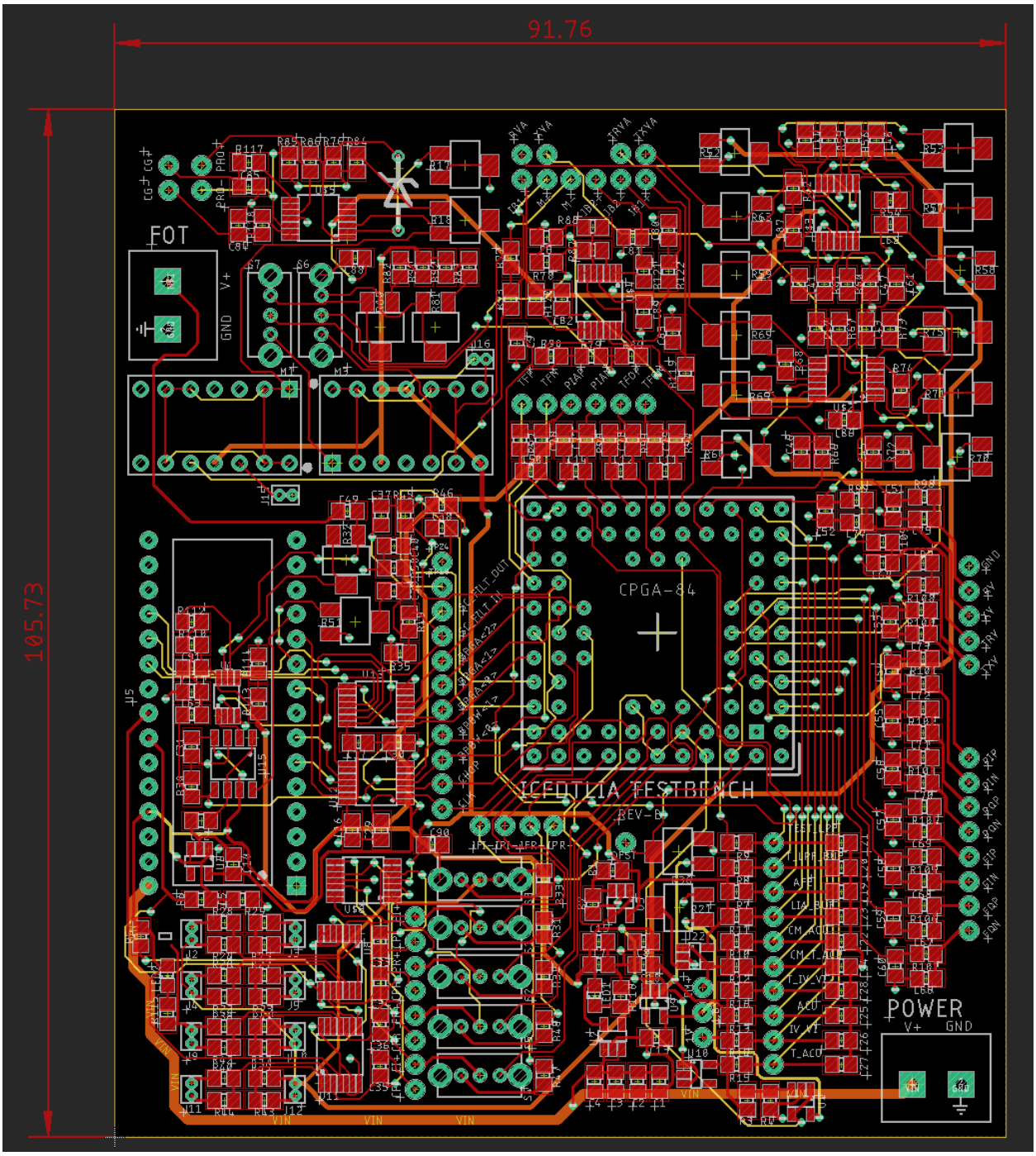

***Figure 79**: Printed circuit board layout CAD files.*

Package Pin	Coord.	Name	Domain	Value	Description	Package Pin	Coord.	Name	Domain	Value	Description
1	B2	NC	N/A	N/A	N/A	43	K10	NC	N/A	N/A	N/A
2	C2	NC	N/A	N/A	N/A	44	J10	NC	N/A	N/A	N/A
3	B1	VDDA_TEST_ACU_1V	Supply	1V		45	K11	VDDA_AFE_1.8V	Supply	1.8V	
4	C1	VDD_CM_ACUTEST_1.8V	Supply	1.8V		46	J11	VDDA_AFE_1.8V	Supply	1.8V	
5	D2	TEST_R_VOLTAGE	Analog			47	H10	VCM_900mV	Supply	900mV	
6	D1	TEST_X_VOLTAGE	Analog			48	H11	TEST_LPF_P	Analog		
7	E3	VDDA_TEST_IV_VI_1V	Supply	1V		49	F10	TEST_LPF_N	Analog		
8	E2	F_Q_N_BUFF	Analog			50	G10	BPGA<0>	Digital		
9	E1	F_Q_P_BUFF	Analog			51	G11	BPGA<1>	Digital		
10	F2	F_I_N_BUFF	Analog			52	G9	BPGA<2>	Digital		
11	F3	F_I_P_BUFF	Analog			53	F9	BPBW<0>	Digital		
12	G3	P_Q_N_BUFF	Analog			54	F11	BPBW<1>	Digital		
13	G1	P_Q_P_BUFF	Analog			55	E11	VDDD	Supply	1.8V	
14	G2	P_I_N_BUFF	Analog			56	E10	CHOP	Digital		
15	F1	P_I_P_BUFF	Analog			57	E9	CLK	Digital		
16	H1	VDDD_DRIVER_1.8V	Supply	1.8V		58	D11	P_IN_P	Analog		
17	H2	VCM_500mV	Supply	500mV		59	D10	P_IN_N	Analog		
18	J1	VDDA_IV_VI_1V	Supply	1V		60	C11	F_IN_P	Analog		
19	K1	VDDA_ACU_1V	Supply	1V		61	B11	F_IN_N	Analog		
20	J2	NC	N/A	N/A	N/A	62	C10	NC	N/A	N/A	N/A
21	L1	NC	N/A	N/A	N/A	63	A11	NC	N/A	N/A	N/A
22	K2	NC	N/A	N/A	N/A	64	B10	NC	N/A	N/A	N/A
23	K3	NC	N/A	N/A	N/A	65	B9	NC	N/A	N/A	N/A
24	L2	VDD_CM_ACU_1.8V	Supply	1.8V		66	A10	GND	GND	GND	GND
25	L3	OFFSET_20n	Analog			67	A9	GND	GND	GND	GND
26	K4	R_VOLTAGE	Analog			68	B8	GND	GND	GND	GND
27	L4	X_VOLTAGE	Analog			69	A8	I_P_IMG	Analog		
28	J5	CM_PPRES_1.8V	GND	GND	GND	70	B6	I_P_RE	Analog		
29	K5	VDD_DRIVER_TESTLPF_1.8V	Supply	1.8V		71	B7	I_F_IMG	Analog		
30	L5	I_BIAS_250nA_2	Supply	250nA		72	A7	I_F_RE	Analog		
31	K6	TEST_LPF_OUT_N	Analog			73	C7	P_RE_N	Analog		
32	J6	TEST_LPF_OUT_P	Analog			74	C6	P_RE_P	Analog		
33	J7	GND	Supply	1.8V		75	A6	P_IMG_N	Analog		
34	L7	GND	GND	GND	GND	76	A5	P_IMG_P	Analog		
35	K7	GND	GND	GND	GND	77	B5	F_RE_N	Analog		
36	L6	GND	GND	GND	GND	78	C5	F_RE_P	Analog		
37	L8	PI_AMP_OUT_N	Analog			79	A4	F_IMG_N	Analog		
38	K8	PI_AMP_OUT_P	Analog			80	B4	F_IMG_P	Analog		
39	L9	VDDA_TESTLPF_1.8V	Supply	1.8V		81	A3	TEST_OFFSET_20n	Analog		
40	L10	I_BIAS_250nA	Supply	250nA		82	A2	TEST_SELECT	Digital		
41	K9	NC	N/A	N/A	N/A	83	B3	NC	N/A	N/A	N/A
42	L11	NC	N/A	N/A	N/A	84	A1	NC	N/A	N/A	N/A

***Figure 80**: ICFDTLIA pinout description chart.*

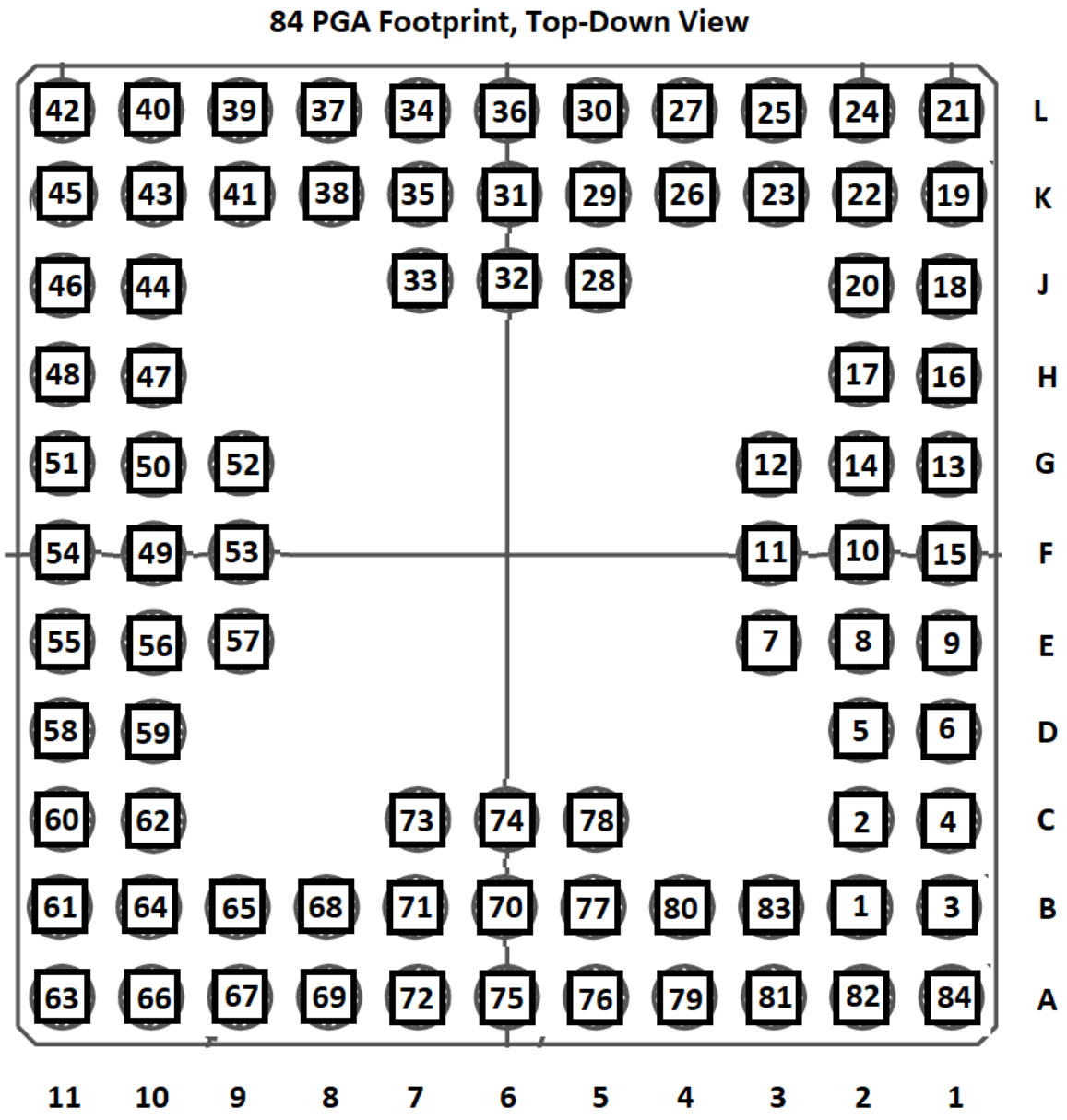

***Figure 81**: ICFDTLIA Pinout map for PCB*

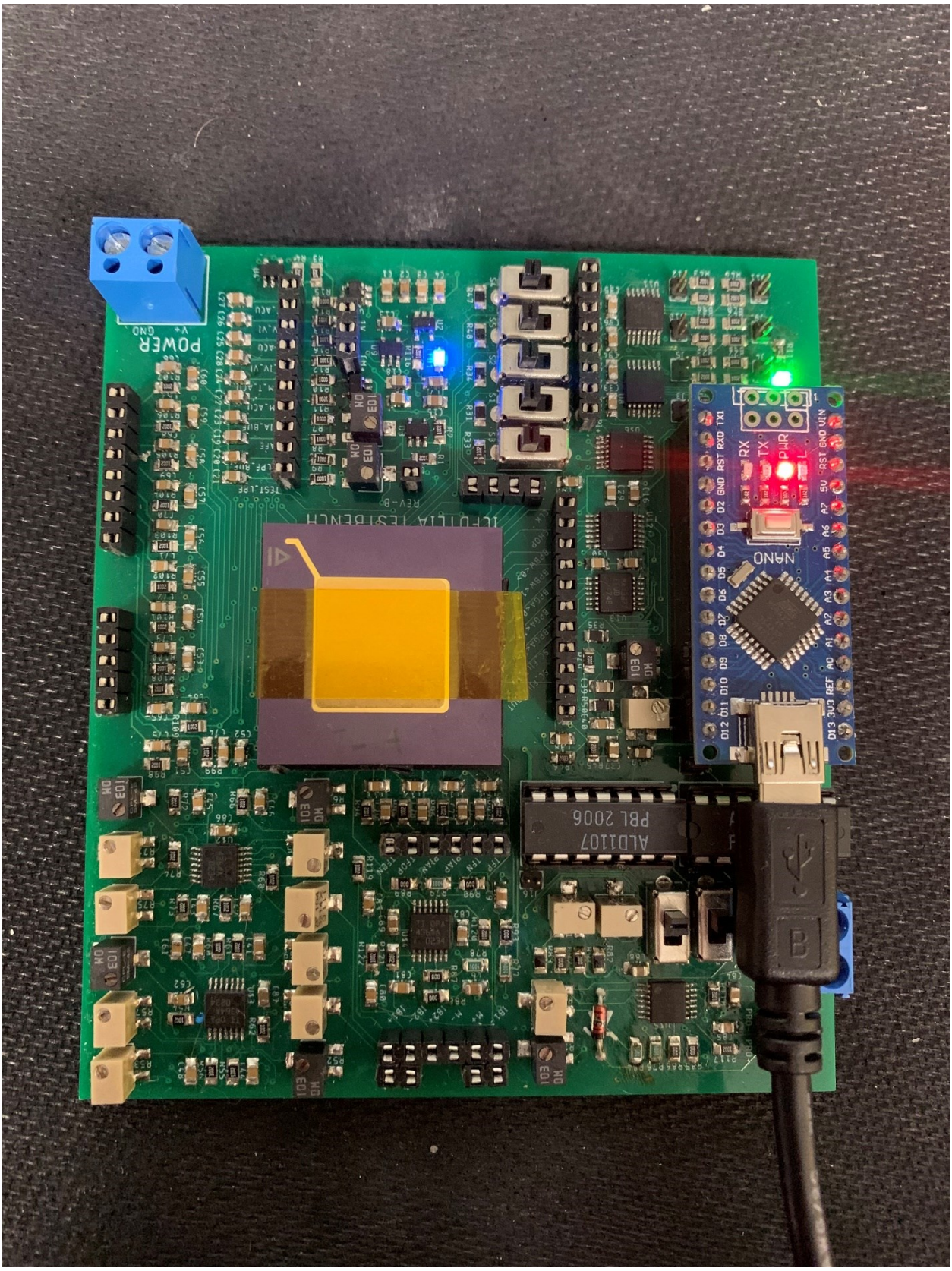

***Figure 82**: Final PCB with soldered components*

Firmware for ICFDTLIA PCB:

```
// ICFDTLIA Firmware
// Author: Gregory Begin

#include "Wire.h"

// Programmable Gain/Bandwidth controls
void Bandwidth(bool BW_0, bool BW_1);
void Gain(bool PG_0, bool PG_1, bool PG_2);

// initialize 8-bit scaling register for FOT generation and CLK, driven by Timer1 OC1A
volatile byte clk_scale_reg = 0;
// toggle Booleans for generating the digital outputs
volatile bool tog_clk = 0, tog_fot = 0 ;

//------------------------------ Start Setup -----------------------------

void setup() {

    ////////////// Setup timer 1 for high precision frequency (CTC)////////////

    // Enable D9 (OC1A) for digital output
    pinMode(9, OUTPUT);

    // ensure interrupts are disabled
    cli();

    // Set internal registers for Toggle on compare match, prescaler = 1, CTC.
    TCCR1A = 0;
    TCCR1B = 0;
    TCCR1A |= (1<<COM1A0);
    TCCR1B |= (1<<WGM12) | (1<<CS10);

    // Set interrupt mask register to allow for OCR1A internal interrupt
    TIMSK1 = 0;
    TIMSK1 = (1<<OCIE1A);

    // Set FOT generation frequency
    // 4Hz FOT = 8MHz/(4*128)Hz = 15625
    // 17Hz FOT = 8MHz/(17*128)Hz = 3676
    // 43Hz FOT = 8MHz/(43*128)Hz = 1453
    // 79Hz FOT = 8MHz/(79*128)Hz = 791

    OCR1A = 3676;

    ////////////////////// Setup 10Khz Chopper Signal ////////////////////////

    // 10kHz chopper pin (PIN D6) Timer_0, OC0A
    pinMode(6, OUTPUT); // CHOP

    // Setup internal registers
    // Toggle on compare match, CTC, prescaler = 8
    TCCR0A = 0;
    TCCR0B = 0;
    TCCR0A |= (1<<COM0A0) | (1<<WGM01);
    TCCR0B |= (0<<CS02) | (1<<CS01);

    // 8MHz/10kHz = 800 / clk8 = 100
    OCR0A = 100;

    // Re-enable interrupts
    sei();

    ////////////////// CONFIGURE DIGITAL OUTPUTS ///////////////////////
```

```
    // Enable the level shifter (PIN D12 / PB4)
    // Set D12 as an output
    pinMode(12, OUTPUT);
    // Set D12 HIGH
    digitalWrite(12, HIGH);

    // Setup Bandwidth and Gain control pins
    // BW
    pinMode(3, OUTPUT); //BW_0
    pinMode(4, OUTPUT); //BW_1
    // GAIN
    pinMode(A0, OUTPUT); //PG_0
    pinMode(A1, OUTPUT); //PG_1
    pinMode(A2, OUTPUT); //PG_2
    // WAVEFORM
    pinMode(7, OUTPUT); // FOT
    pinMode(8, OUTPUT); // CLK



    Bandwidth(0, 0);
    Gain(0, 0, 0);
}

//---------------------------- MAIN INTERRUPT ROUTINE -----------------------------

ISR(TIMER1_COMPA_vect){

  // increment frequency scaling register
  clk_scale_reg++;

  // if scaling register is factor of 32, toggle CLK output
  if(!(clk_scale_reg % 32)){
    digitalWrite(8, tog_clk);
    tog_clk = !tog_clk;
  }


  // if scaling register is factor of 128, toggle FOT output
  if(!(clk_scale_reg % 128)){
    digitalWrite(7, tog_fot);
    tog_fot = !tog_fot;
  }
}

//---------------------------------- MAIN LOOP ----------------------------------

void main(){}

//---------------------------- FUNCTION DEFINITIONS -----------------------------


// Set digital pins according to bandwidth settings
void Bandwidth(bool BW_0, bool BW_1){

digitalWrite(3, BW_0);
digitalWrite(4, BW_1);

}

// Set digital pins according to gain settings
void Gain(bool PG_0, bool PG_1, bool PG_2){

digitalWrite(A0, PG_0);
digitalWrite(A1, PG_1);
digitalWrite(A2, PG_2);

}
```

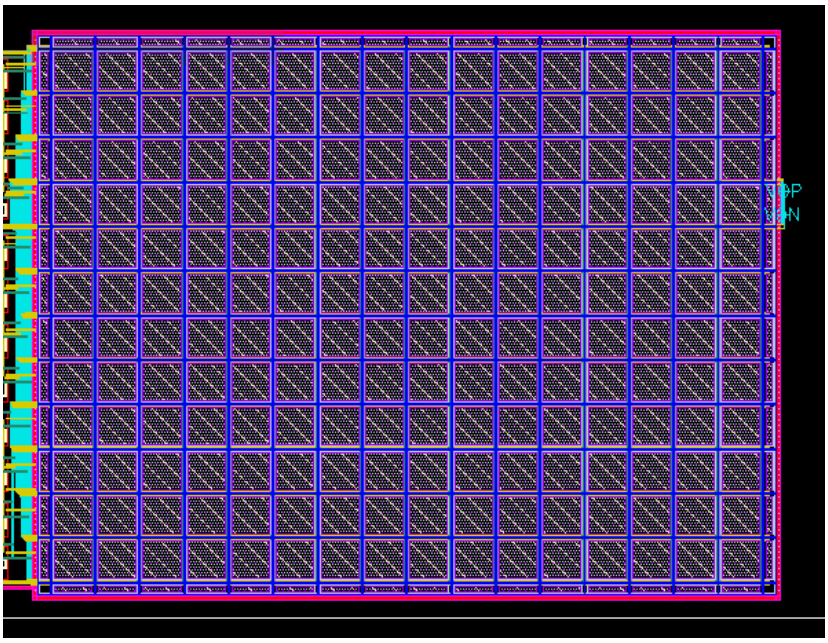

***Figure 83**: Cadence Layout of 4 stages of low pass filter.*

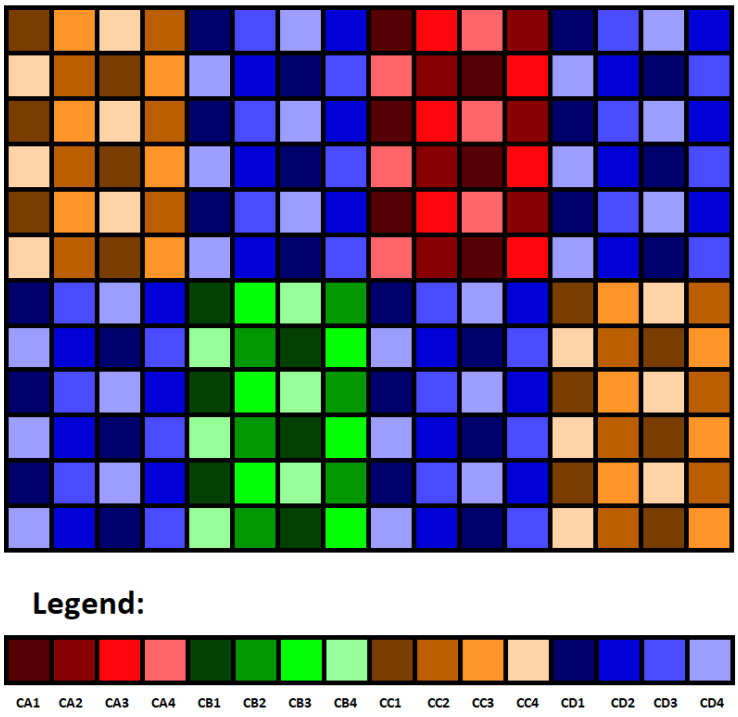

***Figure 84**: Capacitor bank layout with legend.*

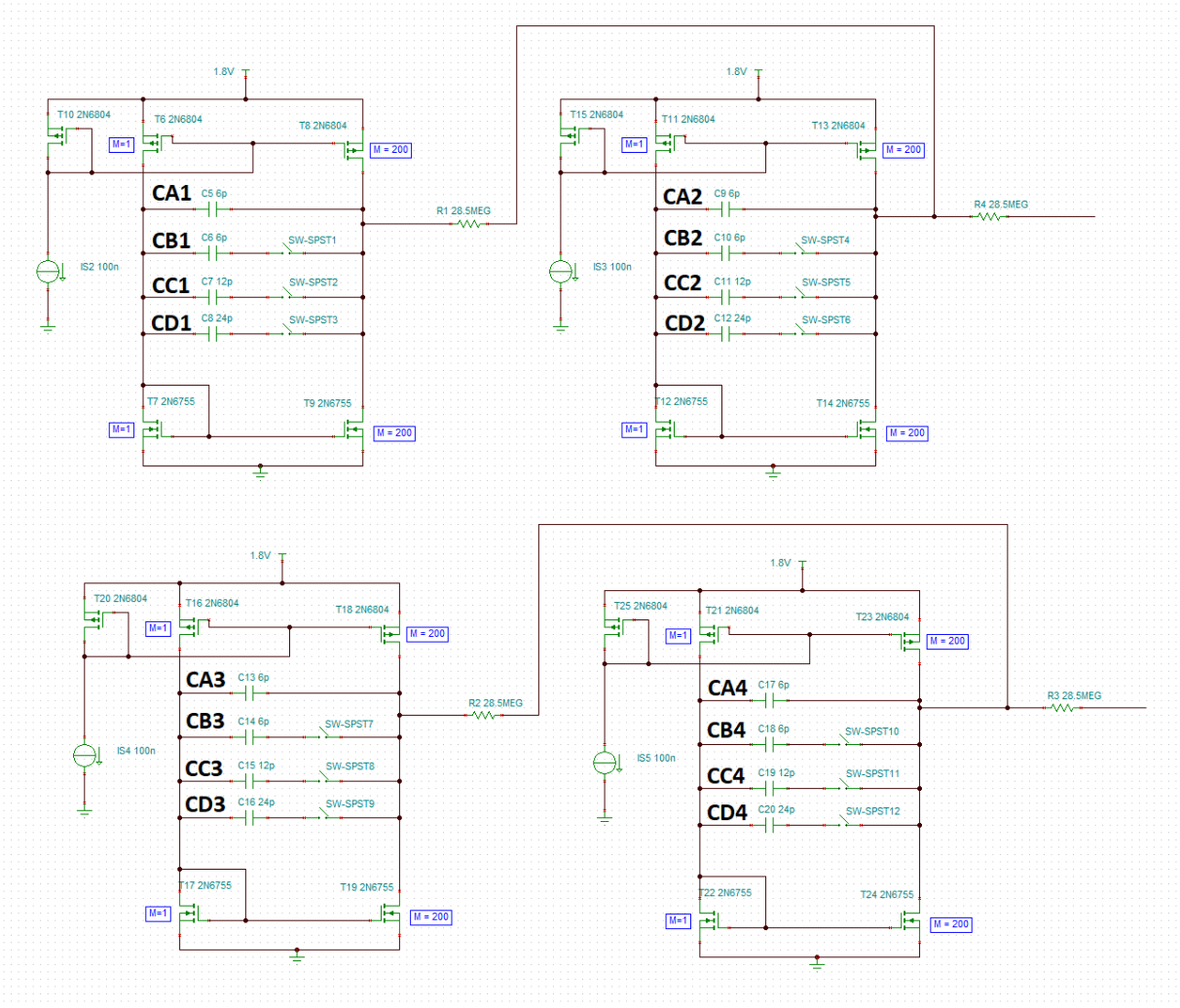

***Figure 85**: Fully differential sub-Hz 2nd order low pass filter circuit schematic with capacitors labelled.*